Title

A Census of Sub-kiloparsec Resolution Metallicity Gradients in Star-forming Galaxies at Cosmic Noon from HST Slitless Spectroscopy

Permalink
https://escholarship.org/uc/item/4qm7c9nc

Journal
The Astrophysical Journal, 900(2)

ISSN
0004-637X

Authors
Wang, Xin
Jones, Tucker A
Treu, Tommaso
et al.

Publication Date
2020-09-01

DOI
10.3847/1538-4357/abacce

Draft version July 24, 2020
Typeset using LaTeX **twocolumn** style in AASTeX63

A Census of Sub-kiloparsec Resolution Metallicity Gradients in Star-forming Galaxies at Cosmic Noon from *HST* Slitless Spectroscopy

Xin Wang,[1, 2] Tucker A. Jones,[3] Tommaso Treu,[2] Emanuele Daddi,[4] Gabriel B. Brammer,[5] Keren Sharon,[6] Takahiro Morishita,[7]
Louis E. Abramson,[8] James W. Colbert,[1] Alaina L. Henry,[7] Philip F. Hopkins,[9] Matthew A. Malkan,[2] Kasper B. Schmidt,[10]
Harry I. Teplitz,[1] and Benedetta Vulcani[11]

[1]*Infrared Processing and Analysis Center, Caltech, 1200 E. California Blvd., Pasadena, CA 91125, USA*
[2]*Department of Physics and Astronomy, University of California, Los Angeles, CA 90095-1547, USA*
[3]*University of California Davis, 1 Shields Avenue, Davis, CA 95616, USA*
[4]*Laboratoire AIM, CEA/DSM-CNRS-Université Paris Diderot, IRFU/Service d'Astrophysique, Bât. 709, CEA Saclay, F-91191 Gif-sur-Yvette Cedex, France*
[5]*Cosmic Dawn Centre, University of Copenhagen, Blegdamsvej 17, 2100 Copenhagen, Denmark*
[6]*Department of Astronomy, University of Michigan, 1085 S. University Avenue, Ann Arbor, MI 48109, USA*
[7]*Space Telescope Science Institute, 3700 San Martin Drive, Baltimore, MD, 21218, USA*
[8]*The Observatories of the Carnegie Institution for Science, 813 Santa Barbara St., Pasadena, CA 91101, USA*
[9]*TAPIR, California Institute of Technology, Pasadena, CA 91125, USA*
[10]*Leibniz-Institut für Astrophysik Potsdam (AIP), An der Sternwarte 16, D-14482 Potsdam, Germany*
[11]*INAF- Osservatorio Astronomico di Padova, Vicolo Osservatorio 5, I-35122 Padova, Italy 0000-0003-0980-1499*

Abstract

We present hitherto the largest sample of gas-phase metallicity radial gradients measured at sub-kiloparsec resolution in star-forming galaxies in the redshift range of $z \in [1.2, 2.3]$. These measurements are enabled by the synergy of slitless spectroscopy from the Hubble Space Telescope near-infrared channels and the lensing magnification from foreground galaxy clusters. Our sample consists of 76 galaxies with stellar mass ranging from 10^7 to 10^{10} $M_\odot$, instantaneous star-formation rate in the range of [1, 100] $M_\odot$/yr, and global metallicity $[\frac{1}{12}, 2]$ solar. At 2-σ confidence level, 15/76 galaxies in our sample show negative radial gradients, whereas 7/76 show inverted gradients. Combining ours and all other metallicity gradients obtained at similar resolution currently available in the literature, we measure a negative mass dependence of $\Delta\log(\mathrm{O/H})/\Delta r$ [dex kpc^{-1}] = $(-0.020 \pm 0.007) + (-0.016 \pm 0.008)\log(M_*/10^{9.4} M_\odot)$ with the intrinsic scatter being $\sigma = 0.060 \pm 0.006$ over four orders of magnitude in stellar mass. Our result is consistent with strong feedback, not secular processes, being the primary governor of the chemo-structural evolution of star-forming galaxies during the disk mass assembly at cosmic noon. We also find that the intrinsic scatter of metallicity gradients increases with decreasing stellar mass and increasing specific star-formation rate. This increase in the intrinsic scatter is likely caused by the combined effect of cold-mode gas accretion and merger-induced starbursts, with the latter more predominant in the dwarf mass regime of $M_* \lesssim 10^9 M_\odot$.

Keywords: galaxies: abundances — galaxies: evolution — galaxies: formation — galaxies: high-redshift — gravitational lensing: strong

1. INTRODUCTION

Metallicity is one of the most fundamental proxies of galaxy evolution at the peak of cosmic star formation and metal enrichment ($1 \lesssim z \lesssim 3$), i.e., the cosmic noon epoch (Madau & Dickinson 2014). The interstellar medium oxygen abundance relative to hydrogen — metallicity[1] — has been shown to correlate strongly with stellar mass (M_*), star-formation rate (SFR) and gas fraction (see the recent review by Maiolino & Mannucci 2018, and references therein). The cumulative history of the baryonic mass assembly, e.g., star formation, gas accretion, mergers, feedback and galactic winds, altogether governs the total amount of metals remain-

Corresponding author: Xin Wang
wangxin@ipac.caltech.edu

---

[1] Throughout this paper, we use metallicity to stand for gas-phase oxygen abundance unless otherwise specified.

ing in gas (Finlator & Davé 2008; Davé et al. 2012; Lilly et al. 2013; Dekel & Mandelker 2014; Peng & Maiolino 2014). Moreover, these baryon cycling processes also tightly regulate the spatial distribution of metals in galaxies (Ho et al. 2015; Sanchez-Menguiano et al. 2016; Belfiore et al. 2019). Thus, a powerful way to learn about the baryon cycle is to use spatially resolved information.

The conventional way to obtain spatially resolved information is through integral field spectroscopy (IFS). IFS has dramatically expanded our vision of galaxies from spectroscopic measurements integrated through single slits/fibres to panoramic 2-dimensional (2D) views across their full surfaces, allowing for spatial variations of physical properties (including metallicity). This facilitates several large ground-based surveys (e.g. CALIFA, MaNGA, SAMI) to constrain the radial profile of metallicity in hundreds of galaxies, successfully capturing the dynamic signatures of the baryon cycle (see e.g., Sanchez et al. 2014; Belfiore et al. 2017; Poetrodjojo et al. 2018). Meanwhile numerical simulations are now capable of making useful predictions for metallicity radial gradients and their evolution with redshift (e.g. Ma et al. 2017; Tissera et al. 2018). The main challenge for observations is that sub-kiloparsec (sub-kpc) spatial resolution is required for accurate results and meaningful comparison with theoretical predictions. While this spatial sampling is readily achieved for nearby galaxies ($z \lesssim 0.3$), seeing-limited data are insufficient for galaxies at moderate to high redshift. Therefore we need an effective approach to achieve sub-kpc resolved spectroscopy for statistically representative samples of high-z galaxies to compare meaningfully with cosmological zoom-in simulations.

The approach we take is space-based slitless spectroscopy. Building upon our previous efforts (Jones et al. 2015; Wang et al. 2017, 2019), we exploit grism spectroscopy from the Hubble Space Telescope (*HST*). *HST*'s diffraction limit in the near-infrared wavelengths is equivalent to a physical scale of $\sim$1 kpc at $z\sim2$. Additional gain in resolution can be provided by gravitational lensing by foreground galaxies and/or galaxy clusters to fully satisfy the requirement for sufficiently resolving the chemical profiles of galaxies at that epoch. Lensing is thus essential for resolving the lowest-mass galaxies at high redshifts. Recently, Curti et al. (2020) derived metallicity maps and radial gradients in a sample of 28 lensed galaxies with stellar mass as low as $10^9 M_\odot$. In this work, we measure radial gradients of metallicity in 76 star-forming galaxies at $1.2 \lesssim z \lesssim 2.3$ gravitationally lensed by foreground galaxy clusters, further extending to even lower stellar masses. Our sample enables a detailed comparison between observed and simulated chemo-structural properties of galaxies, offering valuable insights into galaxy evolution.

This paper is organized as follows. In Section 2, we describe the data and galaxy sample analyzed in this work. The measurements of various physical quantities for our sample galaxies are presented in Section 3. Then two major pieces of our analysis results, i.e., the redshift evolution and mass dependence of sub-kpc resolution metallicity gradients, are shown in Sections 4 and 5, respectively. We finally conclude in Section 6. Throughout this paper, the AB magnitude system and standard concordance cosmology (Ω_m =0.3, Ω_Λ =0.7, H_0 = 70km s^{-1} Mpc^{-1}) are used. Forbidden lines are indicated as follows: [O III]$\lambda5008$:= [O III], [O II]$\lambda\lambda3727,3730$:= [O II], [N II] $\lambda6585$:= [N II], [S II] $\lambda\lambda6718,6732$:= [S II], if presented without wavelength values.

2. DATA AND SAMPLE SELECTION

The spectroscopic data analyzed in this work are acquired by the Grism Lens-Amplified Survey from Space[2] (*GLASS*; Proposal ID 13459; P.I. Treu, Schmidt et al. 2014; Treu et al. 2015). It is a cycle-21 *HST* large program allocated 140 orbits of Wide-Field Camera 3 (WFC3) near-infrared slitless spectroscopy on the centers of 10 strong-lensing galaxy clusters. For each cluster center field, we have 10 orbits of G102 (covering 0.8-1.15μm) and 4 orbits of G141 (covering 1.1-1.7μm) exposures, amounting to $\sim$22 kilo-seconds of G102 and $\sim$9 kilo-seconds of G141 in total, together with $\sim$7 kilo-seconds of F105W+F140W direct imaging for wavelength/flux calibration and astrometric alignment. This exposure time is divided equally into two orients with almost orthogonal light dispersion directions, designed to disentangle contamination from neighbor objects. As a result, we obtain two suites of G102+G141 spectra for each object, in an uninterrupted wavelength range of 0.8-1.7 μm with nearly uniform sensitivity, reaching 1-σ surface brightness of 3×10^{-16} erg s^{-1} cm^{-2} arcsec^{-2}. The 10 cluster fields are listed in Table 1 and shown in Fig. 1. Among these clusters, 6 have ultra-deep 7-filter imaging from the Hubble Frontier Fields (*HFF*) initiative (Lotz et al. 2016). The other 4 have multi-band imaging from the Cluster Lensing And Supernova survey with Hubble (*CLASH*) (Postman et al. 2012).

We base our source selection on the redshift catalogs made public by the *GLASS* collaboration. From these catalogs, we select 327 galaxies with secure spectroscopic redshifts in the range of $z \in [1.2, 2.3]$ with the redshift quality flag $\geq$3. This redshift range is chosen to enable the grism coverage of the oxygen collisionally excited lines and the Balmer lines in rest-frame optical (i.e., [O III], Hβ, [O II]), which are the most promising and frequently used metallicity diagnostics at extragalactic distances. We also visually inspect the spatial extent and grism data quality of each source, to remove sources with compact morphology (i.e., with half-light radius R_{50} < $0\farcs25$ measured in H_{160}-band imaging) and/or

---

[2] https://archive.stsci.edu/prepds/glass/

severe grism defects, not suitable for our analysis. As a consequence, we compile a list of 93 objects with secure spectroscopic redshifts, relatively extended spatial profiles, and no severe defects nor lack of data in their grism spectra. After further removing the sources with low signal-to-noise ratio (SNR) detections of emission lines (see Sect. 3.1), and those with ionization contamination from the active galactic nucleus (AGN; see Sect. 3.4), we obtain the final sample comprising a total of 76 star-forming galaxies at $z \in [1.2, 2.3]$, on which we present the subsequent measurements.

3. METHODOLOGY AND MEASUREMENTS

3.1. *Emission line flux*

We adopt the Grism Redshift and Line Analysis software (GRIZLI[3]; G. Brammer et al. in prep) to handle wide-field slitless spectroscopy data reduction. GRIZLI is a state-of-the-art software that performs "one-stop-shopping" processing of paired direct and grism exposures acquired by space telescopes. The entire procedure consists of five steps: 1) preprocessing of raw grism exposures[4], 2) forward modeling full field-of-view (FoV) grism images, 3) redshift fitting via spectral template synthesis, 4) refining full FoV grism model, and 5) extracting 1D/2D spectra and emission line maps of individual targets.

In Step 3), we derive the best-fit redshift of our sources from spectral template fitting based on a library of spectral energy distributions (SED) of stellar populations with a range of characteristic ages (see Appendix A in Wang et al. 2019, for more details). We also fit the intrinsic nebular emission using 1D Gaussian functions centered at corresponding wavelengths and estimate the line fluxes. The morphological broadening is taken into account with respect to the dispersion direction associated with each exposure. Fig. 2 shows the typical 1D and 2D spectra of one of our target galaxies. The majority (61/76) of our sample galaxies have [O III] detected with SNR$\gtrsim$10. 55, 35, and 15 within the entire sample have SNR$\gtrsim$5 detections of [O II], Hβ, and Hγ, respectively. For galaxies at $z \leq 1.6$, we also typically have access to their Hα[5] and [S II], which help constrain metallicity and nebular extinction. The best-fit redshifts and observed emission line fluxes for all our sources are presented in Table 3.

3.2. *Emission line maps*

In addition to the measurements of integrated emission line fluxes, another key piece of information that we need to retrieve from grism spectroscopy is the spatial distribution of emission line surface brightnesses, i.e., the emission line maps. The *HST* WFC3 near-infrared grisms have limited spectral resolution: for point sources, R~210 and 130, for G102 and G141, respectively. Yet this is actually an advantage in obtaining emission line maps. Since the instrument full-width half-maximum (FWHM) is equivalently ~700 km/s for G102, and ~1200 km/s for G141, it is reasonable to assume that the source 1D spectral shapes and 2D emission line maps are not affected by any kinematic motions of gas ionized by the star-forming regions, where outflows typically have speed <500 km/s (see e.g. Erb 2015, for a recent review). However, our sample galaxies are selected to be spatially extended, having their half-light radius $R_{50} \gtrsim 0\farcs25$, measured from their continuum morphology in the H_{160}-band imaging acquired by *HFF* or *CLASH*. Their spatial profiles along the light dispersion direction are convolved onto the wavelength axis, resulting in severe morphological broadening of the line-spread function FWHM (van Dokkum et al. 2011). This morphological broadening effect is already taken into account when estimating the best-fit grism redshift from the spectral template synthesis process described in Sect. 3.1. It also poses a great challenge for obtaining spatial 2D maps of emission lines that have very close rest-frame wavelengths, in particular the line complex of Hβ +[O III] $\lambda\lambda$4960,5008 doublets.

We hence develop a custom technique to deblend the line complex as follows. First, we measure the source broad-band isophotes that encompass over 90% of the surface brightness in JH_{140} and Y_{105}-band, and overlay them on top of the source 2D G141 and G102 spectra respectively. The 2D grism spectra are standard data products produced by our GRIZLI reduction with contamination and source continuum removed. The positions of the overlaid isophotes on the 2D grism spectra mark the locations of the redshifted emission lines (see the middle and bottom rows of Fig. 3). We rely on the pre-imaging (i.e. JH_{140} and Y_{105}) paired with the grism (i.e. G141 and G102) observations to measure the isophotes because they cover similar wavelength range, share comparable PSF properties, and are acquired at the same PA of the telescope. In this step, the grism spectra taken at different PAs have to be processed separately, since the morphological broadening varies drastically amongst different PAs if the source has asymmetric radial profiles. This broad-band isophote is used as an aperture for emission line map extraction. Since the red (i.e. more to the right on the wavelength axis in 2D spectra) portion of the aperture centered at the redshifted [O III] λ5008 is not contaminated by [O III] λ4960 and the flux ratio between the [O III] doublets is fixed ($f_{\text{[O III] 5008}}/f_{\text{[O III] 4960}}$ = 2.98:1, calculated by Storey & Zeip-

---

[3] https://github.com/gbrammer/grizli/

[4] Specifically, step 1) includes bad-pixel/persistence masking, bias correction, dark subtraction, cosmic ray flagging, relative/absolute astrometric alignment, flat fielding, master/variable sky background subtraction, geometric distortion correction, extraction of source catalogs and segmentation images at visit levels.

[5] 31 out of the 37 sources in this redshift range have Hα detected with SNR$\gtrsim$10.

Table 1. Summary of the *HST* observations presented in this work

Cluster Field	Cluster Alias	Cluster Redshift	R.A. (deg.)	Decl. (deg.)	Grism PA[a] (deg.)	*HST* imaging	$N_{\rm source}$[b]
Abell 370	A370	0.375	02:39:52.9	-01:34:36.5	155, 253	*HFF*	7
Abell 2744	A2744	0.308	00:14:21.2	-30:23:50.1	135, 233	*HFF*	13
MACS0416.1-2403	MACS0416	0.420	04:16:08.9	-24:04:28.7	164, 247	*HFF*/*CLASH*	9
MACS0717.5+3745	MACS0717	0.548	07:17:34.0	+37:44:49.0	020, 280	*HFF*/*CLASH*	5
MACS0744.9+3927	MACS0744	0.686	07:44:52.8	+39:27:24.0	019, 104	*CLASH*	6
MACS1423.8+2404	MACS1423	0.545	14:23:48.3	+24:04:47.0	008, 088	*CLASH*	9
MACS2129.4-0741	MACS2129	0.570	21:29:26.0	-07:41:28.0	050, 328	*CLASH*	10
RXJ1347.5-1145	RXJ1347	0.451	13:47:30.6	-11:45:10.0	203, 283	*CLASH*	2
RXJ2248.7-4431	RXJ2248	0.348	22:48:44.4	-44:31:48.5	053, 133	*HFF*/*CLASH*	5
MACS1149.6+2223[c]	MACS1149	0.544	11:49:36.3	+22:23:58.1	032, 111, 119, 125	*HFF*/*CLASH*	10

NOTE—Here we only list the primary pointings of the analyzed *HST* slitless spectroscopy, covering the cluster centers with WFC3/NIR grisms.

[a] The position angles (PAs) are represented by the "PA_V3" values reported in the corresponding raw image headers. The PA of the actual dispersion axis of slitless spectroscopy, in degrees east of north, is given by $\rm PA_{disp} \approx PA\_V3 - 45.2$. For each one of the *GLASS* PAs (i.e. excluding PAs 111 and 119 for MACS1149), 2 orbits of G141 and 5 orbits of G102 exposures have been taken, amounting to ∼4.5 and ∼11 kilo-seconds science exposure times for G141 and G102 respectively.

[b] The number of galaxies in which we secure sub-kpc resolution metallicity gradient measurements from *HST* spectroscopy.

[c] The detailed analyses of gradient measurements have already been presented in our earlier paper (Wang et al. 2017). Here we update the SED fitting results associated with these galaxies.

pen (2000)), we can obtain the same red portion of the clean [O III] λ4960 2D map. This red part of [O III] λ4960 map is contaminating slightly bluer part of the [O III] λ5008 map, and can be subtracted off, with flux errors properly propagated, therefore yielding cleaned [O III] λ5008 flux in those slightly bluer areas within the extraction aperture. This procedure is then conducted iteratively, until the [O III] λ4960 fluxes in all spatial pixels within the aperture have been removed, and clean 2D maps of [O III] λ5008 and Hβ can be obtained, *at individual PAs*. Finally, we use ASTRODRIZZLE (Gonzaga 2012) to combine the clean [O III] λ5008 and Hβ maps extracted at multiple PAs. The resultant 2D stamps are drizzled onto a 0.″06 grid, Nyquist sampling the FWHM of the WFC3 PSF, and astrometrically matched to the corresponding broad-band images. Notably, our custom deblending technique does not rely on any models of the spatial profiles of [O III] emission[6]. This is a critical procedure to account for the orient-specific contaminations of [O III] λ4960, which can be over 2-σ in some spatial areas within the extraction aperture (see the upper right panel of Fig. 3).

3.3. *Stellar mass*

We perform SED fitting to the broad-band photometry of our galaxies from the *HST* imaging data obtained by *HFF* or *CLASH*. The FAST software (Kriek et al. 2009) is used to infer stellar mass (M_*), star-formation rate (SFR$^{\rm S}$, see Sect. 3.5 for more details), and dust extinction of stellar continuum ($\rm A^S_V$), based on the Bruzual & Charlot (2003) (BC03) stellar population synthesis models. We assume the Chabrier (2003) initial mass function, constant star formation history, the Calzetti et al. (2000) extinction law, and fixed stellar metallicity being one-fifth solar. Since the majority of our galaxies show strong nebular emission in their rest-frame optical, we need to subtract their *nebular* emission from the corresponding broad-band fluxes to estimate more accurately the level of *stellar* continuum. We convolve the best-fit Gaussian profiles for each emission line at the source redshift with the *HST* bandpass throughput, to derive the nebular flux, and then subtract it from the measured broad-band photometry. In Table 3, we show the observed JH_{140}-band magnitude before this correction and the reduction factor, which is a ratio between the JH_{140}-band flux after and before correcting for nebular emission. We verify that this correction is es-

---

[6] We note that in the most up-to-date version of GRIZLI, the subtraction of [O III] λ4960 is implemented. However GRIZLI's automatic subtraction is based on a spatial model of [O III] λ4960 emission, which is different from our procedure presented here.

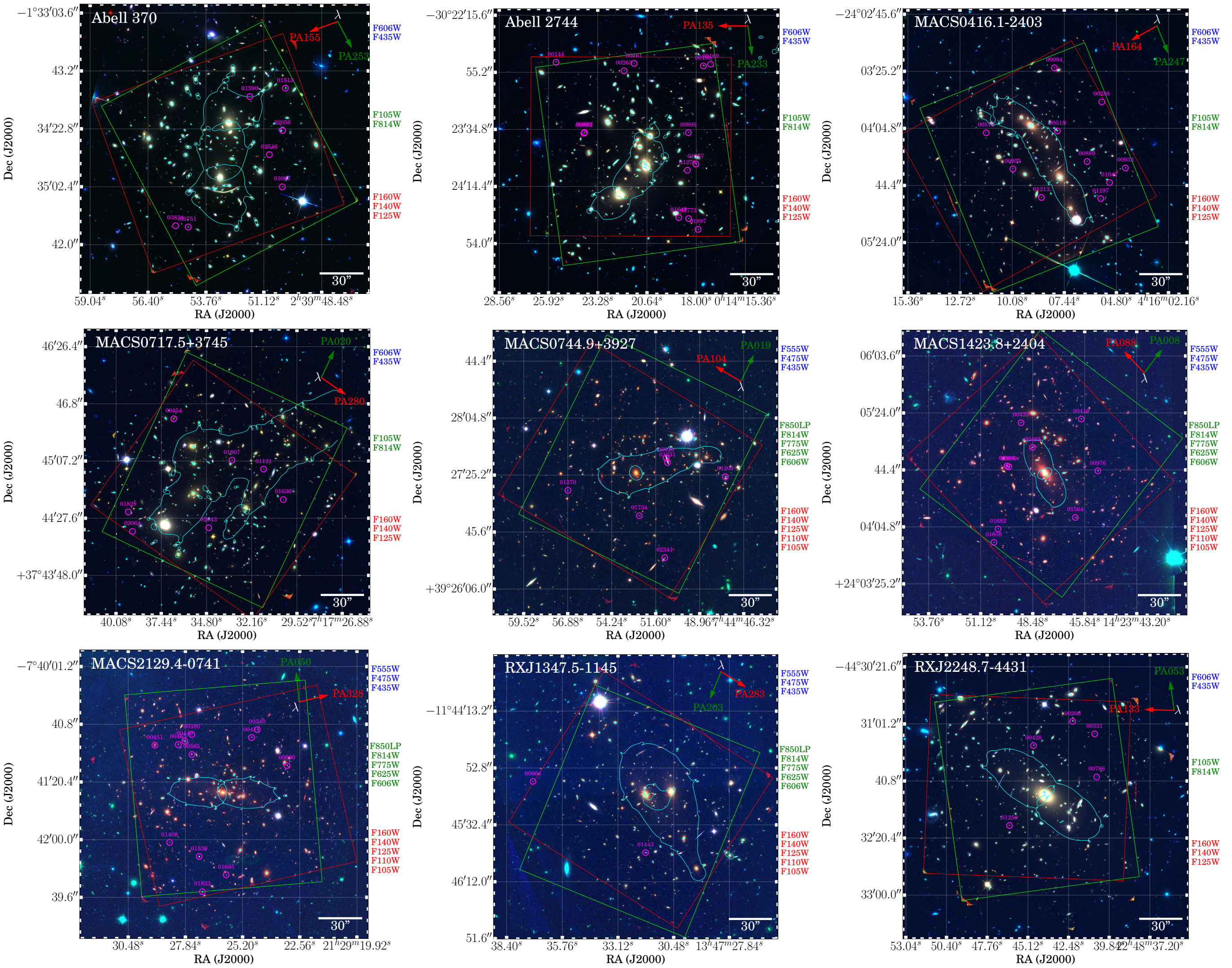

Figure 1. Color-composite images of the nine cluster center fields presented in this work (for the tenth field, i.e., MACS1149, see Fig. 1 of Wang et al. (2017)). The blue, green and red channels are stacked images from the *HFF*/*CLASH* mosaics taken at various filters, shown on the right to each panel. The footprints of *HST* WFC3 near-infrared grism pointings are denoted by the red and green squares, with the corresponding wavelength dispersion directions marked by the arrows in the same color in the upper right corner. The cyan contours represent the critical curves at sample median redshift ($z = 1.63$) predicted by our default macroscopic lens models (see Sect. 3.6). Our sources with sub-kpc resolution metallicity gradient measurements are marked by magenta circles.

sential for deriving reliable M_* estimates for galaxies on the low mass end ($M_* < 5 \times 10^9 M_\odot$); without this correction M_* can be over-estimated by as much as 0.7 dex. We present the results of our stellar continuum SED fitting in Table 3. Thanks to lensing magnification, our sample extends significantly into the low-mass regime at high z, highly complementary to the targets from ground-based surveys (e.g., *KMOS*$^{\rm 3D}$, Wuyts et al. 2016).

3.4. *AGN contamination*

Before carrying out the metallicity inference on our sample, we check for contamination of active galactic nucleus (AGN) ionizations. In Fig. 4, we rely on the mass-excitation diagram to exclude AGN candidates from our sample. The demarcation scheme (Juneau et al. 2014) aims to separate AGN from star-forming galaxies, based on the SDSS DR7 emission-line galaxies at $z \sim 0$. This scheme has been shown to reproduce the bivariate distributions seen in a number of high-redshift galaxy samples out to $z \sim 1.5$ (Juneau et al. 2014). We therefore discard sources in our sample that are 2-σ away from the star-forming region in the diagram, given the measurement uncertainties on M_* and [O III]/Hβ. To examine possible redshift-dependent trends in the future Sections, we subdivide our sample into three bins: 37, 24, and 15 galaxies at $z \in [1.2, 1.6]$, $z \in [1.6, 1.9]$, and $z \in [1.9, 2.3]$, respectively, marked by different symbols in Fig. 4.

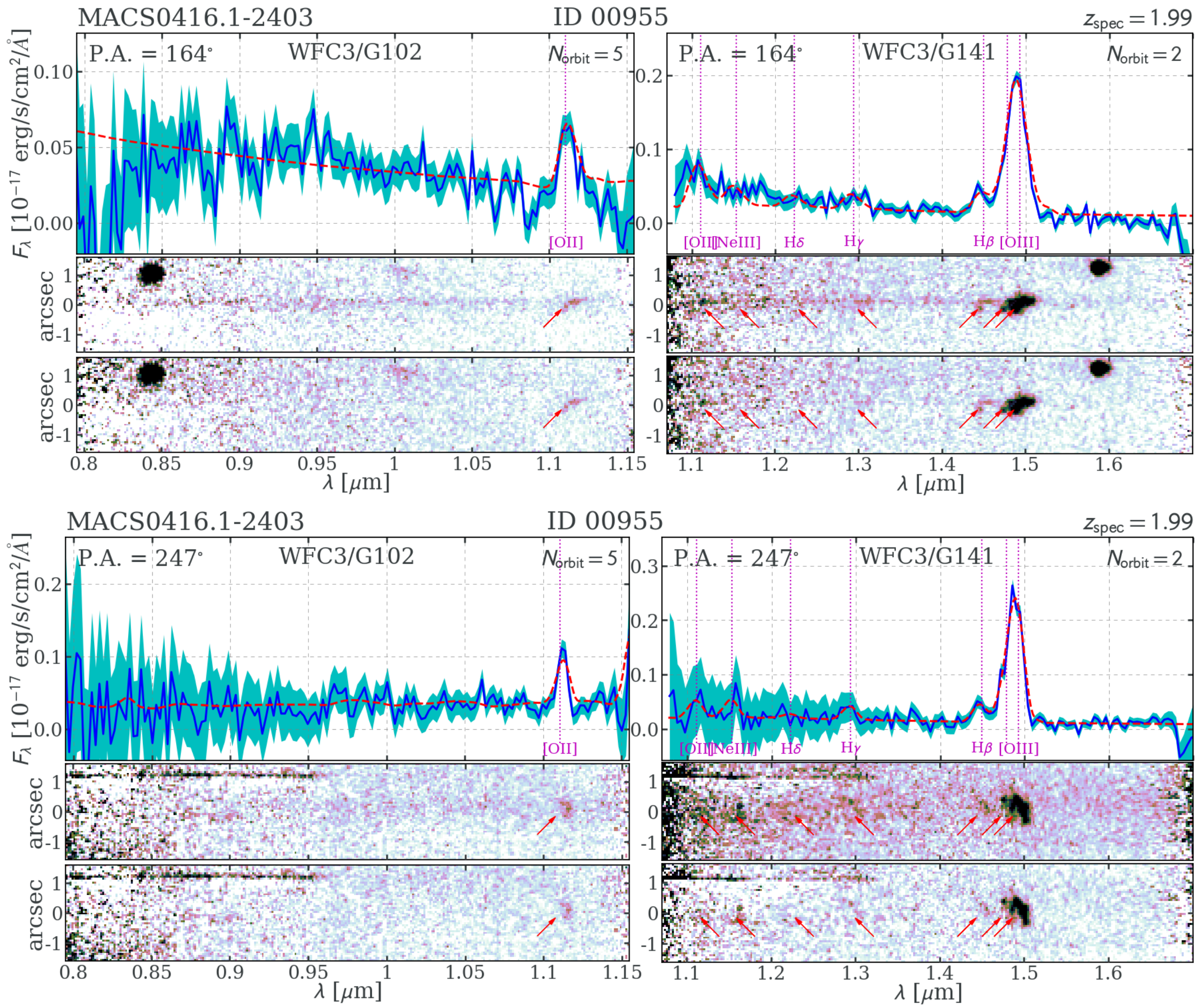

Figure 2. The *HST* grism spectra for one exemplary object in our sample, MACS0416-ID00955 at $z \sim 2$. The total on-target exposure time is equally split between two nearly orthogonal P.A.s (shown in the two sub-figures), reaching 5 orbits of G102 and 2 orbits of G141 exposures per P.A.. In each sub-figure, we show the optimally extracted 1D spectra and the full 2D spectra without and with source stellar continuum subtraction, for both grism channels. The 1D observed F_λ flux and its 1-σ uncertainty are represented by the blue solid lines and the cyan shaded bands, respectively. The wavelengths of the nebular line emission features are marked by magenta vertical dotted lines and red arrows, in 1D and 2D spectra respectively. The red dashed curves show the 1D model spectra, combining both stellar continuum (given by spectral template synthesis) and nebular line emission (modeled as Gaussian profiles), *after* the source morphological broadening is already taken into account. We emphasize that the same best-fit spectral model is used for each individual source, yet the differences in continuum shape and flux levels at the two P.A.s are originated from the varying source morphological kernels along the two light dispersion directions.

Moreover, Coil et al. (2015) found that a +0.75 dex shift in M_* of the demarcation curves is necessary to match the loci of AGNs and star-forming galaxies in the MOSDEF surveys at $z \sim 2.3$, to account for the redshift evolution of the mass-metallicity relation. On part of the sample, we also obtained Hα gas kinematics from the ground-based Keck OSIRIS observations (Hirtenstein et al. 2018). The integrated measurement of $f_{\rm [N\,II]}/f_{\rm H\alpha}$ is typically $\lesssim$0.1 at 3-σ confidence level, indicative of star-forming regions with no significant AGN contamination. We thus verify that there is no sign of significant AGN ionization in our sample.

3.5. *Star-formation rate*

We have two methods for estimating star-formation rate (SFR). First of all, SFR can be obtained from the stellar continuum SED fitting outlined in Sect. 3.3. This method is sensitive to the underlying assumptions of star-formation history and stellar population synthesis models adopted in the

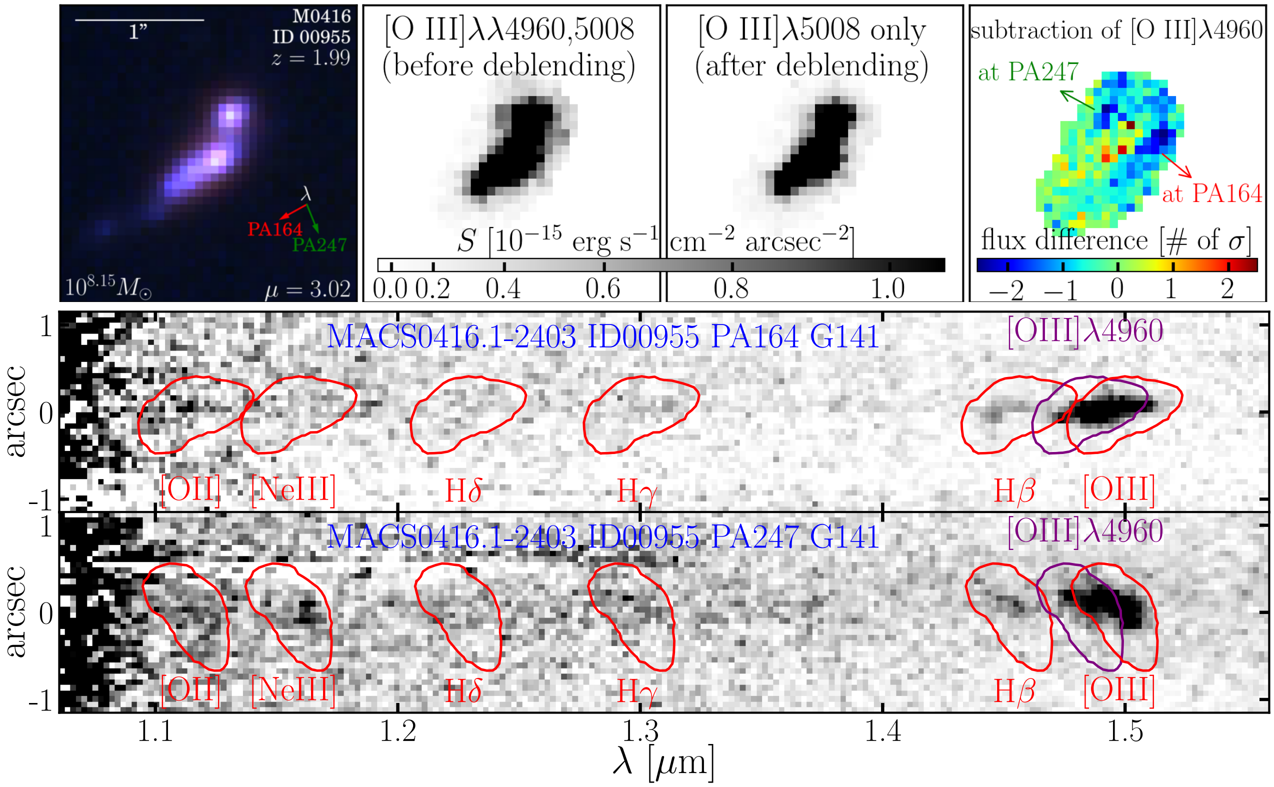

Figure 3. Our custom technique of obtaining pure [O III] λ5008 maps combined from multiple orients of grism exposures. **Top**, from left to right: the color-composite image of object MACS0416-ID00955 (a $z\sim2$ dwarf galaxy with $M_*\simeq10^8 M_\odot$), its [O III] map before deblending the [O III] doublets, its pure [O III] λ5008 map clean from the partial contamination of [O III] λ4960 at two orients (PA164 and PA247), and the significance of difference between these two [O III] maps. The significance is expressed as the flux differences divided by the corresponding flux uncertainties (i.e. σ) of [O III] λ5008 in each spatial pixel. **Middle and bottom**: 2D contamination and continuum subtracted G141 spectra of this dwarf galaxy at two orients (PA164 and PA274) separately. Note that these 2D traces are basically cutouts from the continuum subtracted G141 spectra presented in Fig. 2. Due to the limited spectral resolutions of *HST* grisms and extended source morphology, fluxes of [O III] λ4960 are blended into [O III] λ5008 and Hβ in a spatially inhomogeneous fashion, specific to the light dispersion direction at individual orients.

fitting procedure. Hereafter, we refer to these measurements as SFR$^{\rm S}$.

Secondly, SFR can be derived from nebular emission after correcting for dust attenuation. From our Bayesian inference method presented in Sect. 3.6, we obtain posterior probability distributions of the de-reddened Hβ flux, which can be converted to the intrinsic Hα luminosity given source redshift. As a consequence, SFR (hereafter denoted as SFR$^{\rm N}$) can then be calculated following the widely used calibration (Kennicutt 1998), i.e.,

$$\mathrm{SFR}^{\rm N} = 4.6\times10^{-42}\frac{L(\mathrm{H}\alpha)}{\mathrm{erg/s}}\ (M_\odot/\mathrm{yr}), \tag{1}$$

appropriate for the Chabrier (2003) initial mass function. Unlike the measurements from SED fitting, this method provides a proxy of instantaneous star-forming activities on the time scale of ~10 Myrs. This short time scale is relevant to probe the highly dynamic feedback processes which are effective in re-distributing metals (see e.g., Hopkins et al. 2014). Therefore, we quote the values of SFR$^{\rm N}$ as our fiducial SFR measurements if not stated otherwise.

We note that for our low-z sample (37 galaxies at $z \in [1.2, 1.6]$), Hα is covered by the WFC3/G141 grism. However, due to the low spectral resolution, it is heavily blended with [N II]. We hence rely on the empirical prescription of Faisst et al. (2017) to subtract the contribution of [N II] fluxes from the measured Hα flux, based on stellar mass and redshift of our galaxies (see Table 3 for the calculated [N II]/Hα flux ratios). This ensures a more reliable estimate of SFR$^{\rm N}$, less impacted by dust than the Hβ-based measurements.

On the left panel of Fig. 5, we show the loci of our galaxies in the diagram of SFR vs. M_*. By selecting lensed galaxies via their nebular emission line flux, our sample reaches an instantaneous SFR limit of $\sim1\ M_\odot$/yr at $z\sim2$. In comparison to mass-complete samples (from e.g., the *KMOS*$^{\rm 3D}$ survey, Wuyts et al. 2016) and galaxies from the star-forming main sequence (SFMS, Speagle et al. 2014; Whitaker et al. 2014), we push the exploration of star-forming galaxies at the cosmic noon by 1-2 dex deeper into the low-mass regime. We also show the loci of the spectral stacks from the WFC3 Infrared Spectroscopic Parallel (WISP) Survey (Henry et al.

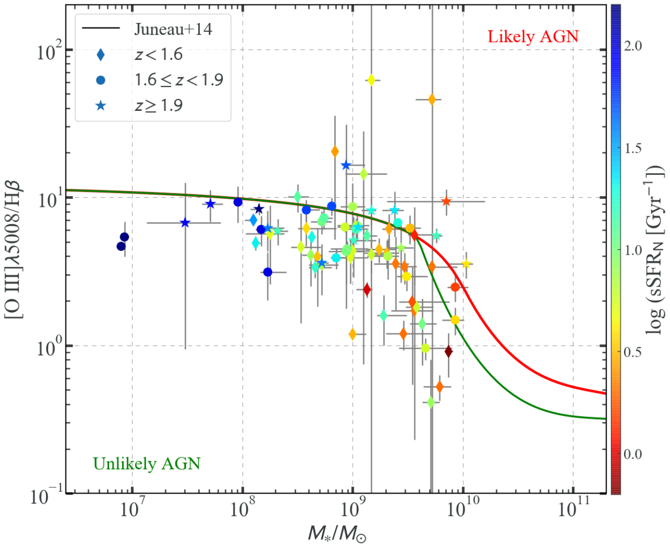

Figure 4. Mass-excitation diagram for our galaxies. The demarcation curves are from Juneau et al. (2014) based on the $z \sim 0$ SDSS DR7 emission-line sample: AGNs are located mainly above the red curve, star-forming galaxies are located below the green curve, and AGN/star-forming composites are in between. Our entire sample is separated into three redshift bins: $z < 1.6$ (37 sources), $1.6 \leq z < 1.9$ (24 sources), and $z \geq 1.9$ (15 sources), color-coded in sSFR. We show that the majority of our sources are located below the green curve, where the possibility of being classified as AGNs is low (<10%).

2013), very close to that of our galaxies given similar observing strategies. We gain over 1 dex in M_* thanks to lensing magnification and the 14-orbit depth of the *GLASS* data in each field.

3.6. *Metallicity and its radial gradient*

Following our previous work (Wang et al. 2017, 2019), we adopt a *forward-modeling* Bayesian method to infer simultaneously metallicity (12 + log(O/H)), nebular dust extinction ($\mathrm{A_V^N}$) and de-reddened Hβ flux ($f_{\mathrm{H}\beta}$), based on observed emission line fluxes directly, as measured in Sect. 3.1. We use flat priors for $12 + \log(\mathrm{O/H})$ and $\mathrm{A_V^N}$, in the range of [7.0, 9.3] and [0, 4], respectively, which are appropriate for the Maiolino et al. (2008) strong line calibrations adopted in our inference. For $f_{\mathrm{H}\beta}$, we use the Jeffrey's prior in the range of [0, 1000], in unit of $10^{-17}\mathrm{erg\ s^{-1}\ cm^{-2}}$. The MCMC sampler EMCEE is used to explore the parameter space, with the likelihood function defined as

$$\mathrm{L} \propto \exp(-\chi^2/2) = \exp\left(-\frac{1}{2}\cdot\sum_i \frac{\left(f_{\mathrm{EL}_i} - R_i \cdot f_{\mathrm{H}\beta}\right)^2}{(\sigma_{\mathrm{EL}_i})^2 + \left(f_{\mathrm{H}\beta}\right)^2 \cdot (\sigma_{R_i})^2}\right). \tag{2}$$

Here EL_i represents each of the available emission lines, among the set of [O II], Hγ, Hβ, [O III], Hα, [S II]. f_{EL_i} and σ_{EL_i} denote the EL_i flux and its uncertainty, de-reddened given a value of A_V^N drawn from the MCMC sampling. The Cardelli et al. (1989) galactic extinction law with R_V =3.1 is adopted to correct for dust reddening. R_i is the expected flux ratio between EL_i and Hβ, with σ_{R_i} being its intrinsic scatter. The content of R_i varies from strong-line diagnostic to Balmer decrement depending on the associated EL_i. In practice, if EL_i is one of the Balmer lines, R_i is given by Hα/Hβ = 2.86 and Hγ/Hβ = 0.47, i.e., the Balmer decrement ratios assuming case B recombination under fiducial HII region situations. Instead, if EL_i is one of the oxygen collisionally excited lines, we take the strong-line flux ratios (i.e. $f_{[\mathrm{O\,III}]}/f_{\mathrm{H}\beta}$ and $f_{[\mathrm{O\,II}]}/f_{\mathrm{H}\beta}$) calibrated by Maiolino et al. (2008) as R_i. Last, if EL_i is [S II], we rely on our strong-line calibration of [S II]/Hα presented in Wang et al. (2017).

This forward-modeling approach is superior to converting emission line flux ratios (e.g., R_{23}, O_{32}) to metallicity, because it properly takes into account any weak nebular emission that falls short of the detection limit, and avoids double counting information as it happens when combining multiple flux ratios that involve the same line. All sources in our sample have SNR≳10 in at least one of the oxygen collisionally excited lines and/or Hα (if source redshift is $z \lesssim 1.6$), yet the Hβ detection is usually not as strong given its intrinsic faintness. By not calculating observed emission line flux ratios but forward modeling observed line fluxes directly, we avoid compromising the high SNR detections of the bright [O III] and [O II] lines by the faint Hβ lines. As a result, our forward-modeling methodology improves our ability of accurate metallicity inference based on high SNR detections of strong nebular lines (i.e. [O III] and [O II]), and does not necessarily require high SNR detections of faint emission lines. In the left panel of Fig. 6, we show the joint constraints on (12 + log(O/H), $\mathrm{A_V^N}$, $f_{\mathrm{H}\beta}$), derived from the observed integrated emission line fluxes for an exemplary object MACS0416-ID00955, whose 1D/2D spectra are shown in Figs. 2 and 3. Together we also simulate a scenario for this observation with much worse SNR detection of Hβ, i.e., artificially increasing the observed Hβ uncertainty by a factor of 10 while keeping other measurements unchanged. It is found that the resultant constraint on 12 + log(O/H) for this simulated scenario stays similar. This test demonstrates that our metallicity inference method can still ensure reasonable constraints on 12 + log(O/H), even in cases where some emission lines such as Hβ are only marginally detected. In the right panel of Fig. 6, we show the histograms of metallicity inferences (median values) given by our forward-modeling technique, in all individual Voronoi cells from our entire galaxy sample. We divide all these metallicity measurements in terms of the observed SNR of Hβ in the corresponding Voronoi cells. Regardless of Hβ SNR, the three histograms all peak at $12 + \log(\mathrm{O/H}) \sim 8.0$, consistent with the integrated

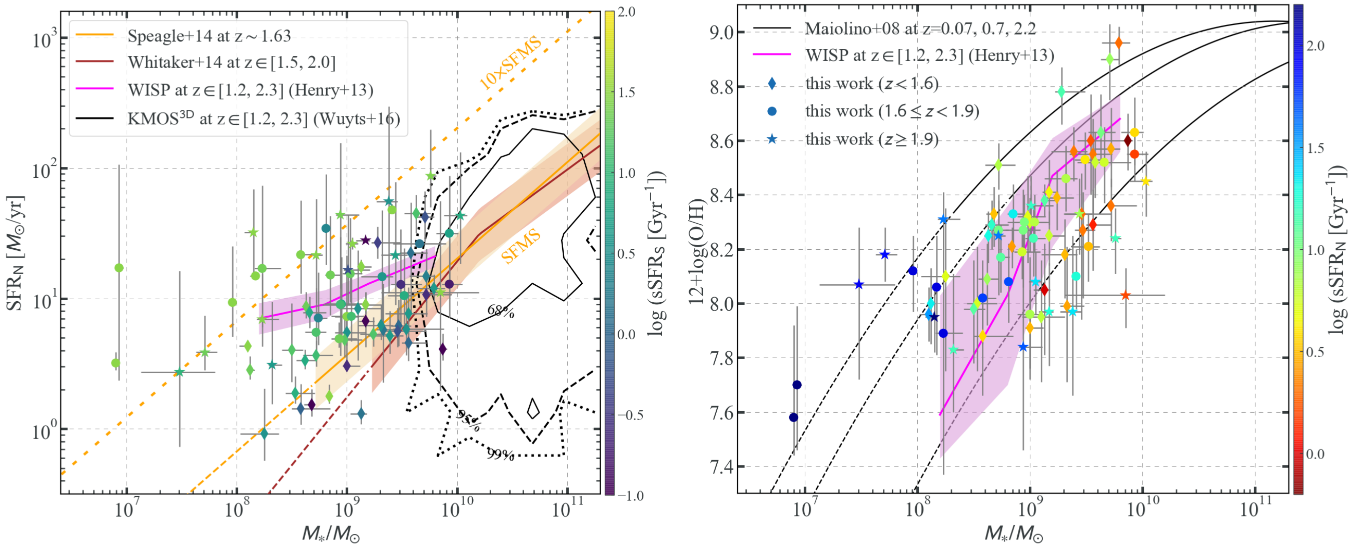

Figure 5. Global properties of our sample. **Left**: SFR as a function of M_* for galaxies at cosmic noon. Our galaxies are represented by the symbols following the scheme in Fig. 4 corresponding to different z bins. However the color coding reflects the specific SFR derived from stellar continuum SED fitting, after subtracting emission line fluxes (see Sect. 3.3). The loci of our galaxies are consistent with that of the WISP survey (Henry et al. 2013), if the SFR inferred from dust-corrected nebular emission is adopted. We also show that in terms of mass coverage, our sample is highly complementary to the ground-based mass-complete sample of *KMOS*^{3D}, which can only probe down to $\sim 5 \times 10^9 M_\odot$ at $z \sim 2$. **Right**: mass-metallicity relations for high-z galaxies. The symbols of our sample now have the same color-coding as in Fig. 4. Our galaxies follow similar trends of the MZRs from the WISP survey and Maiolino et al. (2008). In the low mass regime ($M_* \lesssim 10^8 M_\odot$), our galaxies are more metal enriched than the simple extensions of those MZRs. These metal-enriched galaxies also have higher sSFR than the sample average.

metallicity measurements from other work in similar ranges of redshift and mass (see e.g. Fig. 5 and Maiolino et al. 2008; Henry et al. 2013). From this test, we show that there is no systematic offset of the distribution of inferred metallicities among the three groups divided by Hβ SNR, and our metallicity estimates do not simply revert to the prior used in our Bayesian inference.

Our forward-modeling Bayesian inference is first performed on the integrated emission line fluxes measured for each galaxy, to yield global metallicity. On the right panel of Fig. 5, we show the mass-metallicity relation (MZR) from our sample, color-coded by the specific SFR (sSFR = SFR/M_*) obtained from the aforementioned analyses. We also overlay the MZR from the WISP survey derived using the same strong-line calibrations (Henry et al. 2013). It is encouraging to see that the two MZRs follow similar trends, due to similar source selection technique and observing strategy. Notably, our galaxies at the extreme low-mass end ($M_* \lesssim 10^9 M_\odot$) show both elevated metallicity and sSFR. This is consistent with the hypothesis that these low-mass systems are in the phase of early mass assembly with efficient metal enrichment and minimum dilution from pristine gas infall.

In addition to the integrated emission line fluxes, from the procedures described in Sect. 3.2, we also obtain 2D spatial distributions of emission line surface brightnesses. We utilize Voronoi tessellation as in Wang et al. (2019) to divide spatial bins with nearly uniform SNRs of the strongest emission line available (usually [O III]). Our spatially resolved analysis based on Voronoi tessellation is superior to averaging the signals in radial annuli, because of azimuthal variations (as large as 0.2 dex) in metallicity spatial distribution in nearby spiral galaxies (Berg et al. 2015; Ho et al. 2017). Our Bayesian inference is then executed in each of the Voronoi bins for all sources, yielding their metallicity maps at sub-kpc resolution.

To get the intrinsic deprojected galactocentric distance scale for each Voronoi bin, we conduct detailed reconstructions of the source-plane morphology of each galaxy in our sample. We first obtain a 2D map of stellar surface density (Σ_*, e.g., as shown in Fig. 7) for each source through pixel-by-pixel SED fitting following the prescription described in Sect. 3.3. Then the pixels in this map are ray-traced back to their source plane positions, according to the deflection fields given by the macroscopic cluster lens models. For all the *HFF* clusters, we use the SHARON & JOHNSON version 4corr models (Johnson et al. 2014). For the *CLASH*-only clusters except RXJ1347, we use the Zitrin PIEMD+eNFW version 2 model. For RXJ1347, we use our own model built following closely the approach in Johnson et al. (2014). To this delensed 2D Σ_* map, we fit a 2D elliptical Gaussian function, to determine the galaxy's inclination, axis ratio, and major axis orientation, so that the source intrinsic morphology is recovered from lensing distortion.

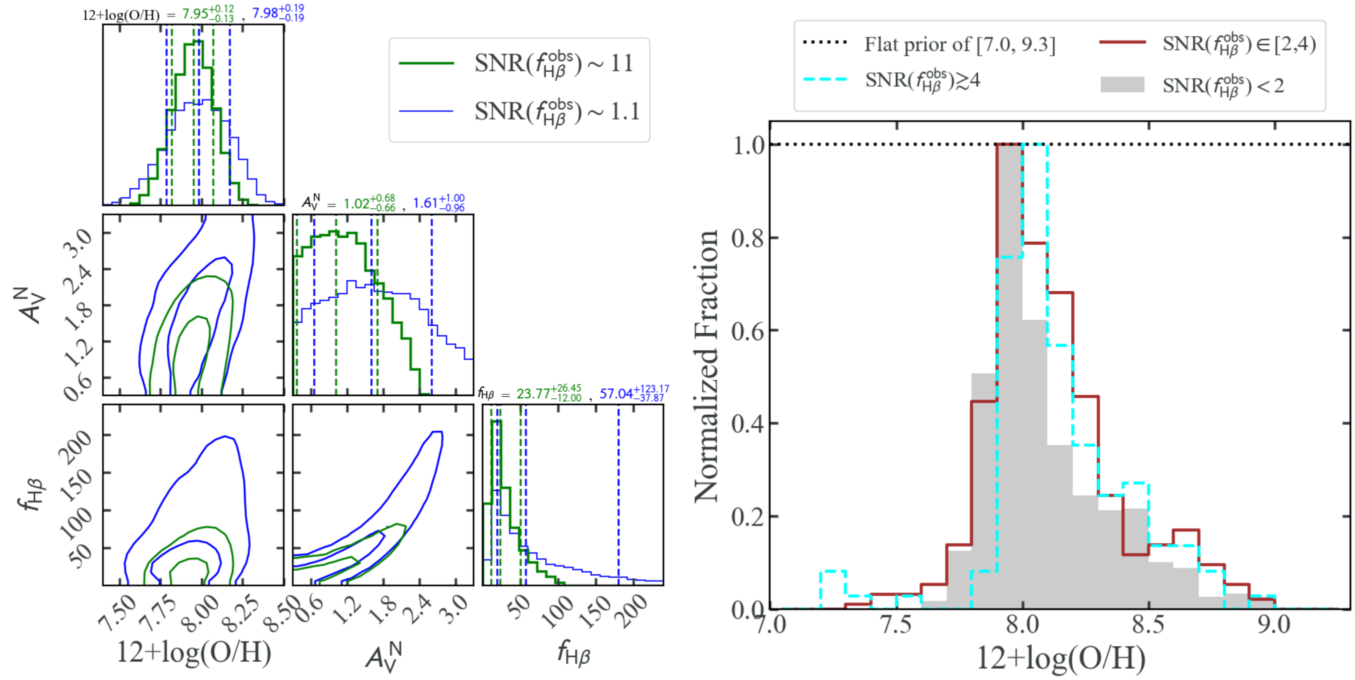

Figure 6. Rigorous constraint on metallicity from our forward-modeling Bayesian inference method. **Left**: marginalized 1D/2D constraints on metallicity (12 + log(O/H)), nebular dust extinction (A_V^N) and de-reddened Hβ flux ($f_{H\beta}$) based on the integrated emission line fluxes of object MACS0416-ID00955, presented in Table 3 (also see Figs. 2 and 3). The parameter inference values shown on top of each column are medians with 1-σ uncertainties drawn from the [16, 50, 84] percentiles, marked by the vertical dashed lines in the 1D histograms. The green color corresponds to the inference from the actual observed emission line fluxes where Hβ is detected at SNR∼11 (i.e. $f^{obs}_{H\beta} = 6.88 \pm 0.60$). The blue-colored results are derived with the uncertainty of Hβ artificially increased by a factor of 10 (i.e. SNR∼1.1), and other emission line flux measurements unchanged. The comparison between the green and blue colored results shows that although the constraints on A_V^N and $f_{H\beta}$ are severely worsened by the decrease in SNR of Hβ, the inference on 12 + log(O/H) remains largely unchanged. This comparison thereby testifies that our forward-modeling Bayesian inference of metallicity does not require high SNR detection of Hβ. **Right**: histograms of median metallicities measured using our forward-modeling method, in all individual Voronoi cells from our entire galaxy sample. The distribution of metallicity measurements is divided into three groups corresponding to three different ranges of Hβ observed SNR in the corresponding Voronoi cells. The horizontal dotted line overlaid shows the flat prior of $12 + \log(O/H) \in [7.0, 9.3]$ used in our Bayesian inference. We demonstrate that the returned metallicity estimates do not simply revert to the prior and there is no systematic offset in our metallicity inference, even in the low SNR regime of Hβ.

Since we have measured both metallicity and source-plane de-projected galactocentric radius for each Voronoi bin, we can estimate a radial gradient slope via linear regression (see Appendix A for the gradient measurements based on metallicities derived in *source-plane* Voronoi bins and related discussions about the effect of anisotropic lensing distortion). Fig. 7 demonstrates the entire process for measuring the metallicity radial gradient of a $z \sim 2$ star-forming dwarf galaxy. As a sanity check, we also measure its radial gradient using metallicity inferences derived in each individual spatial pixel and radial annulus. We verified that the differences among the three methods are ≲0.03 dex/kpc, within the measurement uncertainties.

In the end, we secure a total of 76 galaxies in the redshift range of $1.2 \lesssim z \lesssim 2.3$ with sub-kpc resolution metallicity gradients (see Table 1 for the numbers of sources in individual cluster center fields). This is hitherto the largest sample of such measurements in the distant Universe. This sample enables robust measures of both average gradient slopes and scatter in the population.

4. THE COSMIC EVOLUTION OF METALLICITY GRADIENTS AT HIGH REDSHIFTS

In this section, we collect published results on radial gradients of metallicity measured in the distant Universe. We focus on the measurements that are derived with sub-kpc resolution, because insufficient spatial sampling is shown to cause spuriously flat gradient measurements (Yuan et al. 2013). This poses a real challenge for ground-based observations, given the optimal seeing condition is ∼0.″6, equivalent to 5 kpc at $z \sim 2$. There have been a number of attempts to overcome this beam smearing through correcting the distorted light wave front with the adaptive optics (AO) technique. Using the *SINFONI* instrument on the *VLT* under the AO mode, Swinbank et al. (2012) measured 7 gradients at $z \sim 1.5$. Following the same strategy, Förster Schreiber et al. (2018) expanded the sample by adding 21 new mea-

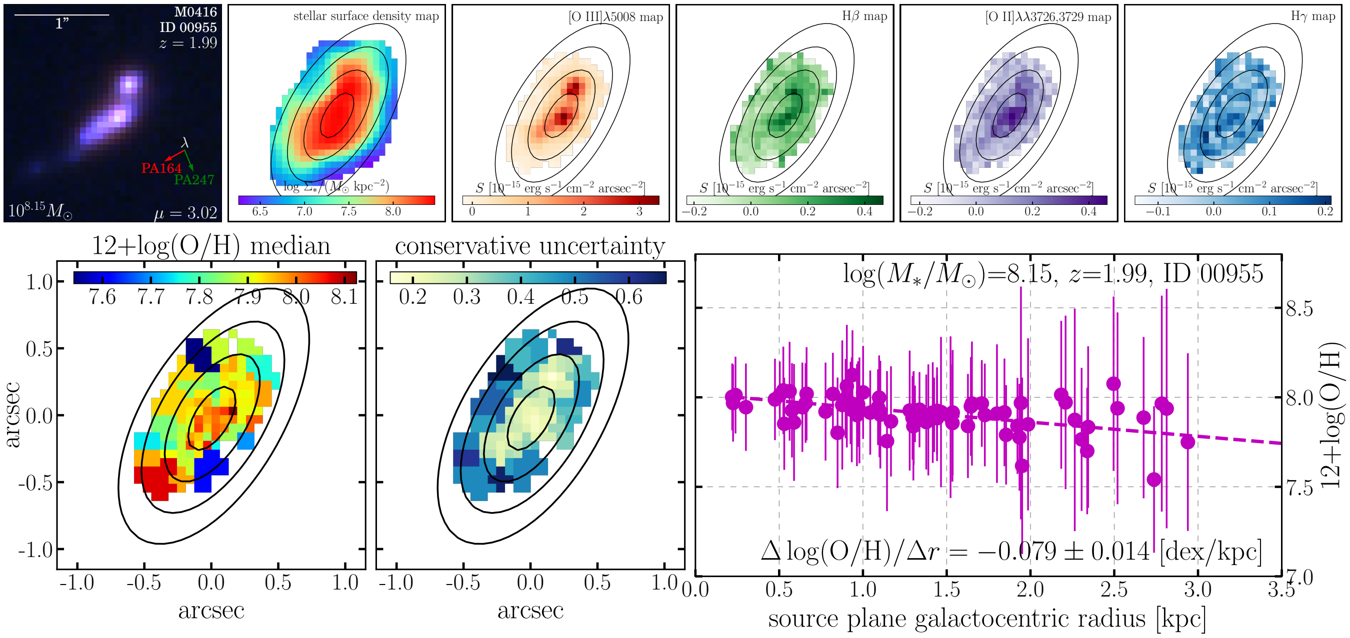

Figure 7. A $z\sim2$ star-forming dwarf galaxy ($M_*\simeq10^8M_\odot$) with a negative metallicity radial gradient, similar to that measured in our Milky Way (i.e., −0.07 ± 0.01, Smartt & Rolleston 1997). We show this as an example of the analysis procedures applied to our entire sample. **Top**, from left to right: color composite stamp (from the *HFF* imaging), stellar surface density (Σ_*) map (obtained from pixel-by-pixel SED fitting to *HFF* photometry), and surface brightness maps of emission lines [O III], Hβ, [O II], and Hγ. We use the technique demonstrated in Fig. 3 to obtain pure [O III] λ5008 and Hβ maps for the source. The black contours mark the de-lensed de-projected galacto-centric radii with 1 kpc interval, given by our source plane morphological reconstruction described in Sect. 3.6. **Bottom**: metallicity map and radial gradient determination for this galaxy. The weighted Voronoi tessellation technique (Cappellari & Copin 2003; Diehl & Statler 2006) is adopted to divide the surface into spatial bins with a constant SNR of 5 on [O III]. In the right panel, the metallicity measurements in these Voronoi bins are plotted as magenta points. The dashed magenta line denotes the linear regression, with the corresponding slope shown at the bottom. The spatial extent and orientation remain unchanged throughout all the 2D maps in both rows, with north up and east to the left.

surements at $z\sim2$ from the SINS/zC-SINF survey[7]. Lensing can also help increase the spatial sampling rate. Jones et al. (2010, 2013) brought forward this approach by securing 4 gradients at $z\sim2$ in galaxy-galaxy lensing systems using the AO-assisted *OSIRIS* instrument on the *Keck* telescope, with resolution further boosted $\gtrsim$3x by lensing magnification. Leethochawalit et al. (2016) carried out similar analyses and measured 11 new gradients at similar redshifts. To recap, there exist a total of 43 metallicity gradient measurements with sub-kpc spatial resolution at cosmic noon before our work.

In this work, we *triple* the sample size by presenting 76 sub-kpc resolution metallicity radial gradients in star-forming galaxies at cosmic noon. This is by far the largest homogeneous sample with sufficient spatial resolution, which enables a uniform analysis. In Fig. 8, our results are highlighted by three sets of symbols — corresponding to the three z sub-groups — color-coded in sSFR. From a total of 76 galaxies in our sample with sub-kpc resolution gradient measurements, there are 15 and 7 sources showing negative and positive (i.e. inverted) gradients greater than 2-σ away from being flat, respectively. At 3-σ confidence level, the number of galaxies showing negative and inverted gradients are 7 and 3, respectively. Notably, two of the 3 inverted gradients (A370-ID03751 and MACS0744-ID01203) have already been reported in detail in Wang et al. (2019). All individual ground-based measurements at similar resolution ($\lesssim$kpc scale) are represented by magenta squares. Recently Curti et al. (2020) analyzed the *KMOS* observations in the field of RXJ2248, and measured metallicity gradients in 12 background galaxies lensed by RXJ2248, out of which three are in overlap with our sample (i.e. ID00206, ID00428, ID01205). We verified that the gradient results measured from both works are compatible at 1-σ confidence level. It is encouraging to see that the metallicity gradients derived using different methods and datasets are in good agreement.

Some theoretical trends are overlaid in Fig. 8. In particular, two numerical simulations with different galactic feedback strengths but otherwise identical settings by Gibson et al. (2013) are shown as the orange curves. The comparison between these two trends demonstrates that enhanced feed-

---

[7] Note that Förster Schreiber et al. (2018) only published the radial gradients of [N II]/Hα measured in their sample galaxies. We convert those measurements into metallicity gradients following the widely adopted strong line calibration of Pettini & Pagel (2004).

back can be highly efficient in erasing metal inhomogeneity. Therefore resolved chemical properties, if measured accurately, can shed light on the strength of galactic feedback in the early phase of disk growth.

Fig. 8 also shows the spread of the *KMOS*^{3D} gradient measurements by Wuyts et al. (2016), which is highly clustered to flatness. Without AO support nor lensing magnification gain on the spatial sampling rate, these gradients are usually obtained at a FWHM angular resolution of $\sim0''.6$, imposed by the natural seeing. For a $z \sim 1.5$ star-forming galaxy with intrinsically negative metallicity gradient ($\Delta\log(\mathrm{O/H})/\Delta r = -0.16 \pm 0.02$ [dex kpc^{-1}]), Yuan et al. (2013) show that from seeing-limited observations with a FWHM angular scale of $\sim0''.5$, its radial metallicity gradient is instead measured to be $\Delta\log(\mathrm{O/H})/\Delta r = -0.01 \pm 0.03$ [dex kpc^{-1}]), significantly biased towards flatness caused by beam smearing. To mitigate the potential bias from beam smearing, Carton et al. (2018) conducted a forward-modeling analysis to recover 65 gradients at $0.1 \lesssim z \lesssim 0.8$ from the seeing-limited *MUSE* observations (marked in green in Fig. 8).

The 2-σ interval of the FIRE simulations (Ma et al. 2017) is shown as the grey-shaded region in Fig. 8. We see that the scatter predicted by the FIRE simulations matches well that from low-z observations (at $z \lesssim 1$, e.g., from Carton et al. 2018), but it is smaller by a factor of 2 at higher redshifts, especially at $z \gtrsim 1.3$. This likely reflects that galaxies display more diverse chemo-structural properties at the peak epoch of cosmic structure formation and metal enrichment, when star formation is more episodic and vigorous (see e.g.., Hopkins et al. 2014).

5. THE MASS DEPENDENCE OF METALLICITY GRADIENTS AT SUB-KPC RESOLUTION: TESTING THEORIES OVER 4 DEX OF M_*

With the sample statistics greatly improved, we can quantify the mass dependence of reliably measured metallicity gradients at high redshifts, as a test of theoretical predictions. The combined sample includes our 76 measurements at $z \in [1.2, 2.3]$, and 35[8] others' as given in Sect. 4. Following the same color/marker styles as in Fig. 8, we plot these high-resolution gradient measurements as a function of their associated M_* in Fig. 9. It is remarkable that now the observational data cover *four orders of magnitude* in M_*. Notably, over half of our gradient measurements reside in the dwarf mass regime ($M_* \lesssim 2 \times 10^9 M_\odot$), probing $\gtrsim$2 dex deeper into the low-mass end, compared with the ground-based AO results (magenta squares).

We perform linear regression on all these measurements of metallicity gradient and stellar mass, with errors on both quantities taken into account, using the following formula,

$$\Delta\log(\mathrm{O/H})/\Delta r\ [\mathrm{dex\ kpc^{-1}}] = \alpha + \beta\log(M_*/M_{\rm med}) + \mathrm{N}(0, \sigma^2). \quad (3)$$

Here α and β are the intercept and the slope of the linear function, respectively. $\mathrm{N}(0, \sigma^2)$ represents a normal distribution with σ being the intrinsic scatter in units of dex kpc^{-1}. $M_{\rm med}$ is the median of the input stellar masses taken as normalization. For the entire mass range (where $M_{\rm med} = 10^{9.4} M_\odot$), we obtain the following estimates: $\alpha = -0.020 \pm 0.007$, $\beta = -0.016 \pm 0.008$, $\sigma = 0.060 \pm 0.006$ (see the result of Case I in Table 2). This shows a weak negative correction between metallicity gradient and stellar mass for these 111 high-z star-forming galaxies.

To understand this negative mass dependence, we show two theoretical predictions from the EAGLE simulations in Fig. 9, corresponding to two suites of numerical simulations implementing different strengths of supernova feedback (Tissera et al. 2018). We see a drastic difference in the slope of the mass dependence of metallicity gradients predicted by different feedback settings in EAGLE, albeit the short M_* coverage. This difference is largely caused by the bifurcations seen in the temporal evolutions of radial chemical profiles for individual galaxies, exemplified by the two simulation tracks shown in Fig. 8. Under the assumption of weak feedback, galaxies evolve according to secular processes, and their radial gradients flatten over time (Pilkington et al. 2012). Given mass assembly down-sizing, more massive galaxies are in a later phase of disk growth than less massive ones (Brinchmann et al. 2004). Collectively, a positive mass dependence of radial gradients manifests. However, when feedback is enhanced, feedback-driven gas flows can efficiently mix stellar nucleosynthesis yields and prevent any metal inhomogeneity from emerging (Ma et al. 2017). This effect is more pronounced in lower mass galaxies living in smaller dark matter halos with shallower gravitational potentials. As a result, a generally negative mass dependence (flat/inverted gradients at low-mass end and negative gradients at high-mass end) can be anticipated.

Fig. 9 also shows the 2-σ spread of the mass dependence from the FIRE simulations (Ma et al. 2017). Given the relatively strong feedback scheme implemented in FIRE, we expect a negative mass dependence, which is indeed seen. Remarkably, the predictions of the FIRE simulations match very well the linear regression fit based on the combined high-z metallicity gradient sample. Our result is thus in better agreement with enhanced feedback — rather than secular processes — playing a significant role in shaping the chemical enrichment and structural evolution during the disk mass assembly (Hopkins et al. 2014; Vogelsberger et al. 2014).

To verify that the observed trends are robust, we subdivide the gradient measurements into three mass bins and perform

---

[8] Only 3/11 gradients reported in Leethochawalit et al. (2016) have M_* measured.

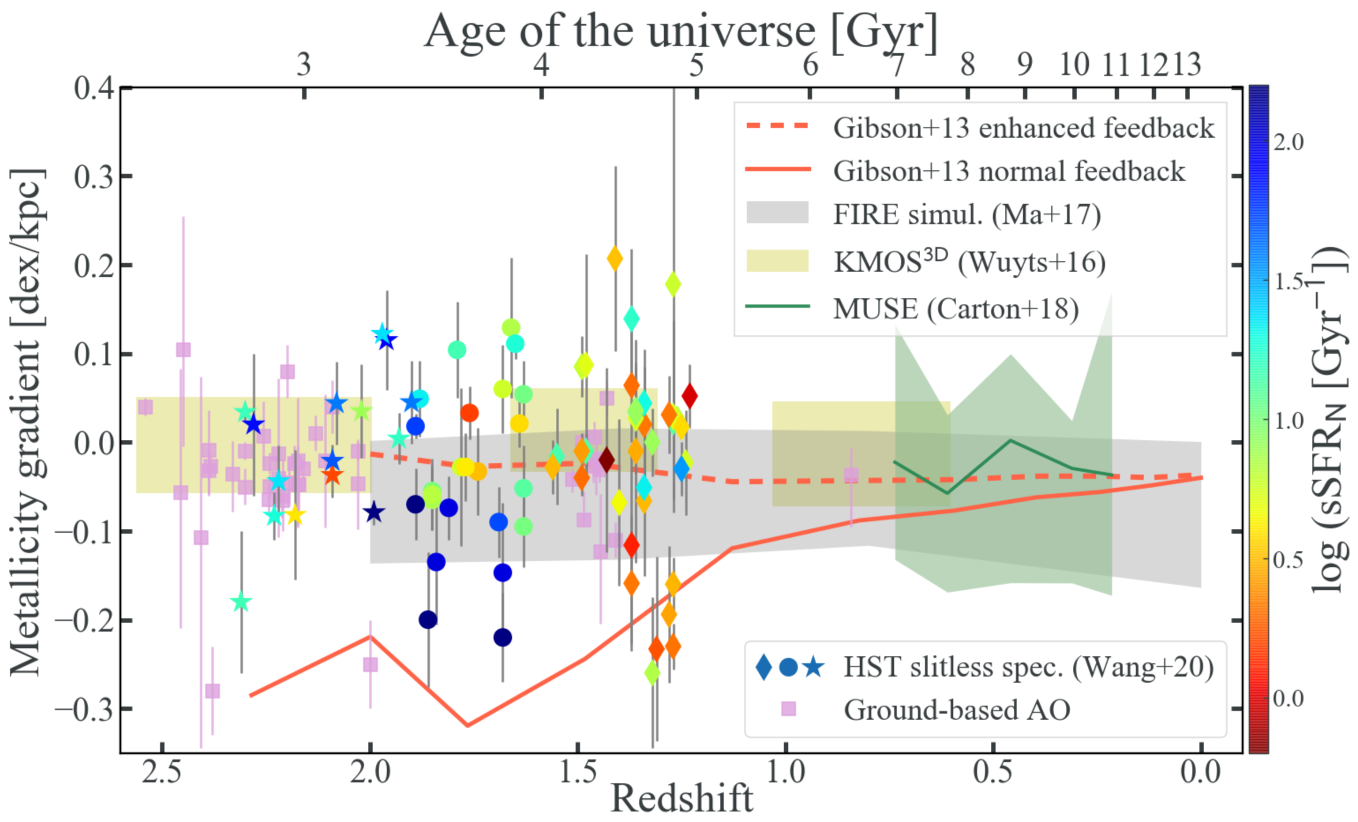

Figure 8. Overview of metallicity gradients in the distant Universe. Our measurements are represented by three symbols, corresponding to different z ranges as in Fig. 4, color-coded in sSFR. As a comparison, we also include individual measurements at similar resolution ($\lesssim$kpc scale) from ground-based AO-assisted observations, marked by magenta squares (Swinbank et al. 2012; Jones et al. 2013; Leethochawalit et al. 2016; Förster Schreiber et al. 2018). The 2-σ spreads of measurements from *KMOS*^{3D} (Wuyts et al. 2016) and *MUSE* (Carton et al. 2018), and the simulation results from FIRE (Ma et al. 2017), are shown as shaded regions in green, yellow, and grey, respectively. The evolutionary tracks of two simulated disk galaxies (Milky Way analogs at $z \sim 0$) with different feedback strength but otherwise identical numerical setup are denoted by the two orange curves.

a separate linear regression analysis to each bin. The results are given in Table 2. We see that the intercept value becomes more negative as M_* increases, with the slopes all consistent with zero, confirming the negative mass dependence of metallicity gradients over the entire mass range. More importantly, we observe an increase in the intrinsic scatter of metallicity gradients with M_* from high-mass to low-mass regimes, consistent with the findings in local spiral galaxies by Bresolin (2019). This increase in scatter can also be found if separating the galaxies based on their sSFR[9]. For galaxies in the combined sample with sSFR $\gtrsim$ 5 Gyr^{-1}, the scatter is constrained to be $\sigma = 0.082^{+0.012}_{-0.011}$ (case IVa in Table 2) whereas for galaxies with sSFR $\lesssim$ 5 Gyr^{-1}, the scatter is instead $\sigma = 0.046^{+0.007}_{-0.006}$ (case IVb in Table 2).

The increase of sSFR in low-mass systems can be ascribed to the accretion of low-metallicity gas from the cosmic filaments (i.e., cold-mode gas accretion, Dekel et al. 2009), or gravitational interaction events amplifying the star-formation efficiency (i.e., merger-induced starbursts, Stott et al. 2013). Both of them can bring about large dispersions in the radial chemical profiles. To investigate which one of the two effects is more dominant in boosting the chemo-structural diversity in low-mass high-sSFR galaxies, we turn to the global MZR of our sample, presented in Section 3.6 (see Fig. 5). We rely on the WISP measurements as the control sample, because of the similar source selection criteria, mass coverage, redshift range, and consistent techniques in estimating SFR (based on Balmer line fluxes) and metallicity (assuming the Maiolino et al. (2008) calibrations).

We find that in the medium-mass bin ($M_*/M_\odot \in [10^9, 10^{10}]$), the galaxies in our sample with higher SFR than that of the WISP stacks, are more metal-poor by 0.15 dex than the WISP metallicities in the corresponding mass range. This is supportive of the cold-mode accretion diluting the global metallicity of our galaxies, stimulating star formation and increasing the intrinsic scatter of metallicity gradients.

---

[9] Here we use the SED-derived SFR, i.e., SFR^S in Table 3, for our galaxies to be self-consistent throughout the combined sample.

However, in the low-mass bin ($M_*/M_\odot \in [10^8, 10^9]$), our galaxies with higher SFR than WISP show significant metal-enrichment, i.e., higher by 0.27 dex than the corresponding WISP metallicities. We hence argue that in the dwarf-mass regime of $M_* \lesssim 10^9 M_\odot$, merger-driven starbursts play a more predominant role than the cold-mode accretion does to boost the chemo-structural diversity. Our result is consistent with the sharp increase of the merger fraction — from 10% to over 50% for galaxies at $M_* \sim 10^{10}$ to $10^{8.5}$ at $z \sim 1.5$ — found by the HiZELS survey (Stott et al. 2013, 2014). For part of our dwarf galaxies on which we have mapped their gas kinematics using Keck OSIRIS, we also found that the velocity field becomes more turbulent (i.e. with lower ratios of rotational speed versus velocity dispersion) for galaxies with higher sSFR (Hirtenstein et al. 2018). This kinematic evidence further reinforces the scenario that mergers boost the star-formation efficiency, random motions, and the chemo-structural diversity in dwarf galaxies at cosmic noon.

Lastly, the combined high-z metallicity gradient sample reveals that inverted gradients are almost exclusively found in the low-mass range, i.e., $M_* \lesssim 3 \times 10^9$ (also see Carton et al. 2018). This feature is also seen in the local Universe: only the lowest M_* bin (at $\sim 10^9 M_\odot$) from the MaNGA survey shows positive gradient slope (Belfiore et al. 2017). The reason for inverted gradients in isolated systems is still under debate, with possible causes ranging from centrally-directed cold-mode accretion (Cresci et al. 2010), or metal-loaded outflows triggered by galactic winds (Wang et al. 2019). In any case, these processes should be more pronounced in low-mass systems, suggested by the occurrence rate of this inverted gradient phenomenon.

6. CONCLUSION

To summarize, we have presented an unprecedentedly large sample of sub-kpc resolution metallicity radial gradients in 76 gravitationally-lensed star-forming galaxies at $1.2 \lesssim z \lesssim 2.3$, using *HST* near-infrared slitless spectroscopy. We performed state-of-the-art reduction of grism data, careful stellar continuum SED fitting after subtracting nebular emission from broad-band photometry, and Bayesian inferences of metallicity and SFR based on emission line fluxes. Our sample spans a M_* range of [10^7, 10^{10}] $M_\odot$, an instantaneous SFR range of [1, 100] $M_\odot$/yr, and a global metallicity range of $7.6 \lesssim 12 + \log(\mathrm{O/H}) \lesssim 9.0$, i.e., $[\frac{1}{12}, 2]$ solar. At 2-σ confidence level, we secured 15 and 7 galaxies that show negative and inverted gradients, respectively. Collecting all high resolution gradient measurements at high redshifts currently existing (where results presented in this work constitute 2/3 of all measurements), we measure a weak negative mass dependence over four orders of magnitude in M_*: $\Delta\log(\mathrm{O/H})/\Delta r$ [dex kpc^{-1}] $= (-0.020 \pm 0.007) + (-0.016 \pm 0.008) \log(M_*/10^{9.4} M_\odot)$ with $\sigma = 0.060 \pm 0.006$ being the intrinsic scatter. This supports enhanced feedback as the main driver of the chemo-structural evolution of star-forming galaxies at cosmic noon. Moreover, we also find that the intrinsic scatter of metallicity gradients increases with decreasing M_* and increasing sSFR. Combined with the global metallicity measurements, our result is consistent with the hypothesis that the combined effect of cold-mode gas accretion and merger-induced starbursts strongly boosts the chemo-structural diversity of low-mass star-forming galaxies at cosmic noon, with mergers playing a much more predominant role in the dwarf-mass regime of $M_* \lesssim 10^9 M_\odot$. This work demonstrates that by accurately mapping the radial chemical profiles of star-forming galaxies at high redshifts, we can cast strong constraints on the role that feedback, gas flows and mergers play in the early phase of disk mass assembly. The observed trends between metallicity and galaxy properties, while weak, are nonetheless very well measured over a wide dynamic range of mass. This census offers a stringent test for theoretical models and cosmological simulations, as the resulting trends are highly sensitive to baryon cycling processes at the peak of cosmic star formation ($1.2 \lesssim z \lesssim 2.3$). Using the Near-Infrared Imager and Slitless Spectrograph (NIRISS) onboard the soon-to-be-launched James Webb Space Telescope (*JWST*), the GLASS-*JWST* ERS program (PI Treu, ID 1324) and the CAnadian NIRISS Unbiased Cluster Survey (CANUCS) GTO program (PI Willott) will conduct K-band slitless spectroscopy on several galaxy cluster center fields. The data acquired by these programs will enable sub-kpc resolution measurements of metallicity gradients to $z \lesssim 3.5$, and thus extend the test for theoretical predictions to even higher redshifts.

ACKNOWLEDGMENTS

We thank the anonymous referee for careful reading and constructive comments that improve the quality of our paper. This work is supported by NASA through HST grant HST-GO-13459. XW acknowledges support by UCLA through a dissertation year fellowship. XW is greatly indebted to his family, i.e., Dr. Xiaolei Meng, SX Wang and ST Wang, for their tremendous love, care and support during the COVID-19 pandemic, without which this work could not have been completed.

Software: APLpy (Robitaille & Bressert 2012), AstroDrizzle (Gonzaga 2012), Astropy (Price-Whelan et al. 2018), Emcee (Foreman-Mackey et al. 2013), FAST (Kriek et al. 2009), Grizli (G. Brammer et al. in prep), SExtractor (Bertin & Arnouts 1996), VorBin (Cappellari & Copin 2003).

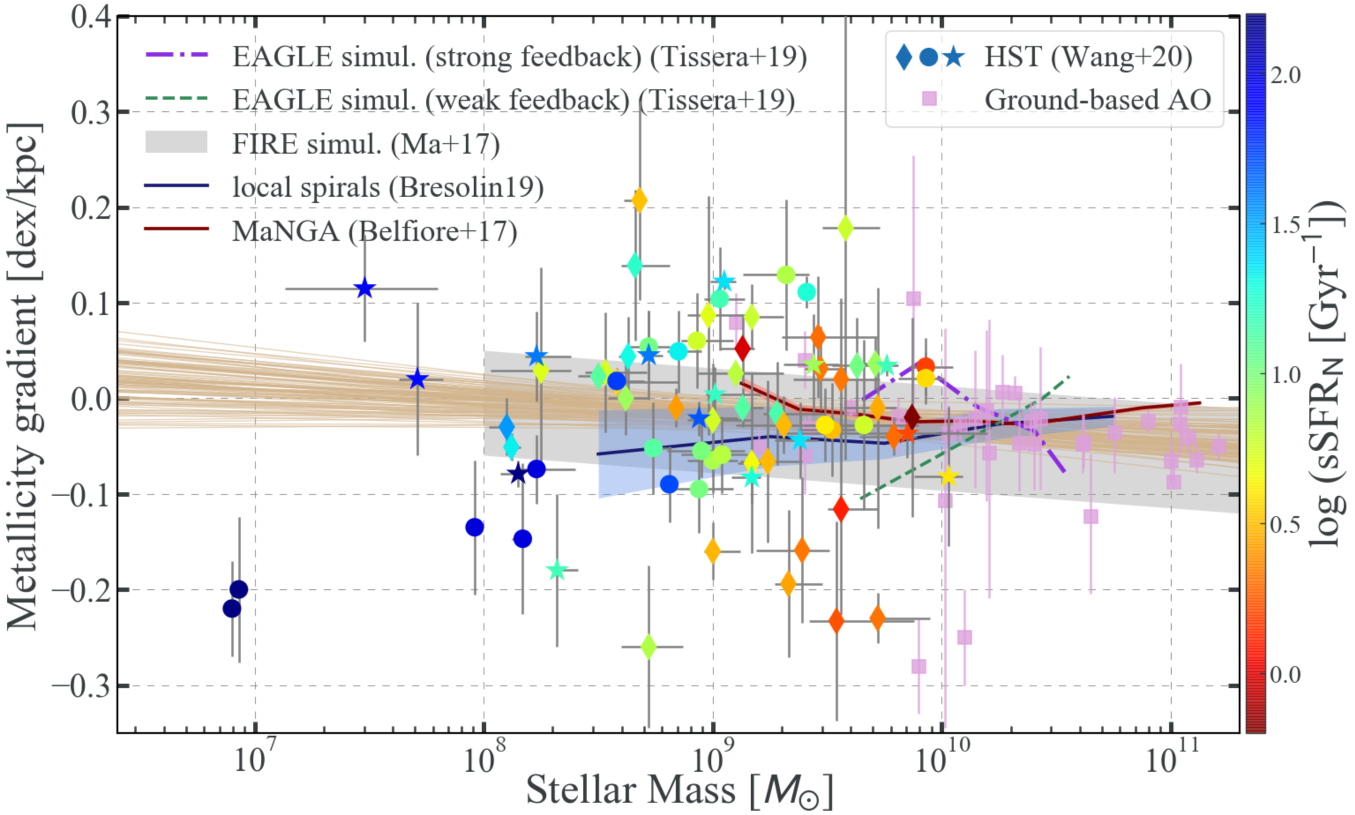

Figure 9. Metallicity gradient as a function of stellar mass for high-z and local star-forming galaxies. As in Fig. 8, our measurements are represented by three types of symbols regarding three z bins colored coded in sSFR, whereas high-z ground-based measurements with similar resolution are denoted by magenta squares. For comparison, we also show the median measurements with 1-σ interval of local measurements (Belfiore et al. 2017; Bresolin 2019), the 2-σ spread of the FIRE simulations (Ma et al. 2017), and two mass dependencies derived from the EAGLE simulations assuming different feedback settings (Tissera et al. 2018). Combining all available high-z gradients measured at sufficient spatial resolution ($\lesssim$kpc), we obtain a weakly negative mass dependence over four orders of magnitude in M_*: $\Delta\log(\mathrm{O/H})/\Delta r$ [dex kpc^{-1}] = $(-0.020 \pm 0.007) + (-0.014 \pm 0.008)\log(M_*/10^{9.4}M_\odot)$ with the intrinsic scatter being $\sigma = 0.060 \pm 0.006$. The thin lines in tan mark 100 random draws from the linear regression. This observed mass dependence is in remarkable agreement with the predictions of the FIRE simulations. However, as shown in Table 2, we also observe an increase of the intrinsic scatter from high-mass to low-mass systems, not captured by theoretical predictions.

APPENDIX

A. MEASURING METALLICITY RADIAL GRADIENTS USING VORONOI TESSELLATION IN THE SOURCE PLANE

As explained in Section 3.6, we use Voronoi tessellation to divide the spatial extent of our sample galaxies into sub-regions, where we measure metallicities individually to estimate their radial gradients. This tessellation process is by default performed in the image plane, since the noise properties of the observed emission line fluxes are well defined in the image plane. Furthermore, the majority of our sample galaxies have magnifications less than 4 and the sample median value is $\mu = 2.69$ (see the results presented in Table 3), which indicates that the highly anisotropic lensing phenomenon is relatively rare in our sample.

Nevertheless, there indeed exist some galaxies in our sample that are highly anisotropically magnified. It is thus important to verify that the highly anisotropic lensing effect does not introduce significant systematic offset into their radial gradients measured in the image plane. For that purpose, we measure their radial gradients in the source plane, using similar methods outlined in Section 3.6. Figure 10 shows such analysis of one exemplary source in our sample, i.e., MACS0717-ID01131 at $z = 1.85$ with $\mu = 5.88$. The image-plane morphology, shown in Figure 40, indicates that one of the two spatial directions is preferentially magnified. Here, unlike the procedures given in Figure 40, we first transform the observed 2D emission line maps of this galaxy into its source plane, by ray-tracing each pixel to their source-plane positions according to the lensing deflection fields given

Table 2. Linear regression results of the mass dependence of metallicity radial gradients at cosmic noon

Case	α	β	σ	$M_{\rm med}[M_\odot]$	$N_{\rm source}$	Notes
I	$-0.0203^{+0.0070}_{-0.0068}$	$-0.0156^{+0.0076}_{-0.0077}$	$0.0601^{+0.0065}_{-0.0057}$	$10^{9.4}$	111	all metallicity gradients measured at sub-kpc resolution
II	$-0.0128^{+0.0099}_{-0.0097}$	$-0.0025^{+0.0181}_{-0.0181}$	$0.0677^{+0.0091}_{-0.0077}$	$10^{9.0}$	76	all metallicity gradients from *HST* spectroscopy
IIIa	$-0.0430^{+0.0078}_{-0.0085}$	$-0.0009^{+0.0186}_{-0.0179}$	$0.0342^{+0.0075}_{-0.0060}$	$10^{10.4}$	27	high-mass bin: $M_*/M_\odot \gtrsim 10^{10}$
IIIb	$-0.0082^{+0.0134}_{-0.0137}$	$-0.0520^{+0.0565}_{-0.0552}$	$0.0785^{+0.0122}_{-0.0104}$	$10^{9.5}$	47	medium-mass bin: $10^9 \lesssim M_*/M_\odot \lesssim 10^{10}$
IIIc	$-0.0198^{+0.0140}_{-0.0139}$	$0.0270^{+0.0524}_{-0.0512}$	$0.0607^{+0.0154}_{-0.0125}$	$10^{8.6}$	31	low-mass bin: $10^8 \lesssim M_*/M_\odot \lesssim 10^9$
IVa	$-0.0129^{+0.0128}_{-0.0132}$	$0.0207^{+0.0164}_{-0.0166}$	$0.0823^{+0.0125}_{-0.0108}$	$10^{8.9}$	50	high-sSFR bin: sSFR $\gtrsim 5{\rm Gyr}^{-1}$
IVb	$-0.0344^{+0.0078}_{-0.0080}$	$-0.0074^{+0.0094}_{-0.0094}$	$0.0464^{+0.0074}_{-0.0062}$	$10^{9.7}$	61	low-sSFR bin: sSFR $\lesssim 5{\rm Gyr}^{-1}$

NOTE—The linear regression is performed using the LINMIX software[a] taking into account the measurement uncertainties on both stellar mass (M_*) and metallicity gradient ($\Delta\log({\rm O/H})/\Delta r$), following the Bayeisan method proposed by Kelly (2007). The following function form (Eq. 3) is adopted: $\Delta\log({\rm O/H})/\Delta r$ [dex kpc^{-1}] $= \alpha + \beta\log(M_*/M_{\rm med}) + {\rm N}(0, \sigma^2)$. As given in the rightmost column, Cases I corresponds to the linear regression result based on all sub-kpc scale metallicity gradient measurements at the cosmic noon epoch, whereas Case II shows the result from our gradient measurements only. We divide the entire sample into three M_* bins and conduct linear regressions separately, with results represented by Cases IIIa,b,c. Cases IVa,b show the results if the entire sample is divided based on sSFR, instead of M_*. The number of sources ($N_{\rm source}$) involved in each case is shown in the second rightmost column.

[a] https://github.com/jmeyers314/linmix

by the adopted macroscopic lens model. Then the weighted Voronoi tessellation technique (Cappellari & Copin 2003; Diehl & Statler 2006) is again adopted to divide the source-plane surface into spatial bins with a constant SNR of 5 on [O III], the same as used in the gradient measurement in the image plane. Our forward-modeling Bayesian method of metallicity inference is conducted in each individual source-plane Voronoi bin to yield metallicity maps in the source plane.

For the galacto-centric distance scale of each individual source-plane Voronoi bin, we again rely on the 2D elliptical Gaussian function fit to the source-plane stellar mass surface density map of this galaxy[10] (see the second to the left panel in Figure 10). This fitting procedure yields the best-fit inclination, axis ratio, and major axis orientation of the galaxy, so that we not only take out the effect of lensing distortion, but also take into account the projection effect when determining the source intrinsic morphology. At last, the radial gradient can be given by a linear regression to the metallicity estimates in all source-plane Voronoi bins.

For our exemplary differentially magnified source MACS0717-ID01131, the metallicity gradient measured in its source plane is $\Delta\log({\rm O/H})/\Delta r = -0.031 \pm 0.023$ [dex kpc^{-1}], in agreement at 1-σ confidence level with the gradient measured in the image plane, i.e., $\Delta\log({\rm O/H})/\Delta r = -0.055 \pm 0.028$ [dex kpc^{-1}] (shown in Figure 40 and given in Table 3). We verified that this difference ($\lesssim$0.03 dex kpc^{-1}, compatible within 1-σ) is typical for the few highly anisotropically magnified galaxies in our sample. In fact, the metallicity radial gradient measurement in this galaxy has been presented in our previous work (Jones et al. 2015). Using half of the grism data (2 orbits of G141 and 5 orbits of G102) available at that time, Jones et al. (2015) estimated the radial metallicity gradient of this galaxy to be -0.03 ± 0.03 dex kpc^{-1} from metallicities measured in individual spatial pixels, and -0.05 ± 0.05 dex kpc^{-1} from metallicities derived in radial annuli. We see that our updated results derived in both the image and source planes presented in this work are compatible with previous measurements within measurement uncertainties.

B. A SUMMARY OF THE DATA PRODUCTS AND ANALYSIS RESULTS FOR THE FULL METALLICITY GRADIENT SAMPLE PRESENTED IN THIS PAPER (ONLINE MATERIAL)

In Figures 11 through 75, we present the source 1D/2D grism spectra, color-composite image, stellar surface density stamp, and EL maps, as well as metallicity map and radial metallicity gradient measurements for the entire sample. Following the conventions adopted in Figs. 2 and 7, we first show the 1D and 2D G102-G141 spectra, at two separate P.A.s. Note that due to grism defect and/or falling outside WFC3 FoV, some sources (i.e. A2744-ID00144, A2744-ID01897, RXJ1347-ID00664) only have coverage from one of the orients. Beneath the spectra, we show the source 2D stamps. For sources at $z \lesssim 1.6$, we display

---

[10] Note that this fitting is always performed for metallicity gradient measurements in the image plane, such that the black contours shown in all image-plane 2D maps for our sample galaxies are obtained by re-lensing the corresponding best-fit source-plane de-projected galacto-centric radius contours.

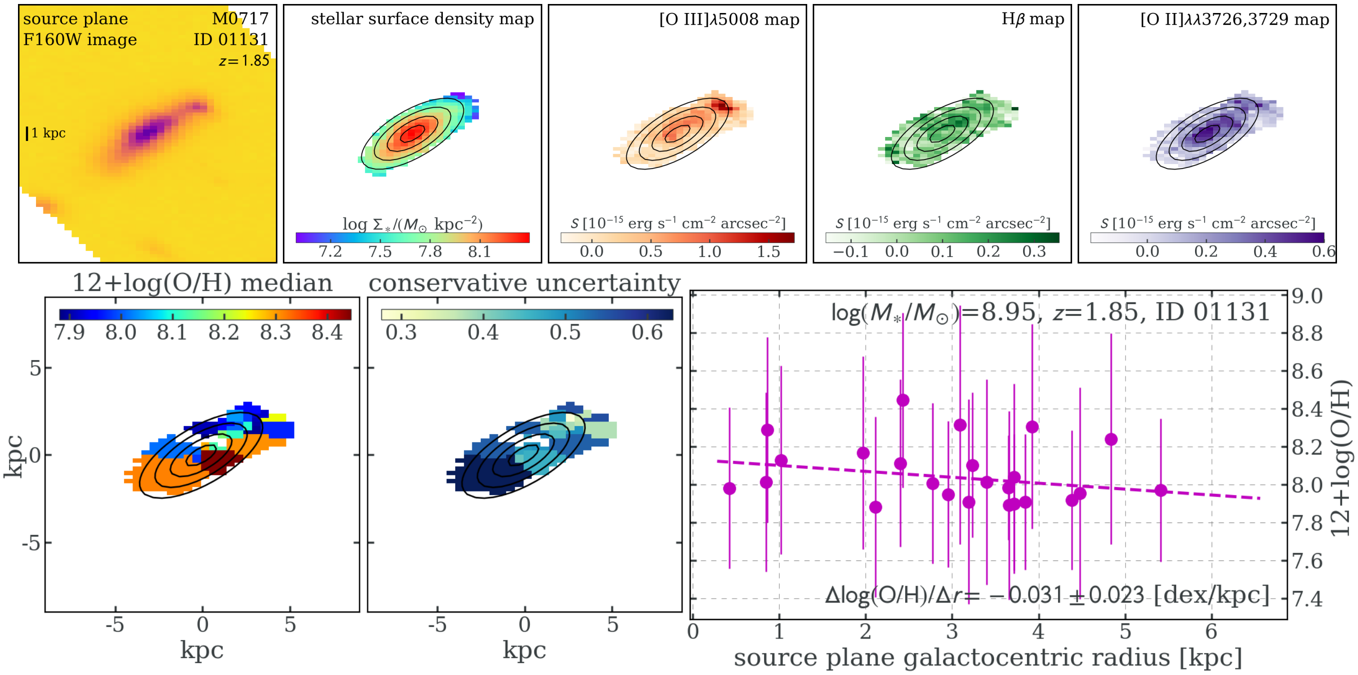

Figure 10. Source-plane metallicity radial gradient measurement of one highly anisotropically magnified galaxy (MACS0717-ID01131) in our sample. Its image-plane metallicity radial gradient measurement is presented in Figure 40. **Top**, from left to right: the source-plane reconstructed 2D maps of H_{160}-band surface brightness, stellar surface density (Σ_*), and surface brightness of emission line [O III], Hβ, and [O II]. These 2D maps are arranged on the same spatial scale with a scale bar of 1 kpc shown in the leftmost panel. The black contours mark the de-projected galacto-centric radii with 1 kpc interval, with galaxy inclination taken into account. Note that the black radius contours in Figure 40 are obtained from re-lensing the contours shown in this figure to the image plane of this galaxy. **Bottom**: metallicity map and radial gradient determination for this galaxy in its source plane. We again use Voronoi tessellation to divide its source-plane reconstructed spatial extent into bins with a constant SNR of 5 on [O III], the same as used in the gradient measurement in the image plane. In the right panel, the metallicity measurements in these source-plane Voronoi bins are plotted as magenta points. The dashed magenta line denotes the linear regression, with the corresponding slope shown at the bottom. The metallicity gradient measured in the source plane is $\Delta \log(\mathrm{O/H})/\Delta r = -0.031 \pm 0.023$ [dex kpc^{-1}], in agreement with the gradient measured in the image plane, i.e., $\Delta \log(\mathrm{O/H})/\Delta r = -0.055 \pm 0.028$ [dex kpc^{-1}].

their Hα map, whereas for sources at higher redshifts, Hγ map is shown instead, since Hα has already redshifted out of the wavelength coverage of *HST* grisms. The bottom panels show the metallicity map and radial gradient measurements.

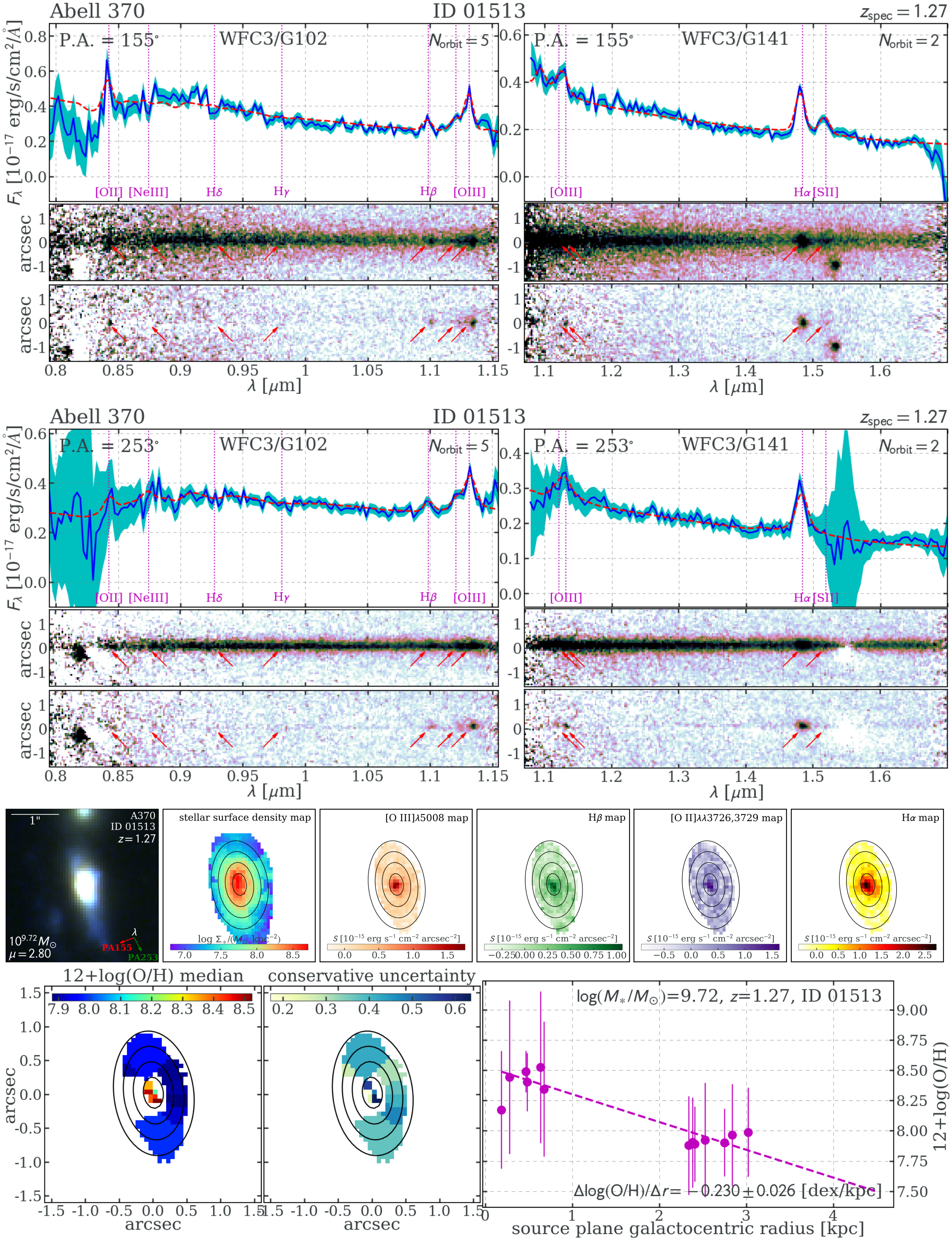

Figure 11. The source ID01513 in the field of Abell 370 is shown.

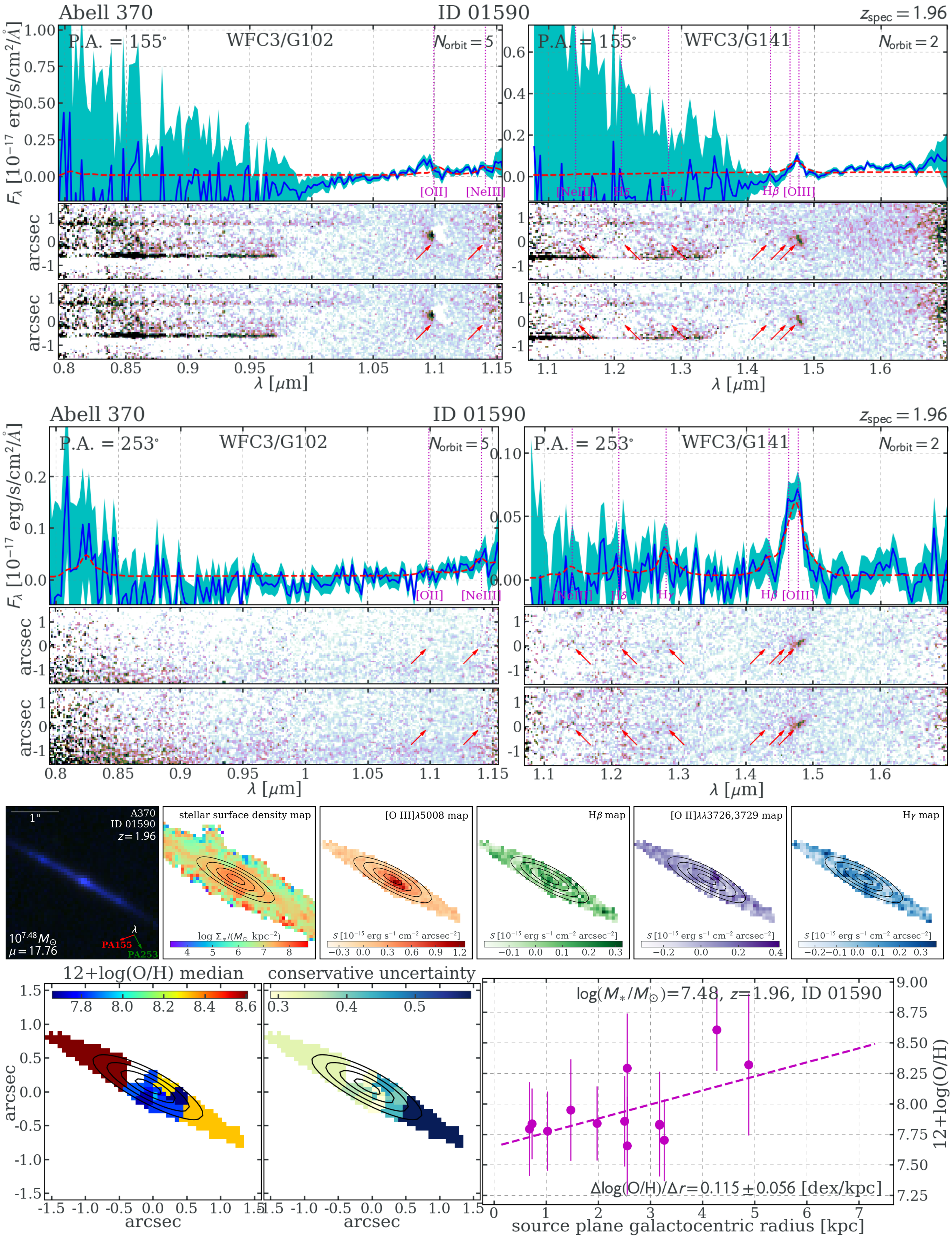

Figure 12. The source ID01590 in the field of Abell 370 is shown.

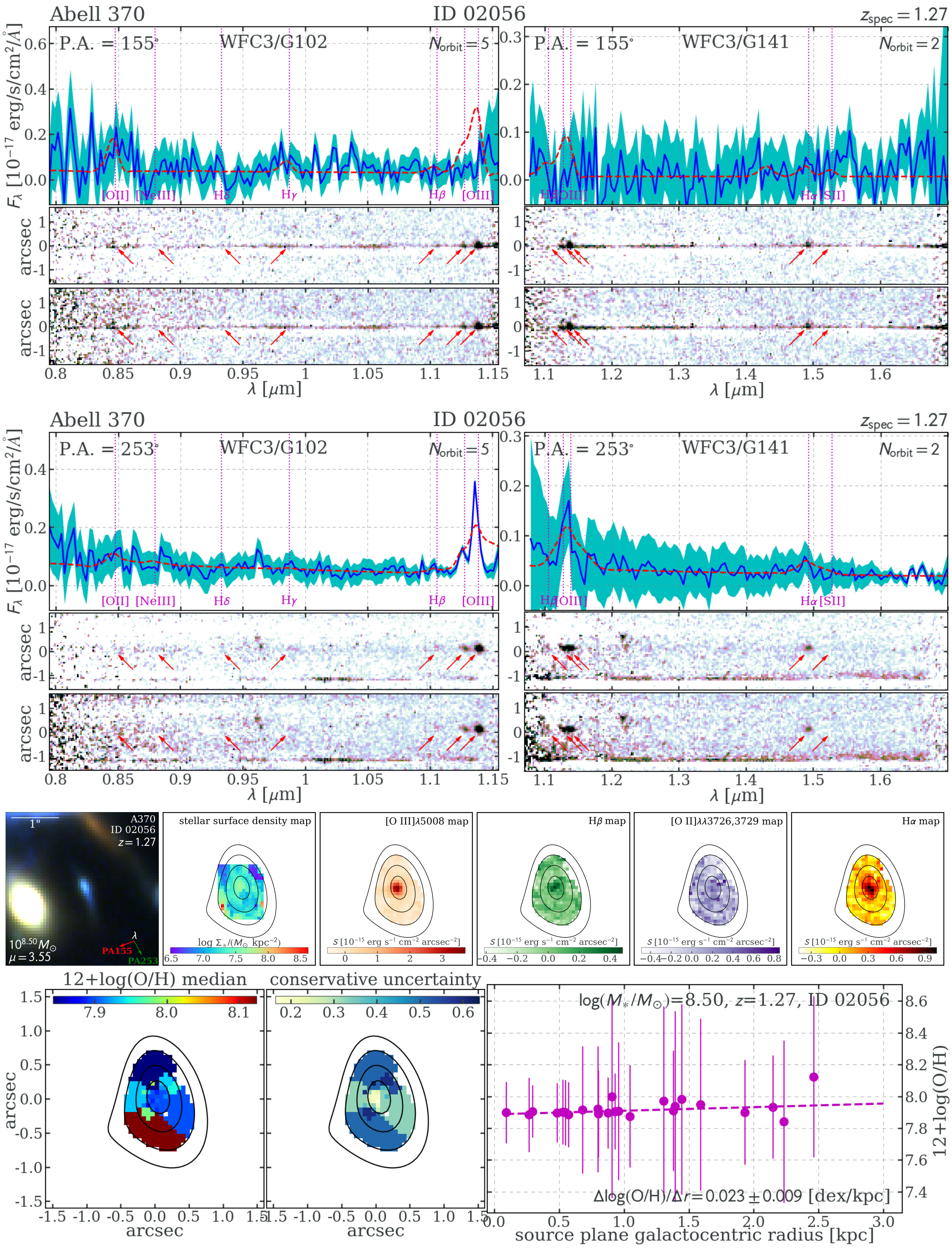

Figure 13. The source ID02056 in the field of Abell 370 is shown.

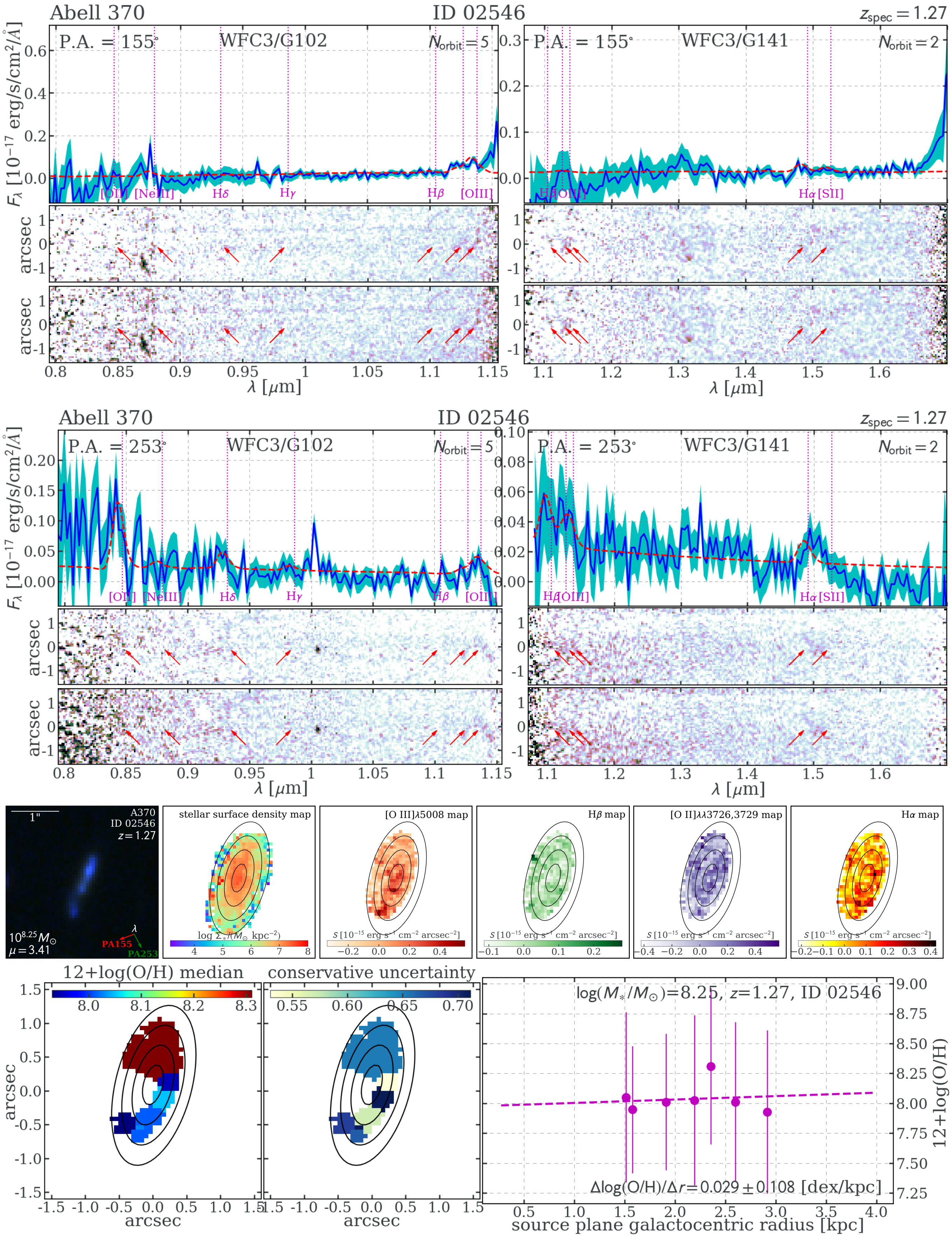

Figure 14. The source ID02546 in the field of Abell 370 is shown.

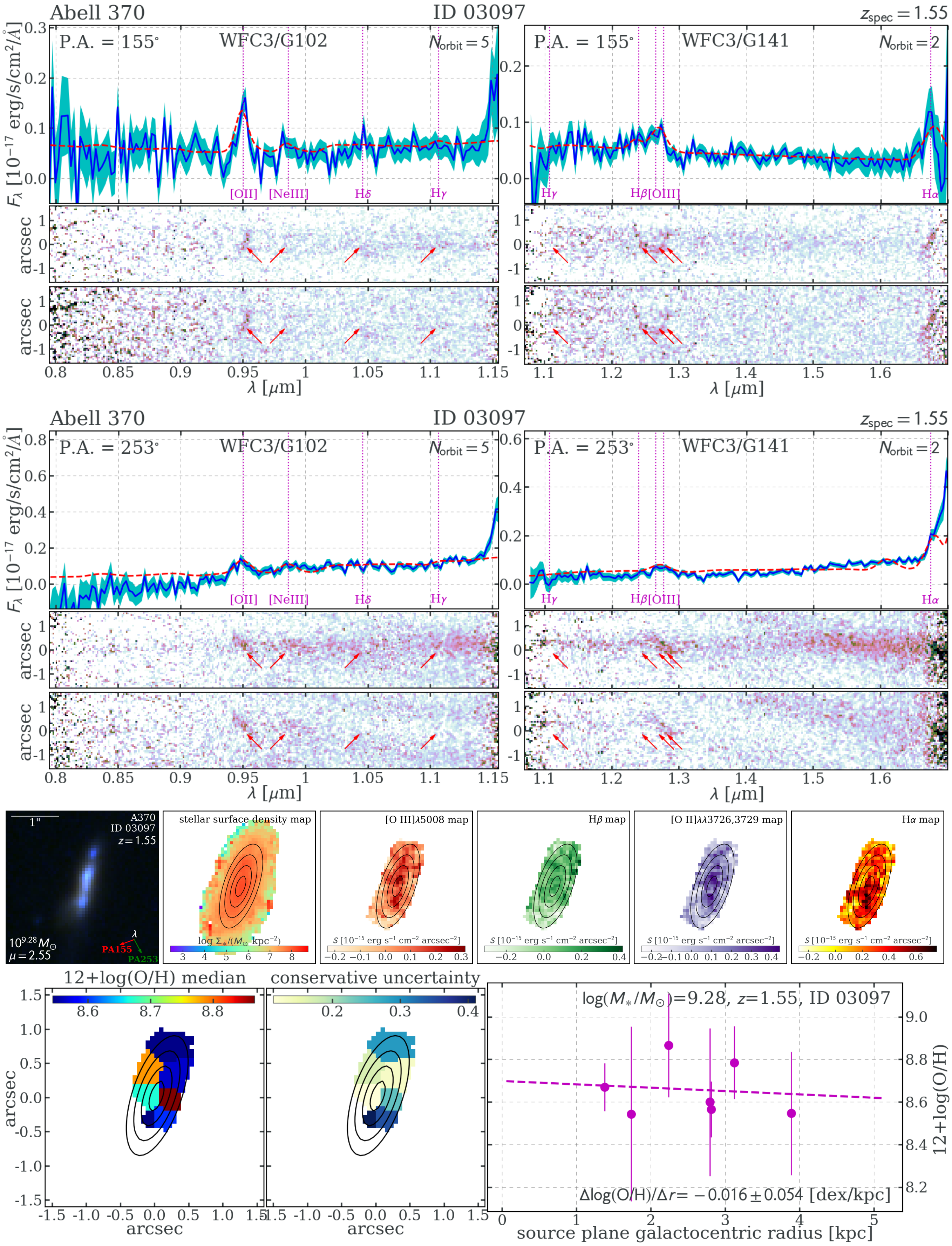

Figure 15. The source ID03097 in the field of Abell 370 is shown.

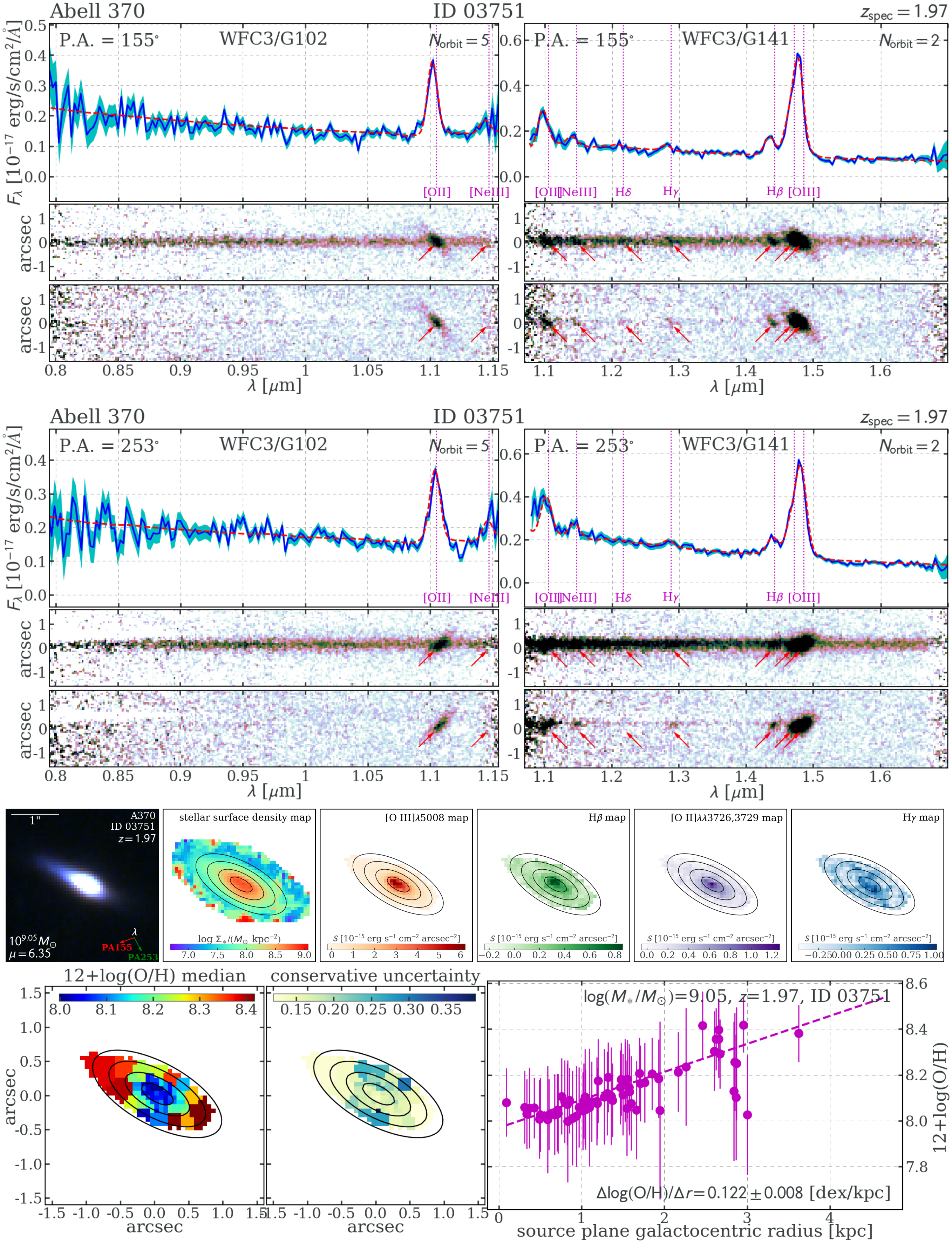

Figure 16. The source ID03751 in the field of Abell 370 is shown.

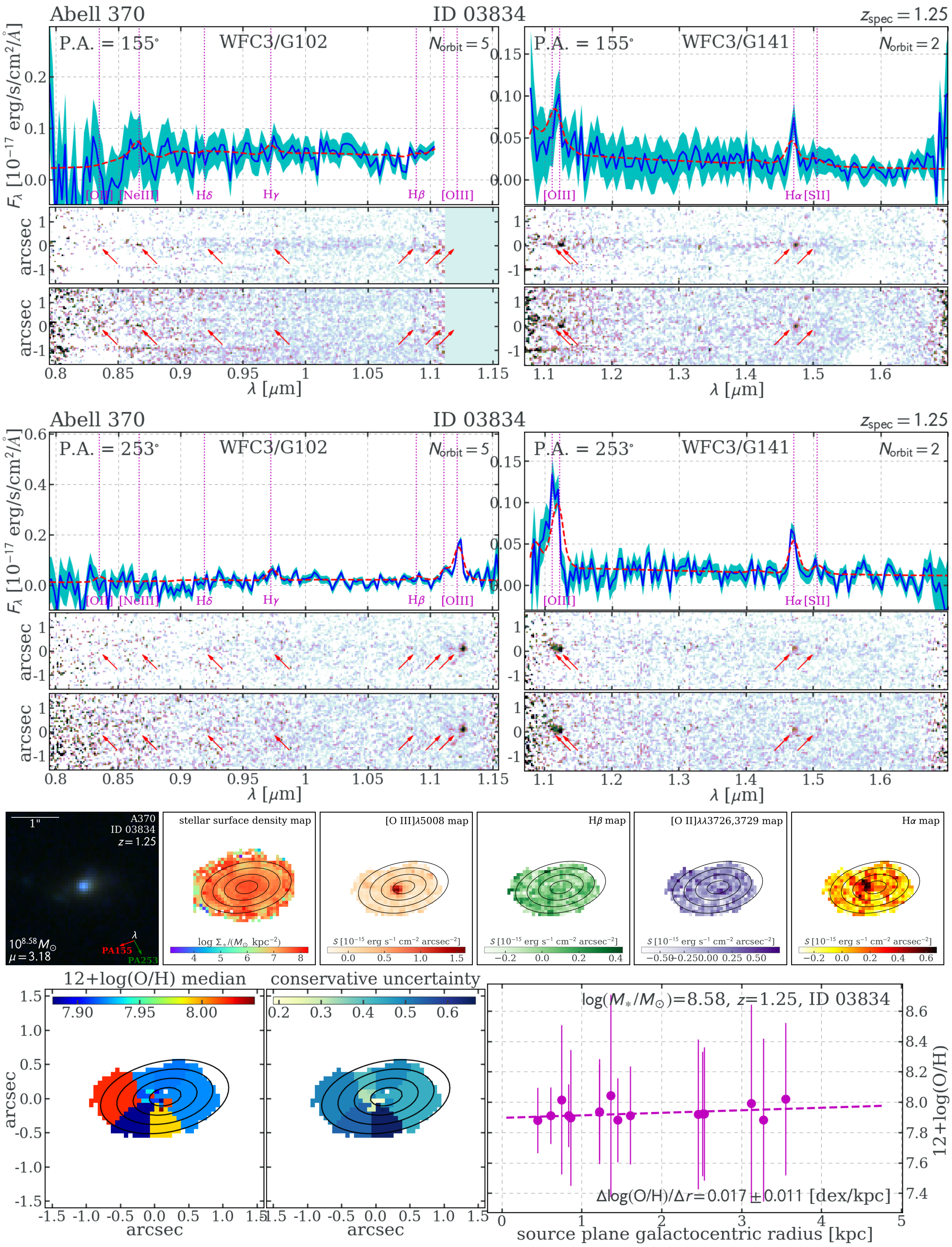

Figure 17. The source ID03834 in the field of Abell 370 is shown.

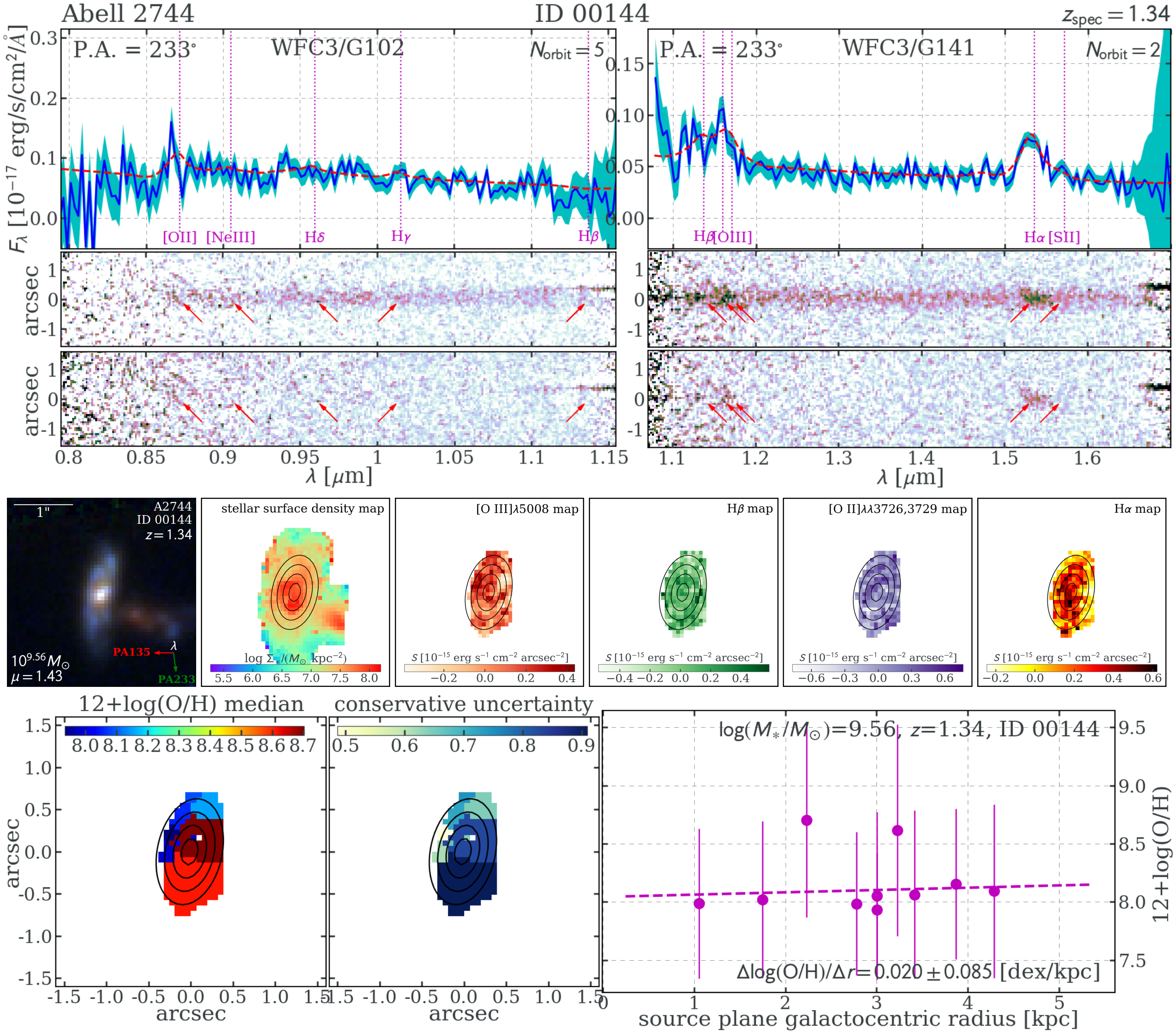

Figure 18. The source ID00144 in the field of Abell 2744 is shown.

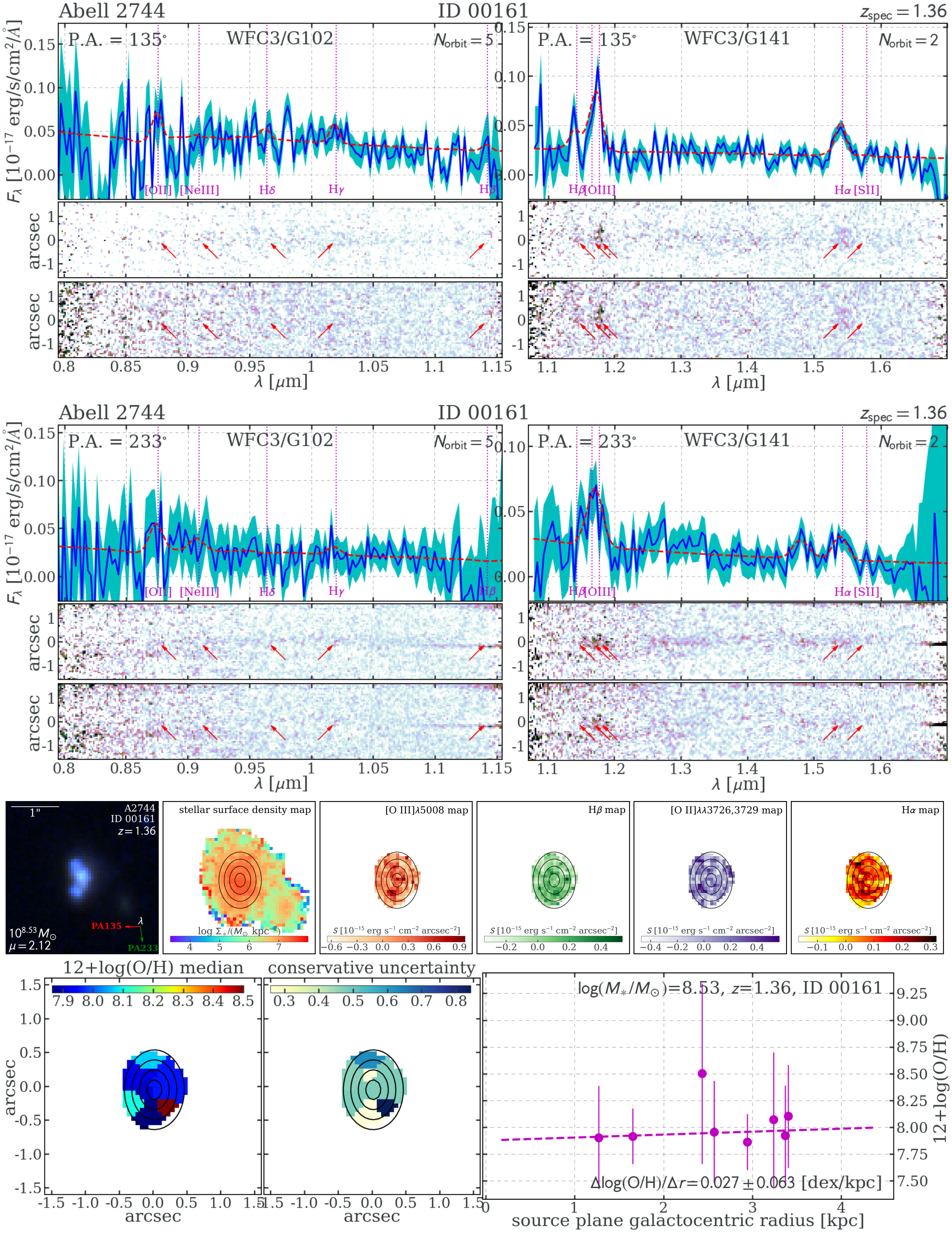

Figure 19. The source ID00161 in the field of Abell 2744 is shown.

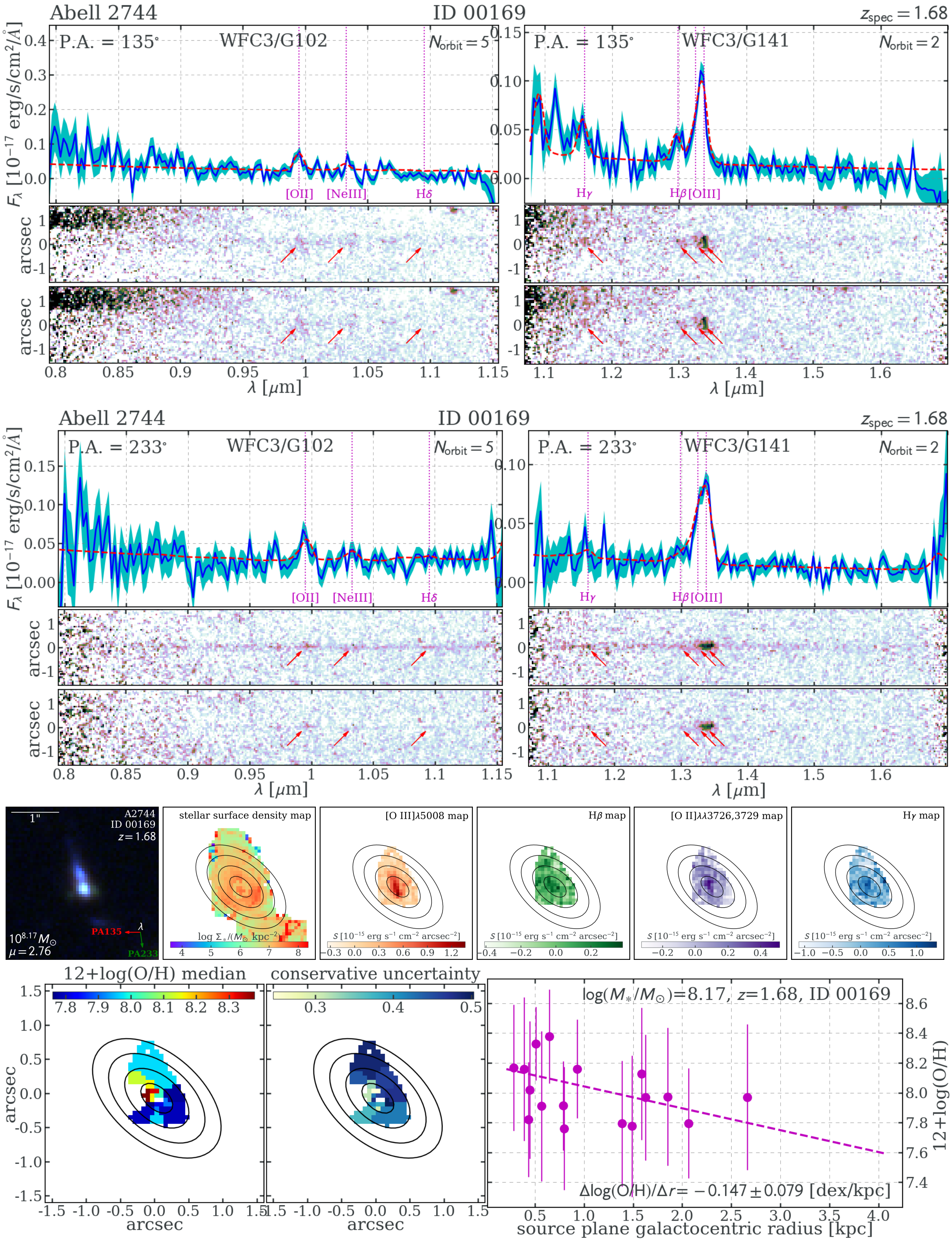

Figure 20. The source ID00169 in the field of Abell 2744 is shown.

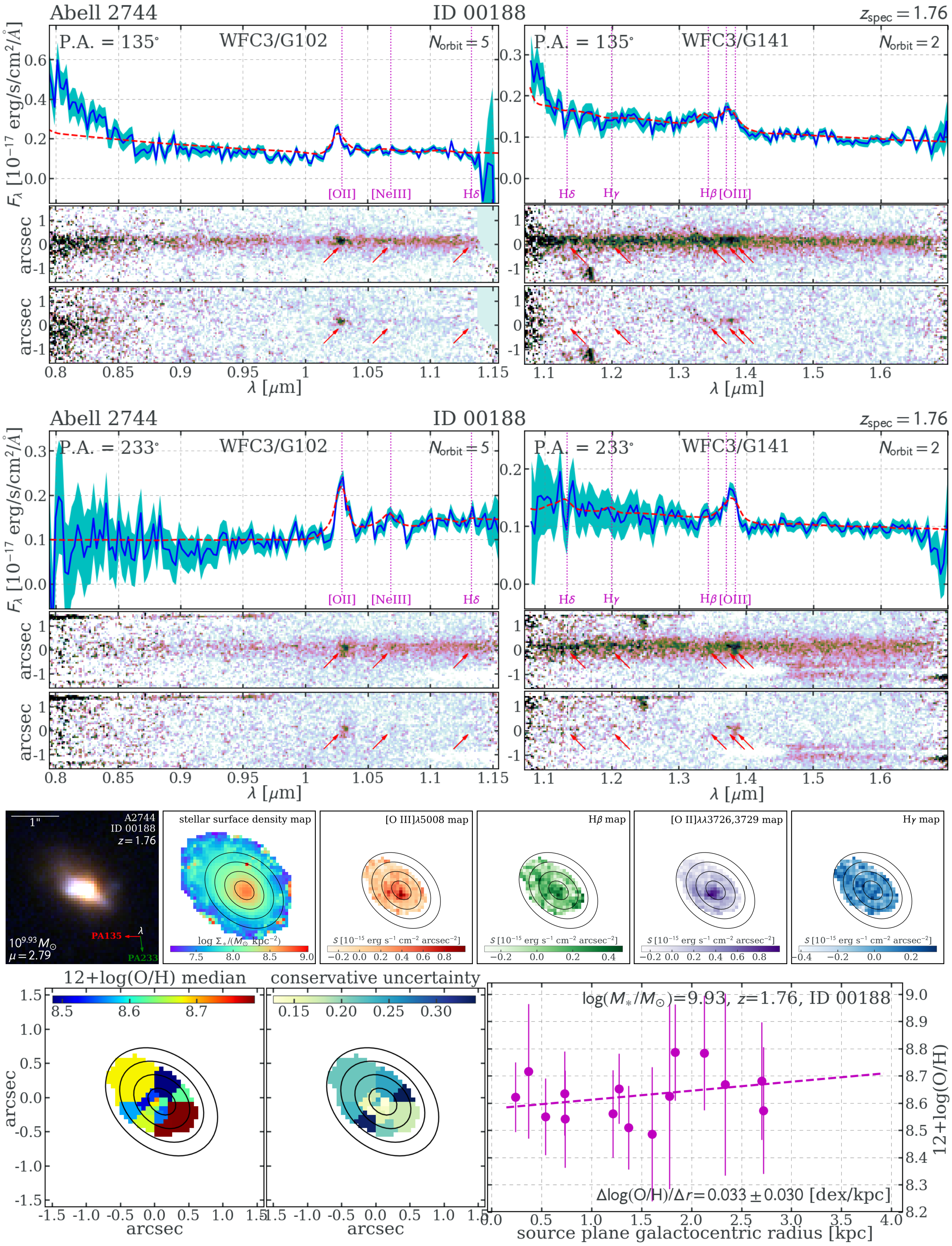

Figure 21. The source ID00188 in the field of Abell 2744 is shown.

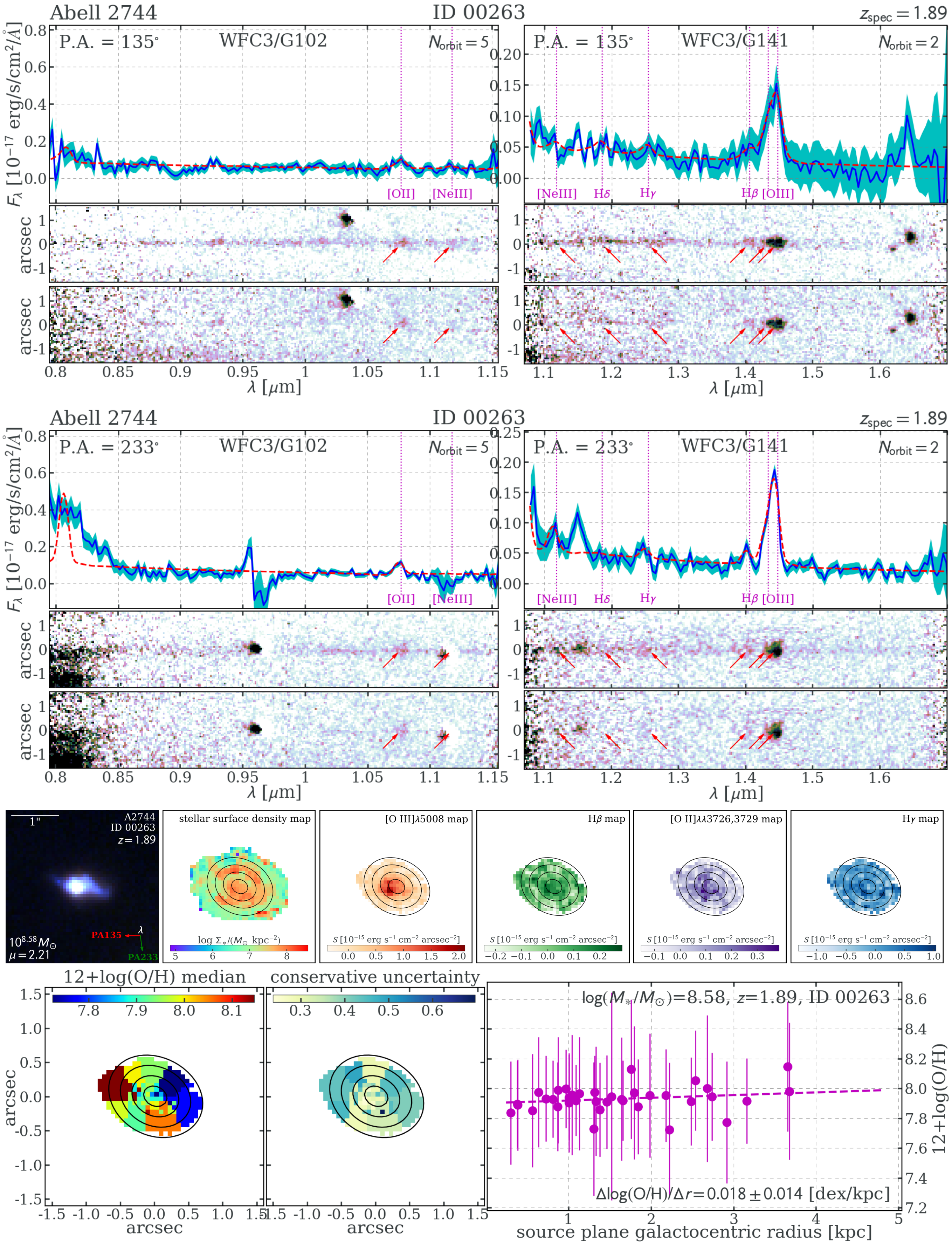

Figure 22. The source ID00263 in the field of Abell 2744 is shown.

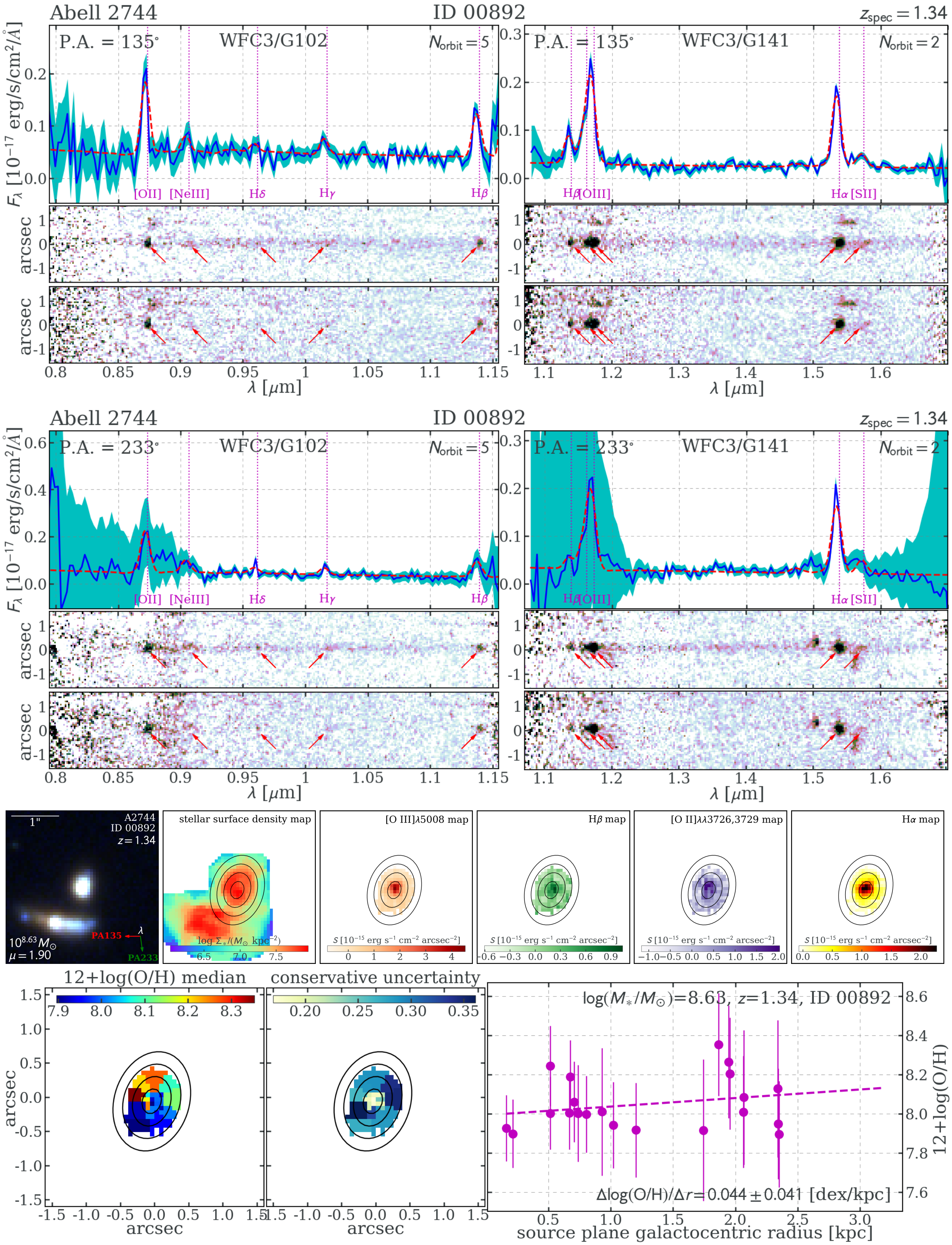

Figure 23. The source ID00892 in the field of Abell 2744 is shown.

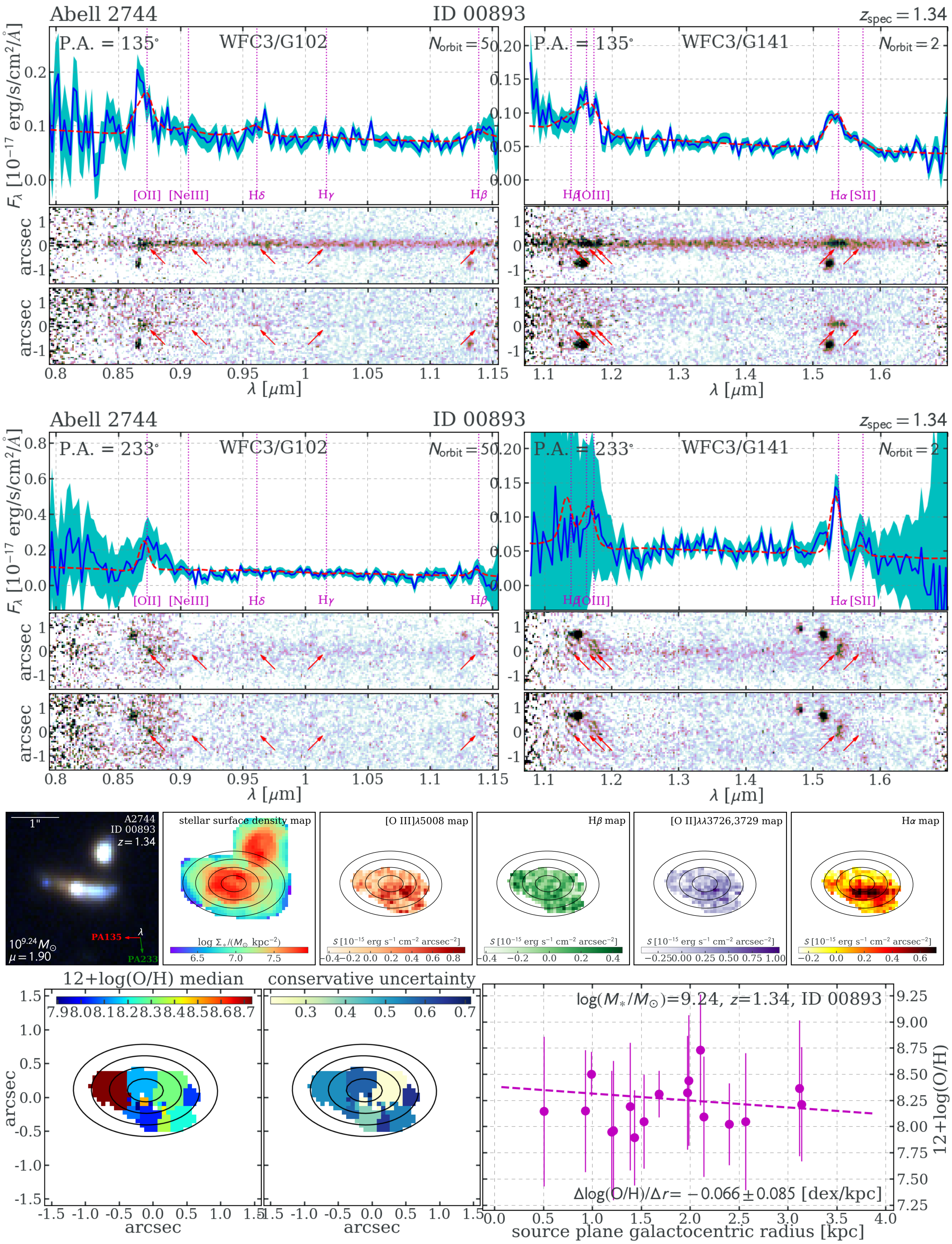

Figure 24. The source ID00893 in the field of Abell 2744 is shown.

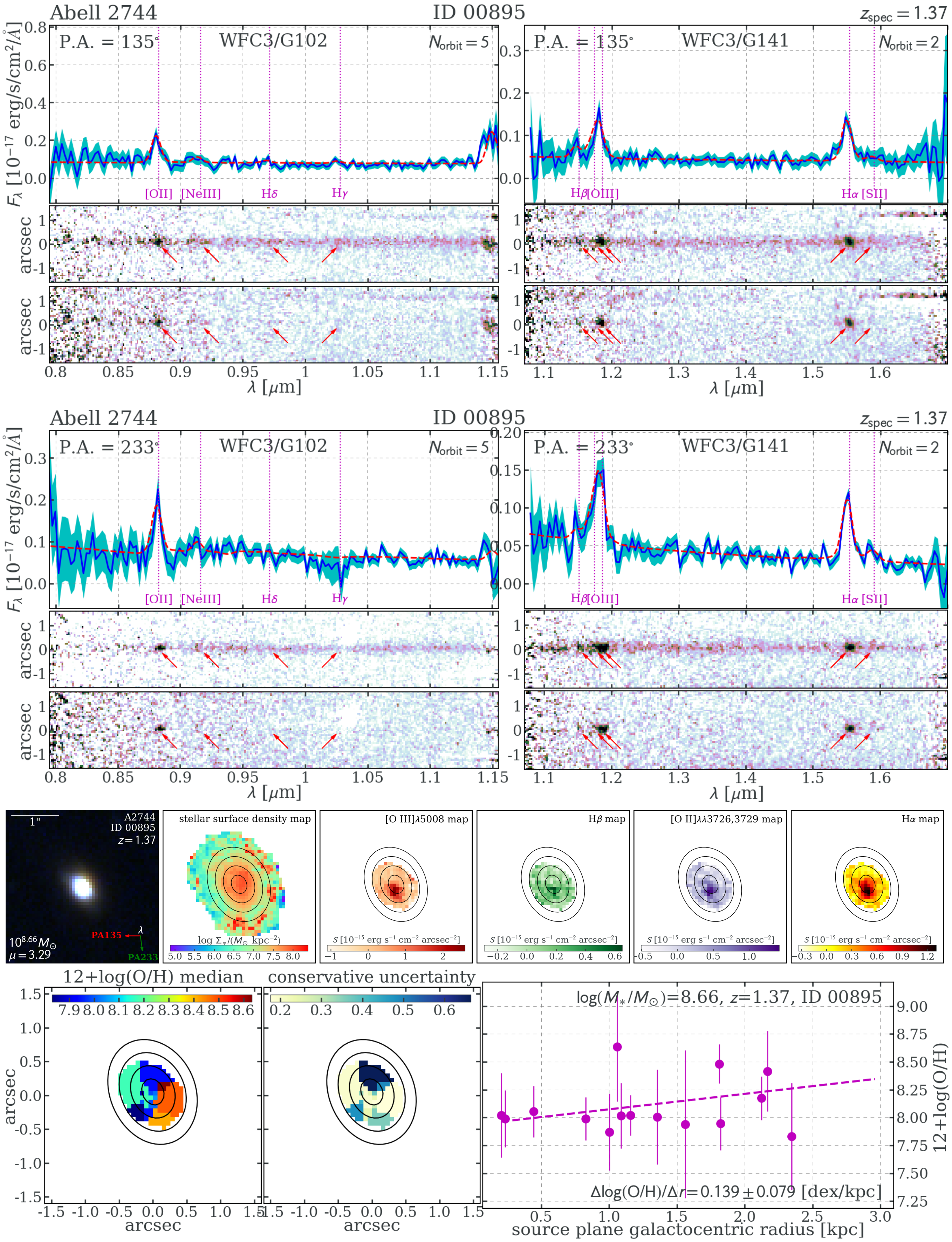

Figure 25. The source ID00895 in the field of Abell 2744 is shown.

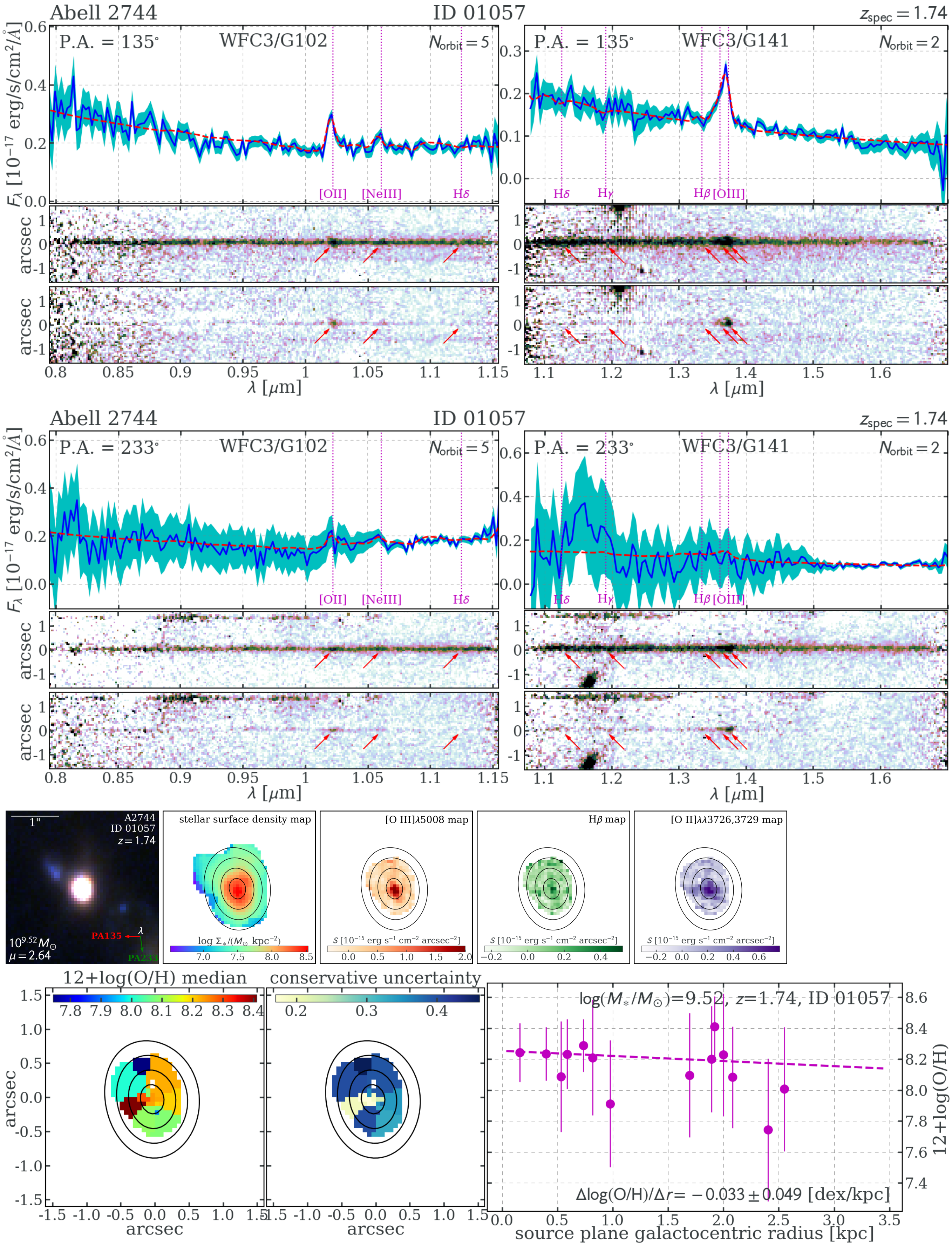

Figure 26. The source ID01057 in the field of Abell 2744 is shown.

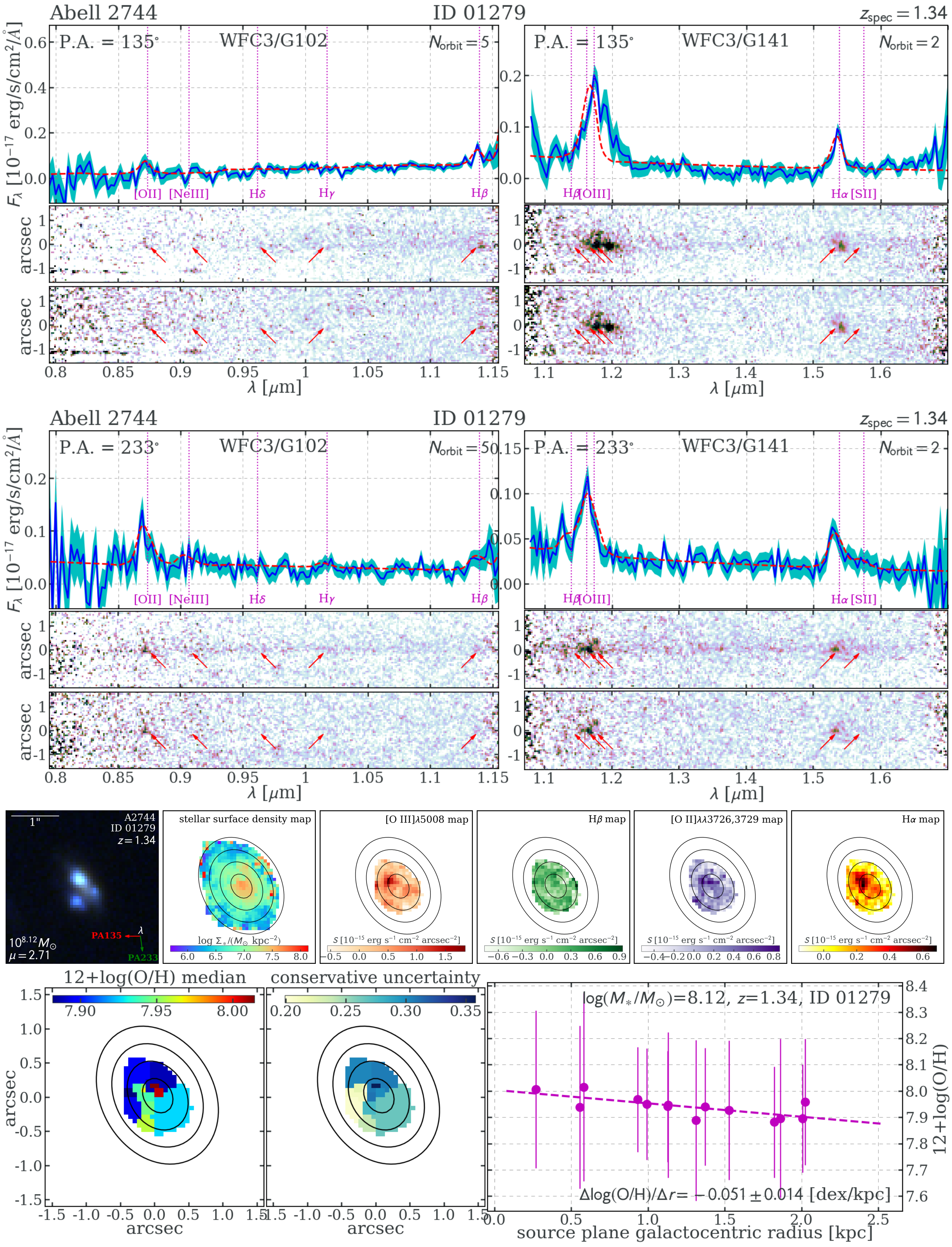

Figure 27. The source ID01279 in the field of Abell 2744 is shown.

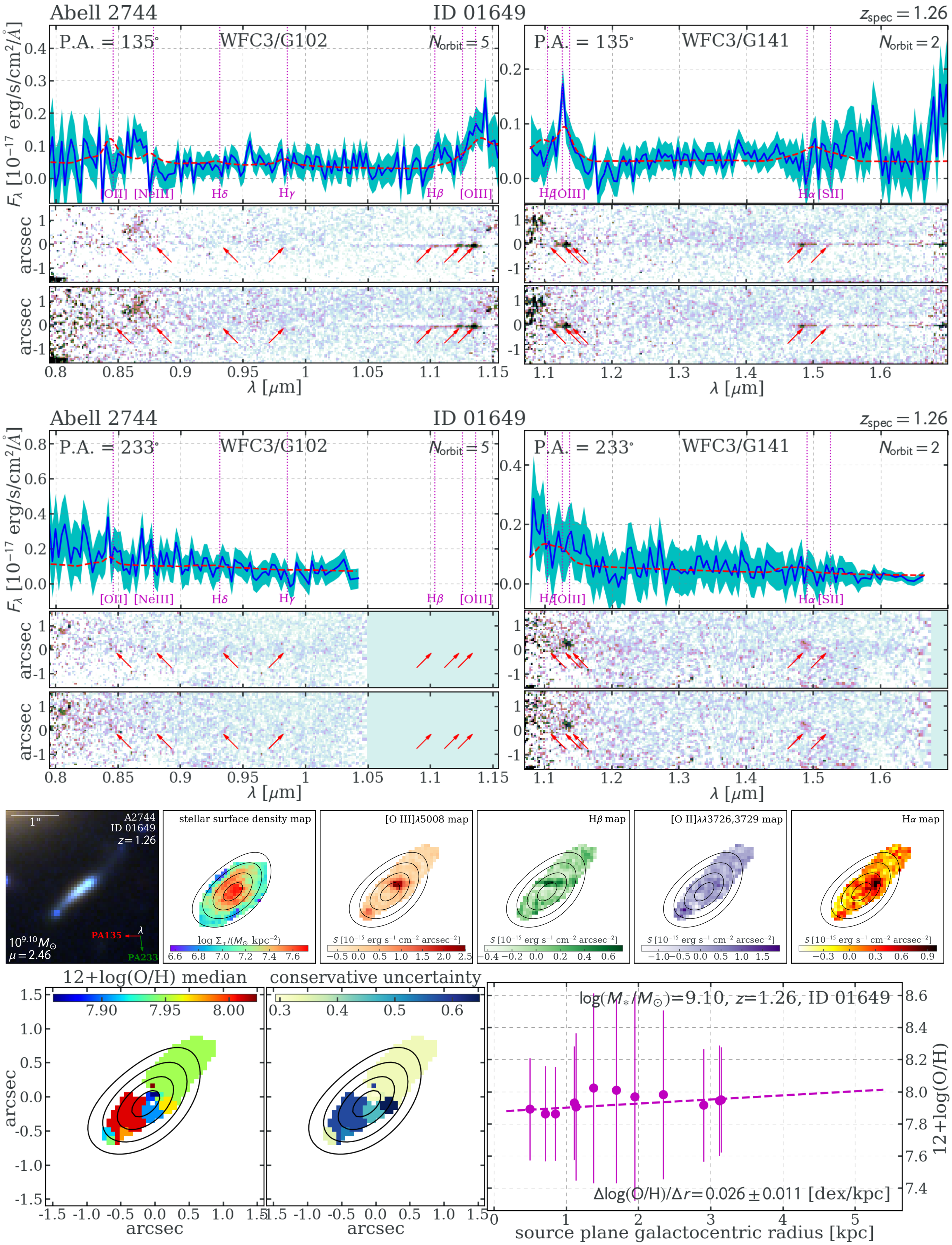

Figure 28. The source ID01649 in the field of Abell 2744 is shown.

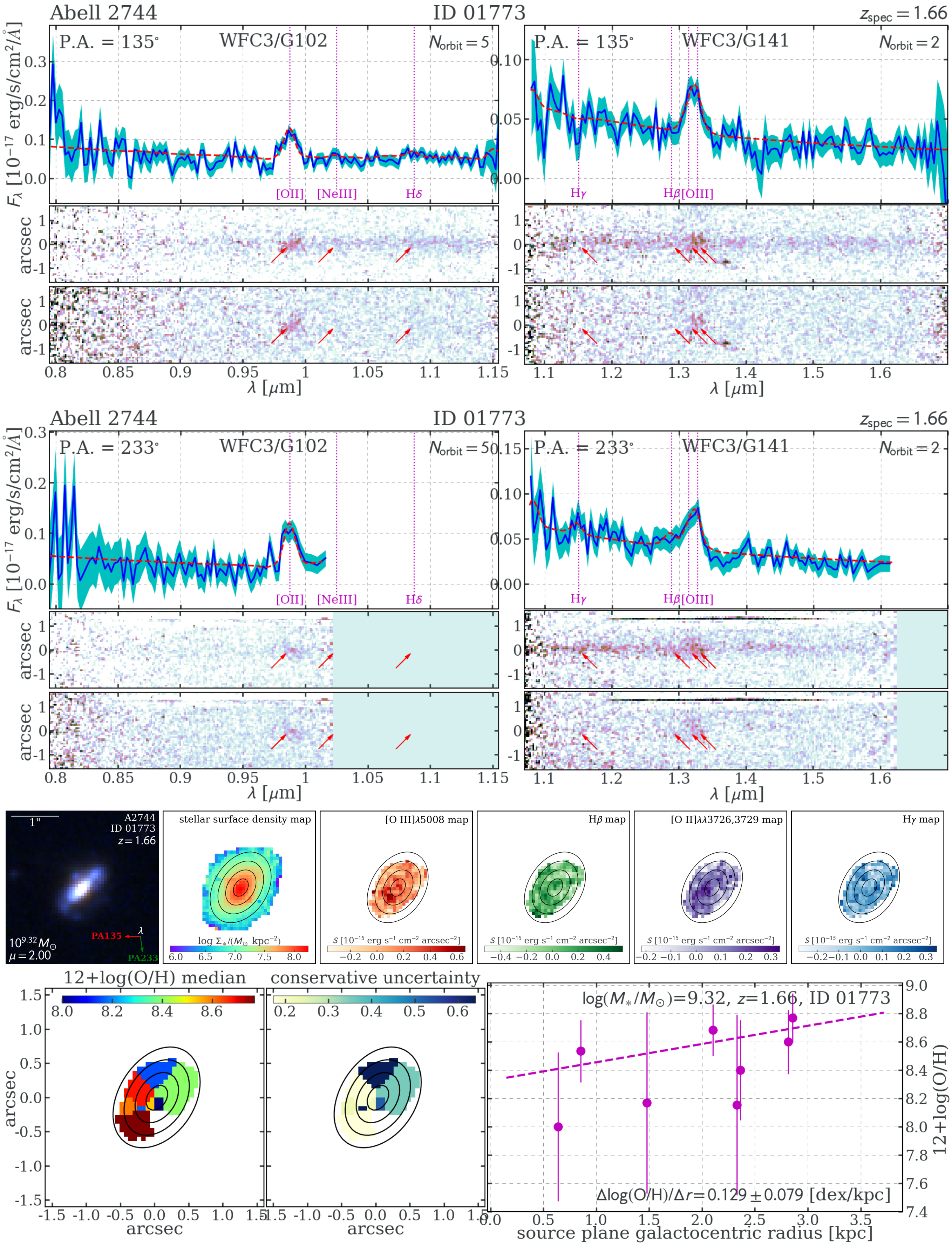

Figure 29. The source ID01773 in the field of Abell 2744 is shown.

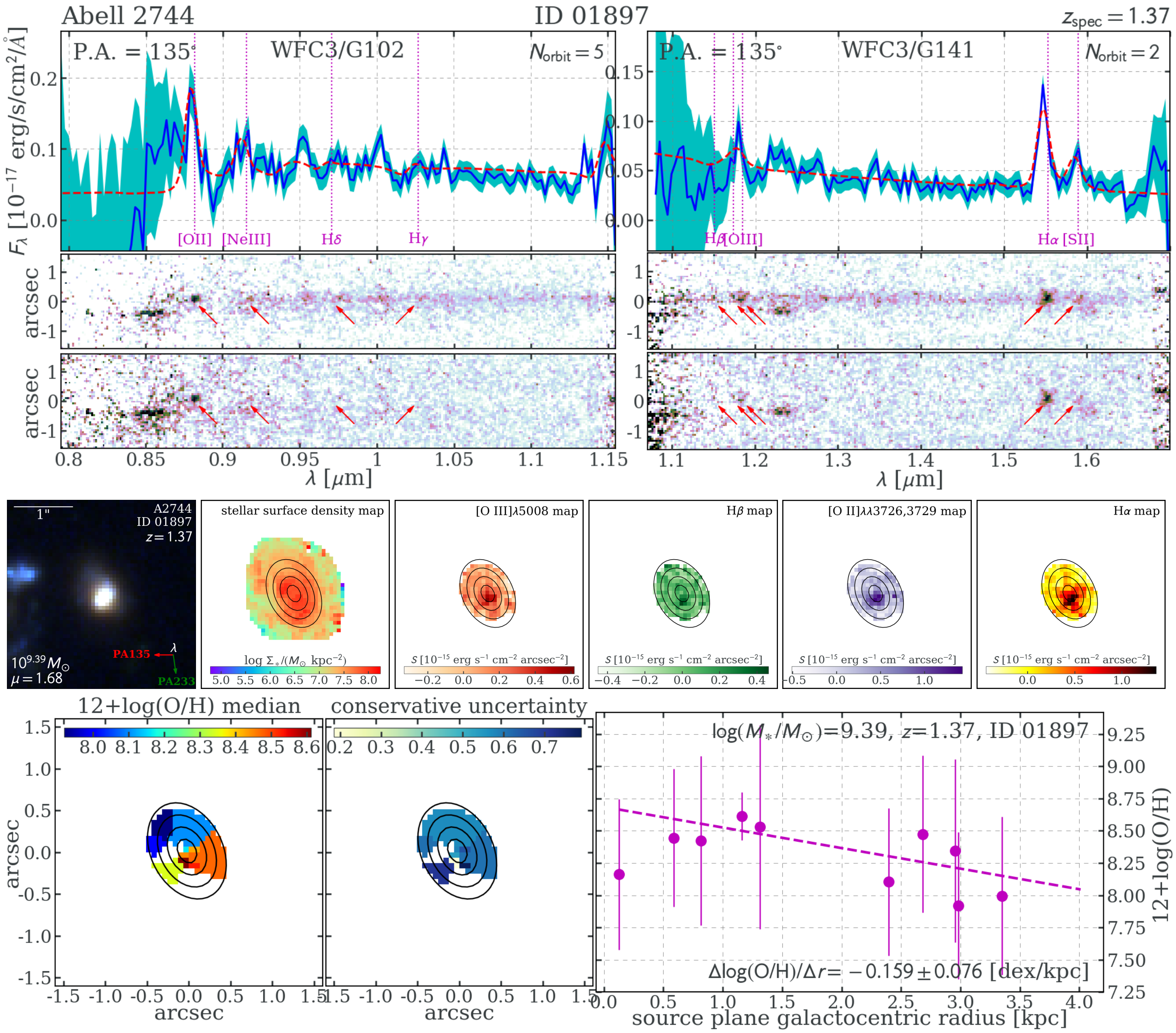

Figure 30. The source ID01897 in the field of Abell 2744 is shown.

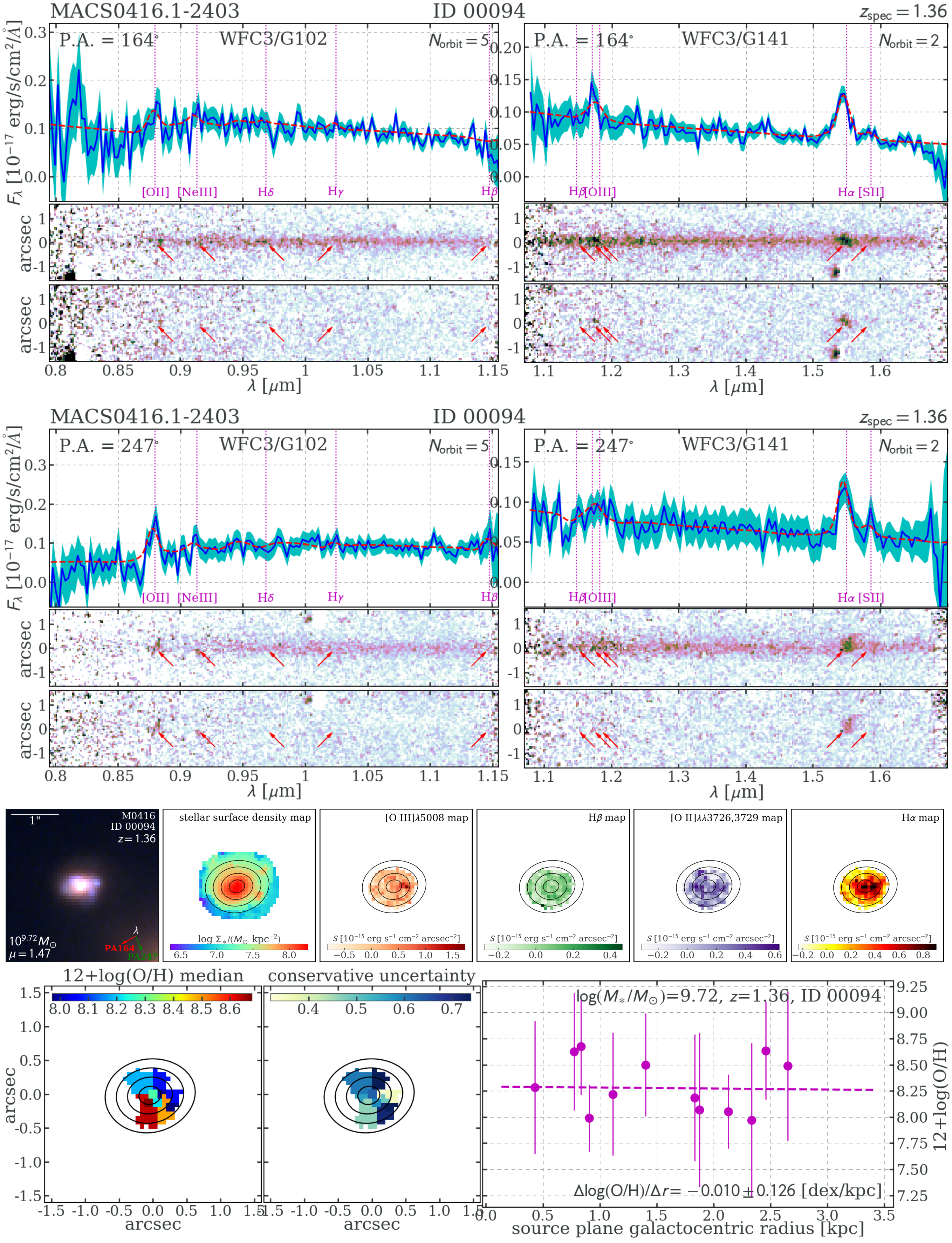

Figure 31. The source ID00094 in the field of MACS0416.1-2403 is shown.

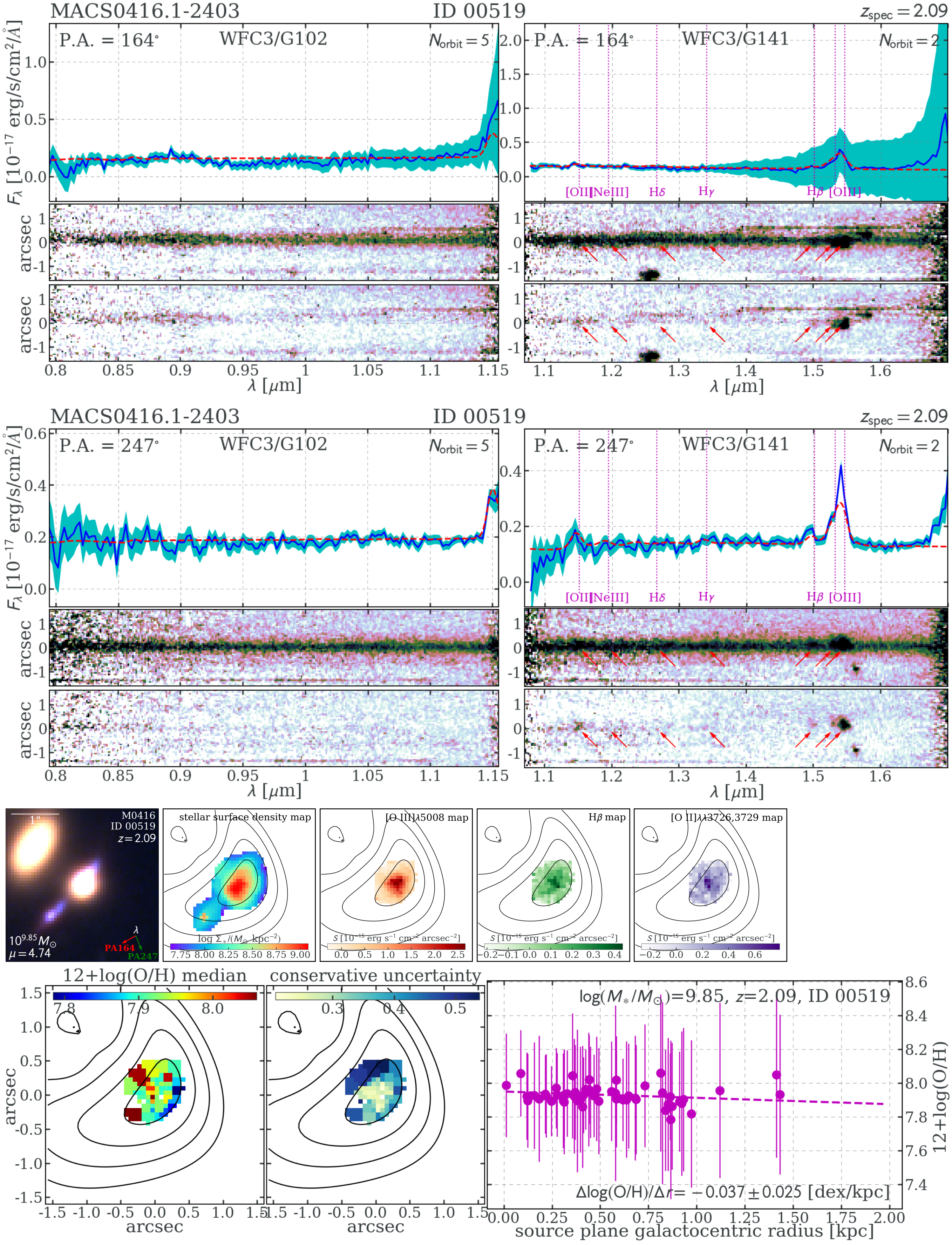

Figure 32. The source ID00519 in the field of MACS0416.1-2403 is shown.

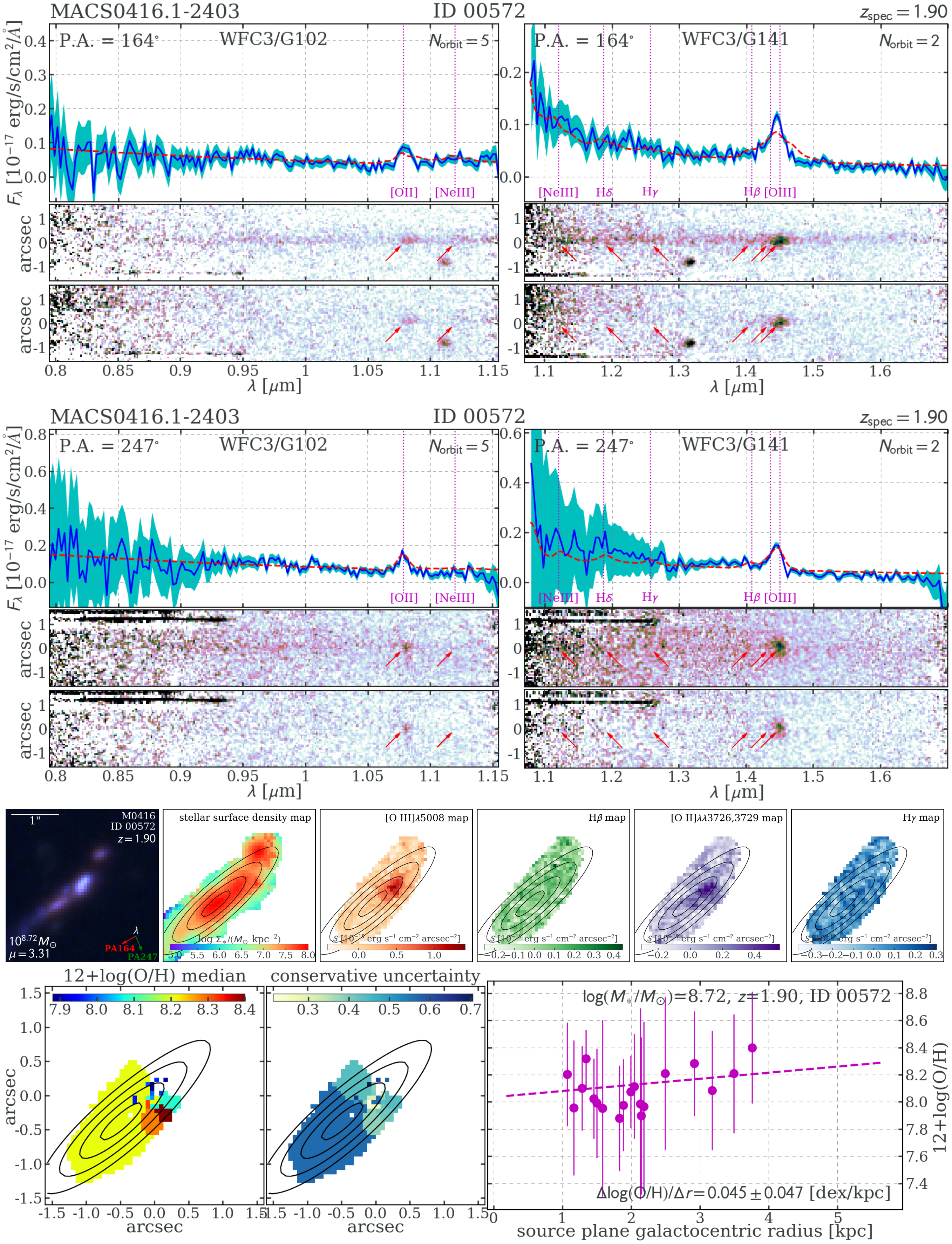

Figure 33. The source ID00572 in the field of MACS0416.1-2403 is shown.

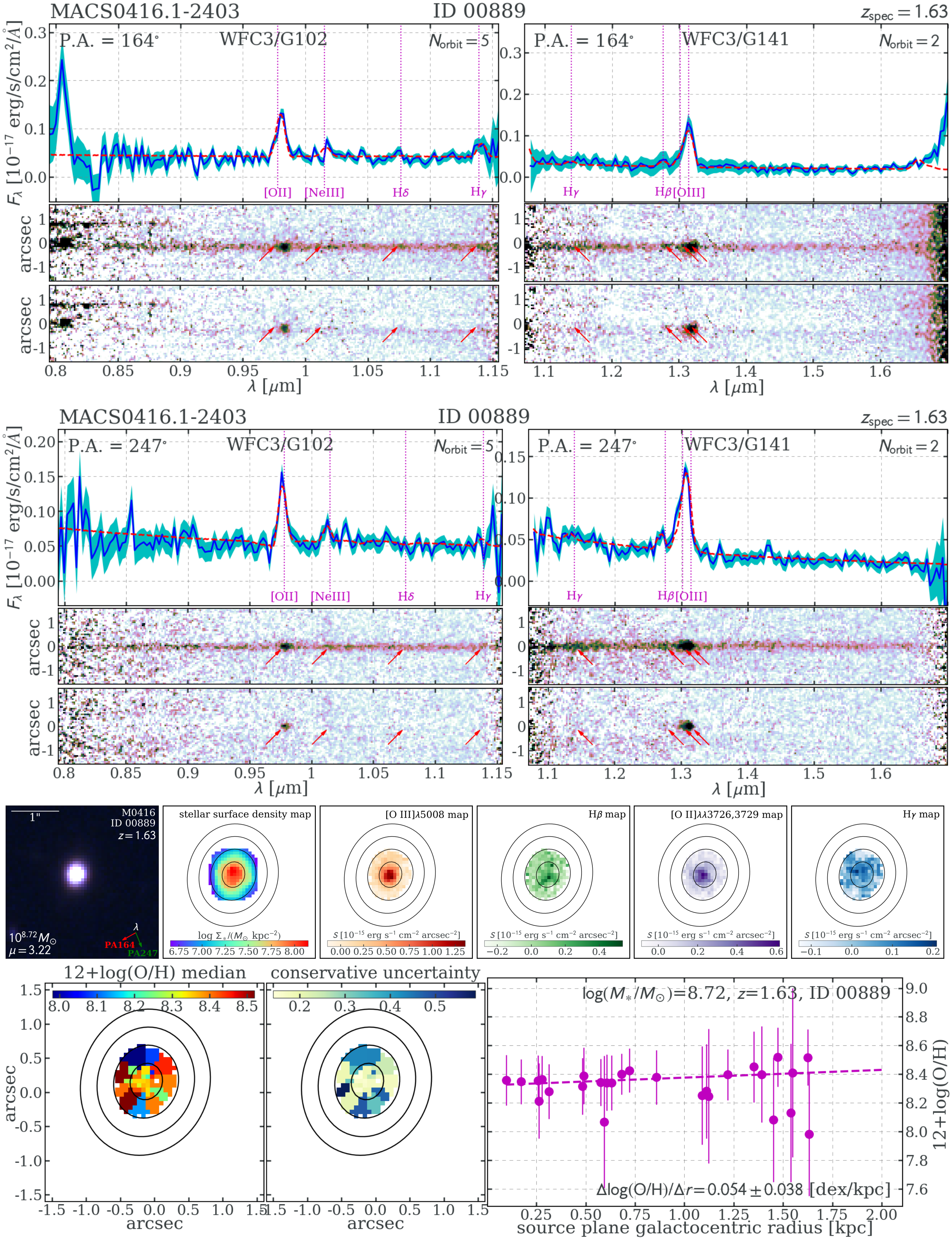

Figure 34. The source ID00889 in the field of MACS0416.1-2403 is shown.

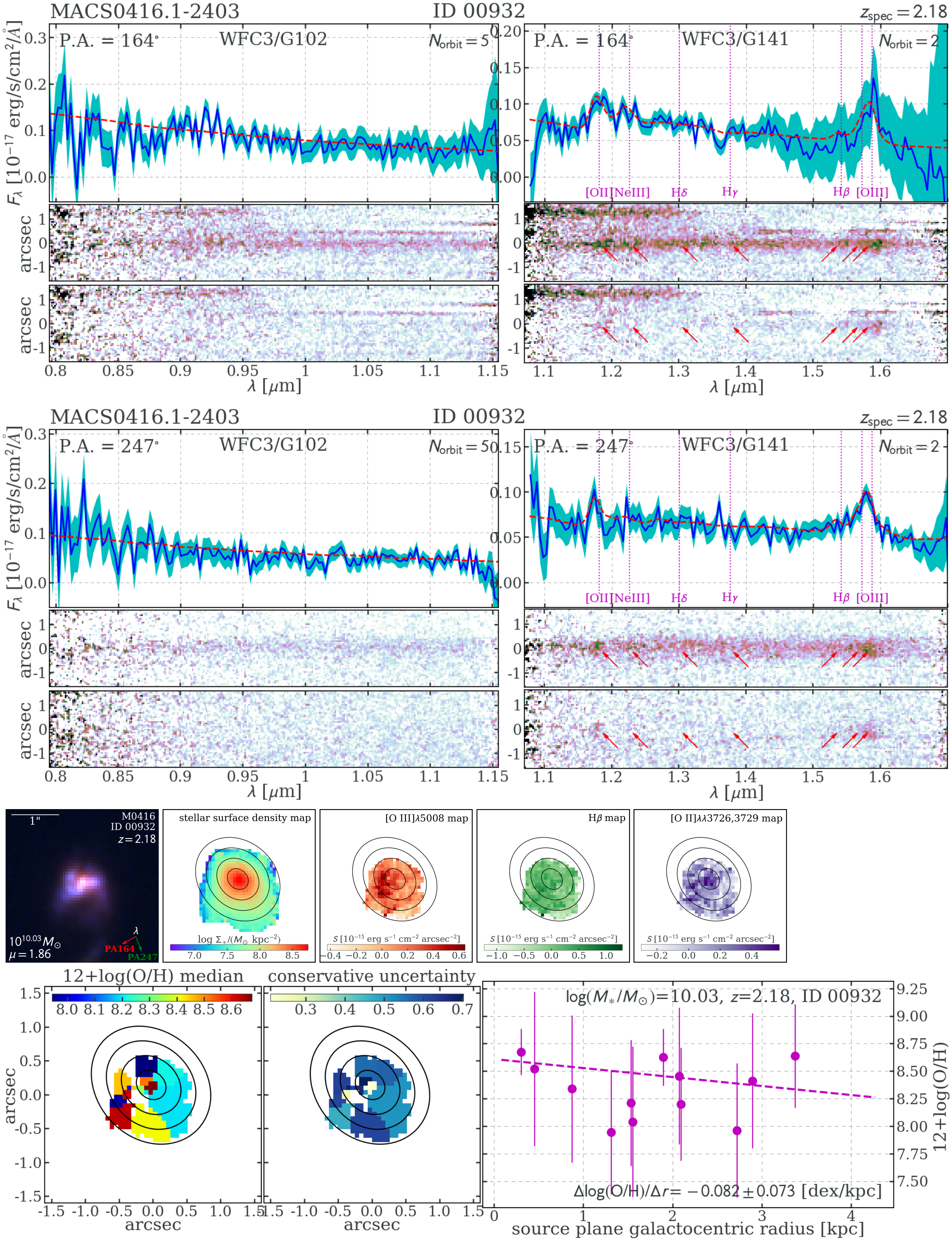

Figure 35. The source ID00932 in the field of MACS0416.1-2403 is shown.

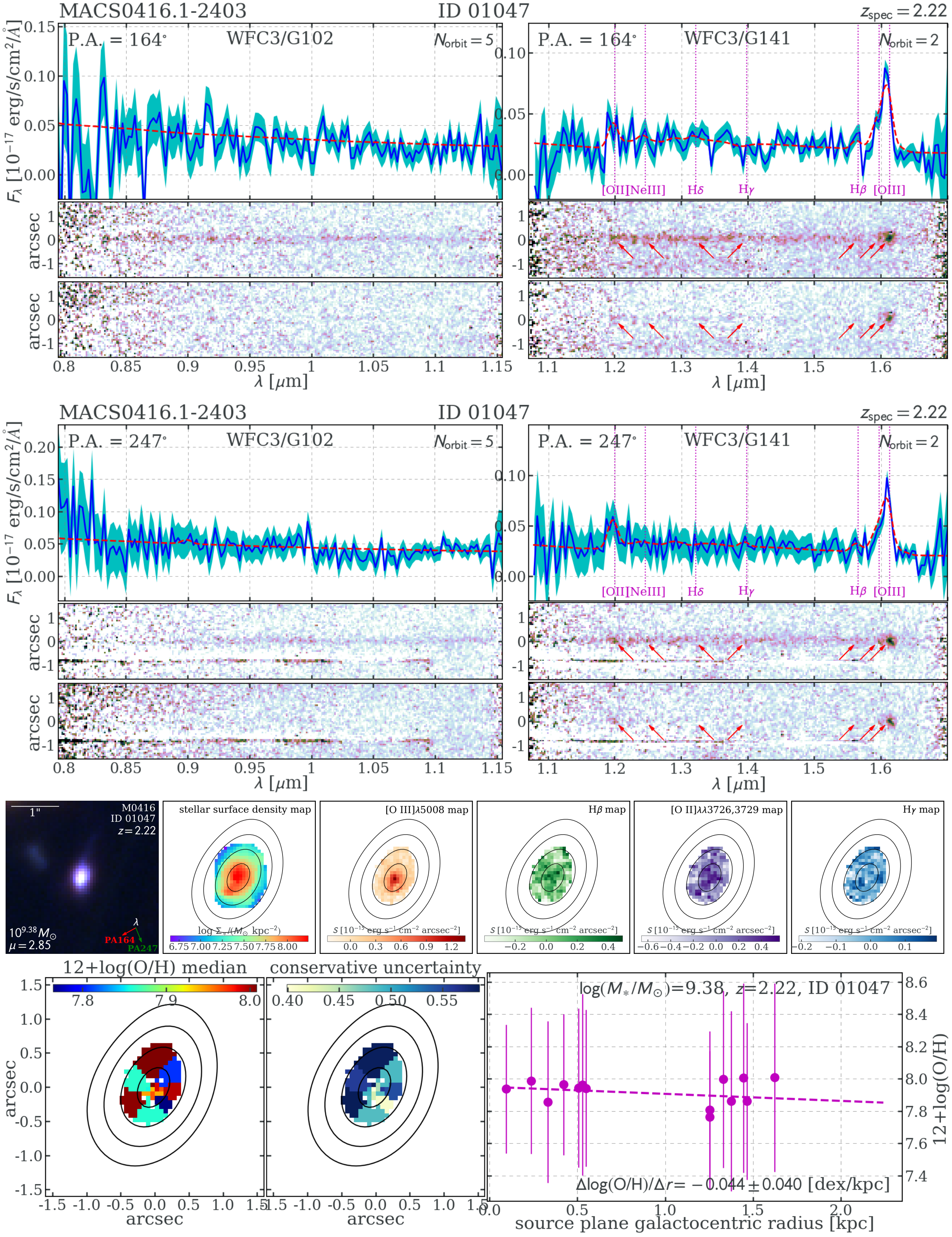

Figure 36. The source ID01047 in the field of MACS0416.1-2403 is shown.

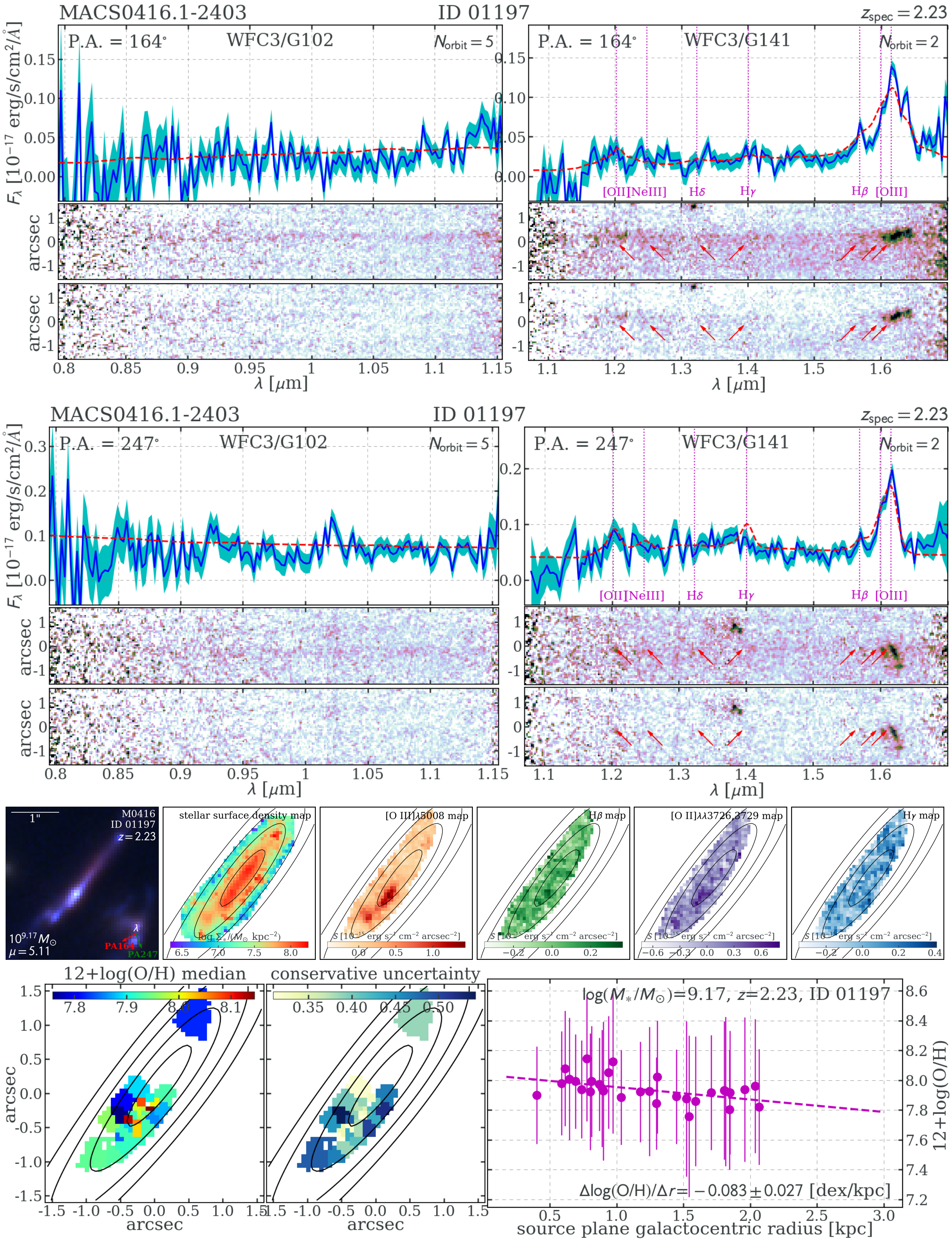

Figure 37. The source ID01197 in the field of MACS0416.1-2403 is shown.

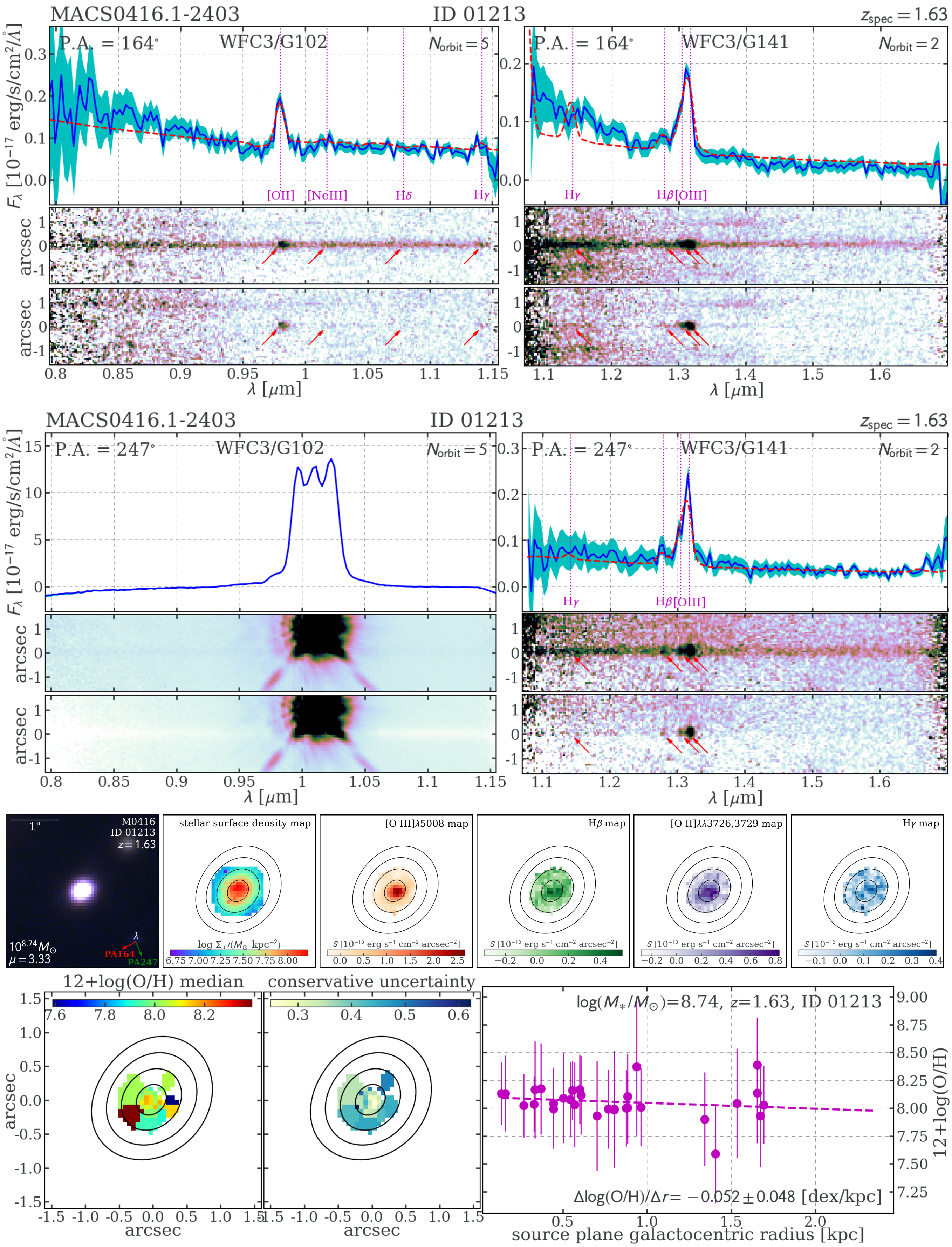

Figure 38. The source ID01213 in the field of MACS0416.1-2403 is shown.

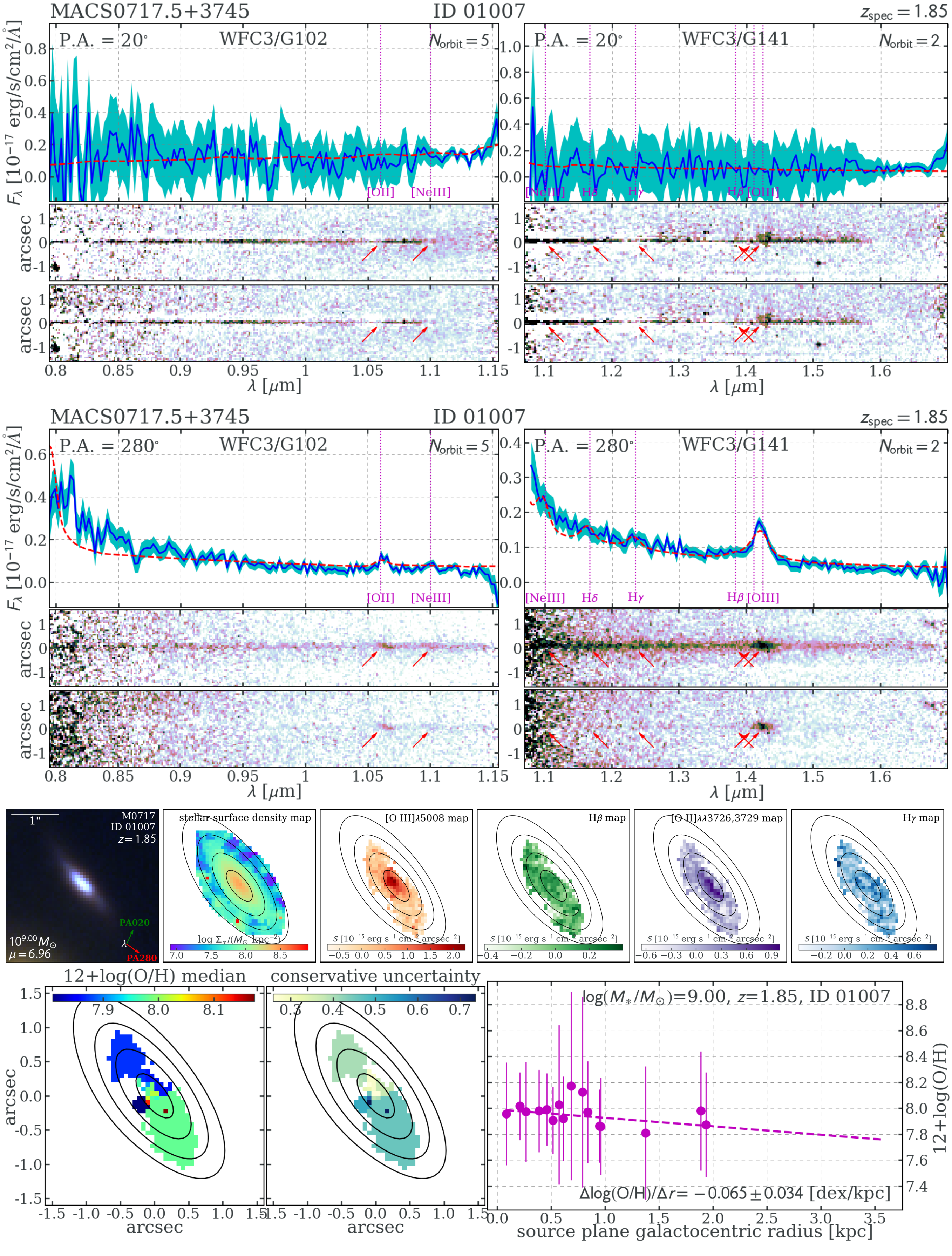

Figure 39. The source ID01007 in the field of MACS0717.5+3745 is shown.

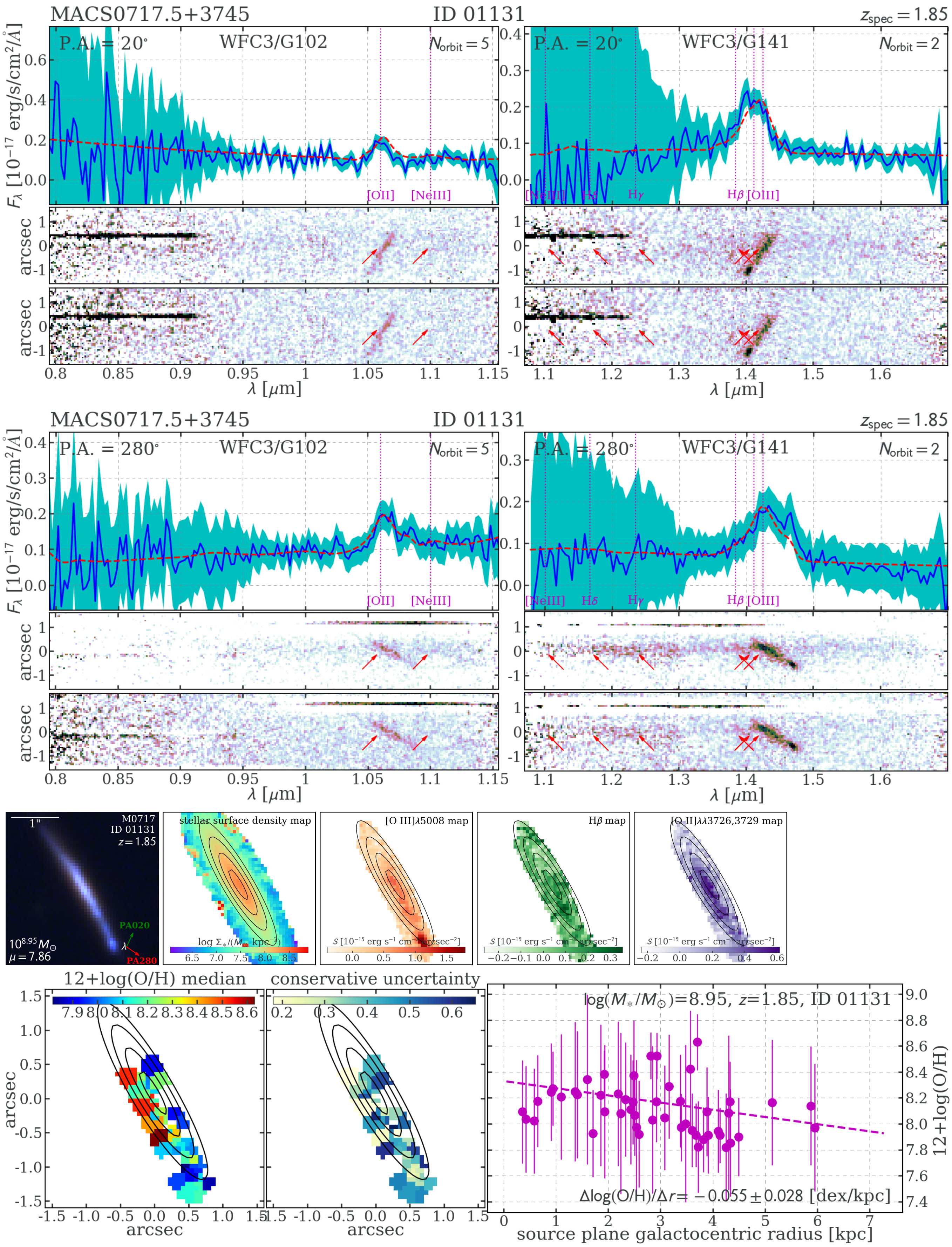

Figure 40. The source ID01131 in the field of MACS0717.5+3745 is shown.

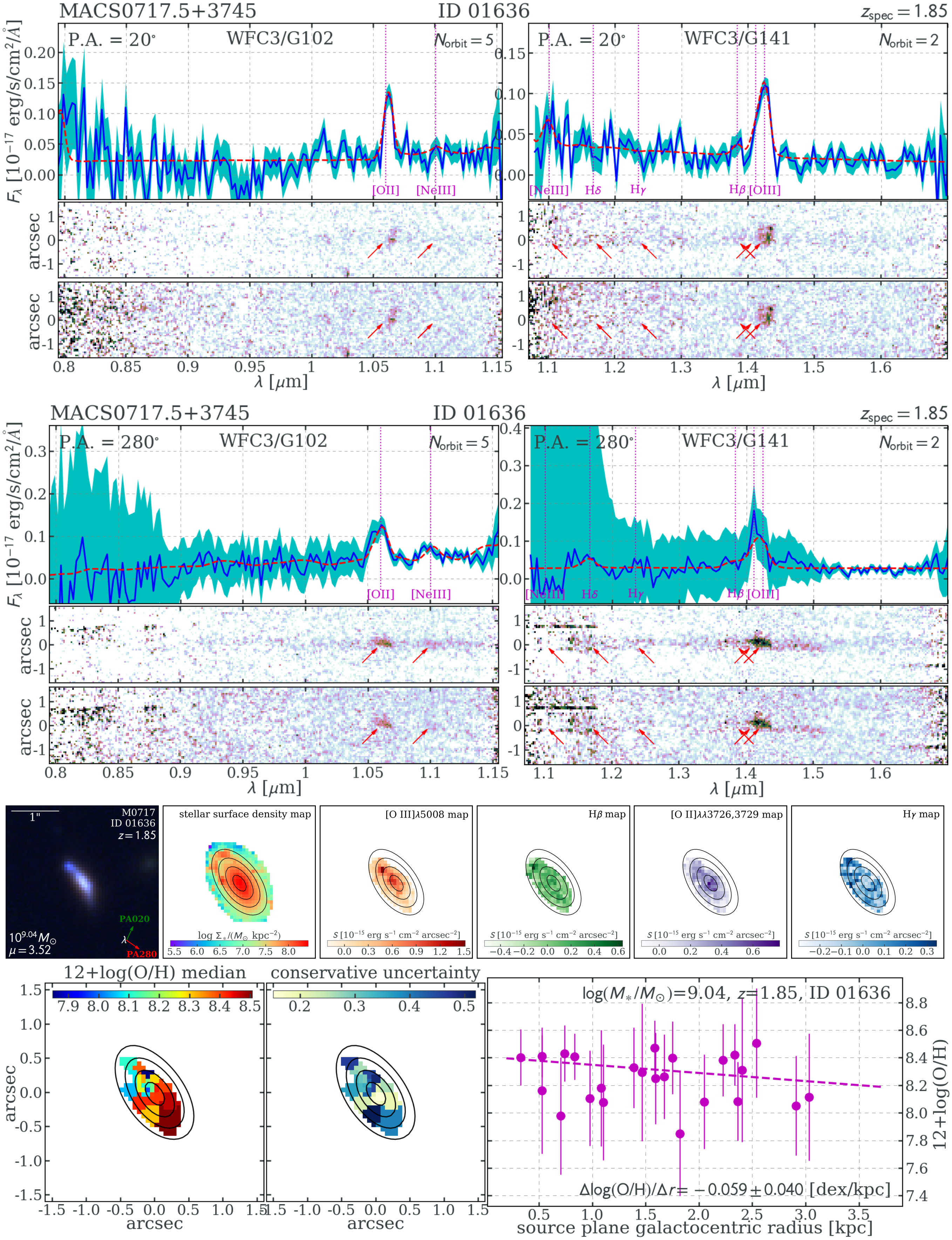

Figure 41. The source ID01636 in the field of MACS0717.5+3745 is shown.

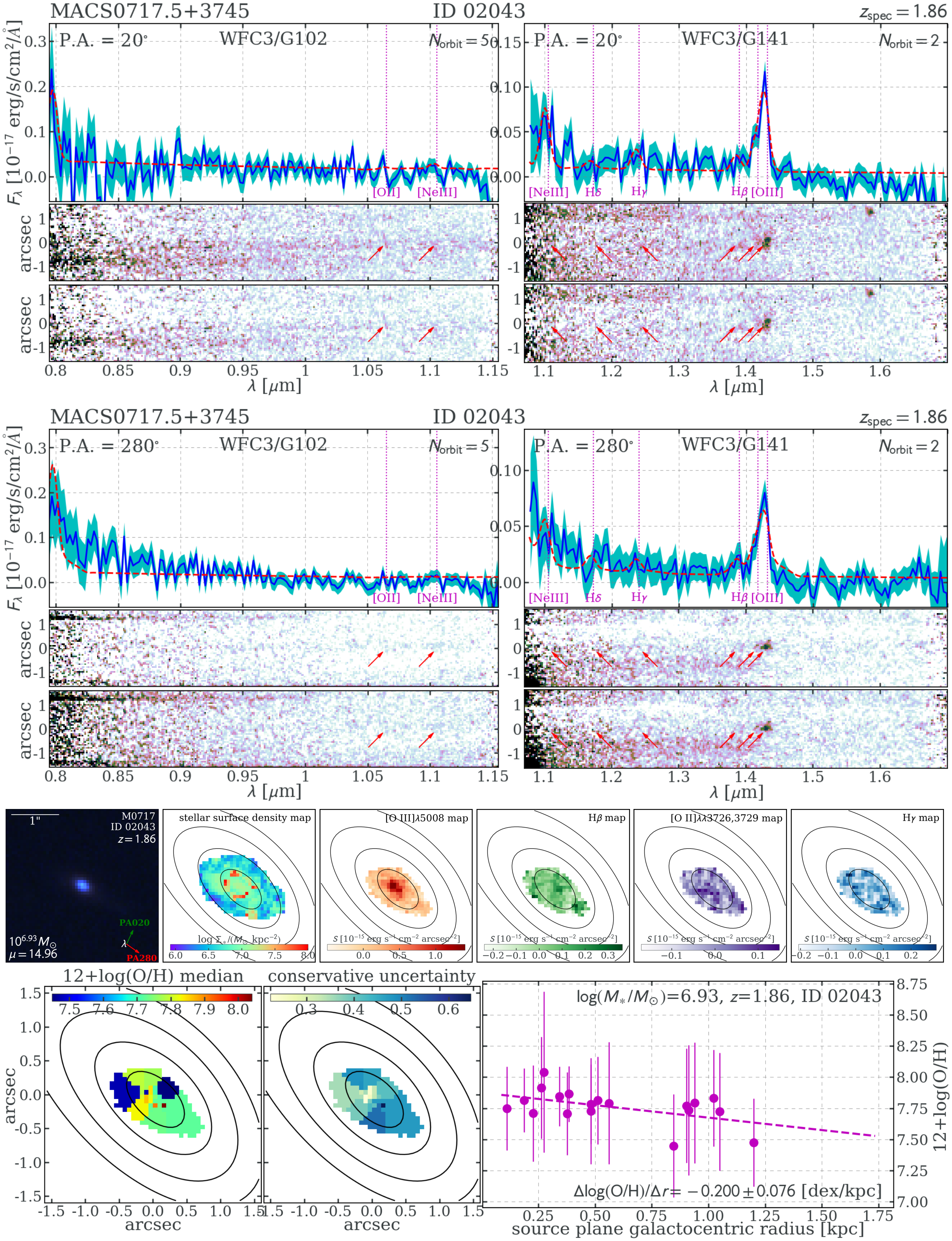

Figure 42. The source ID02043 in the field of MACS0717.5+3745 is shown.

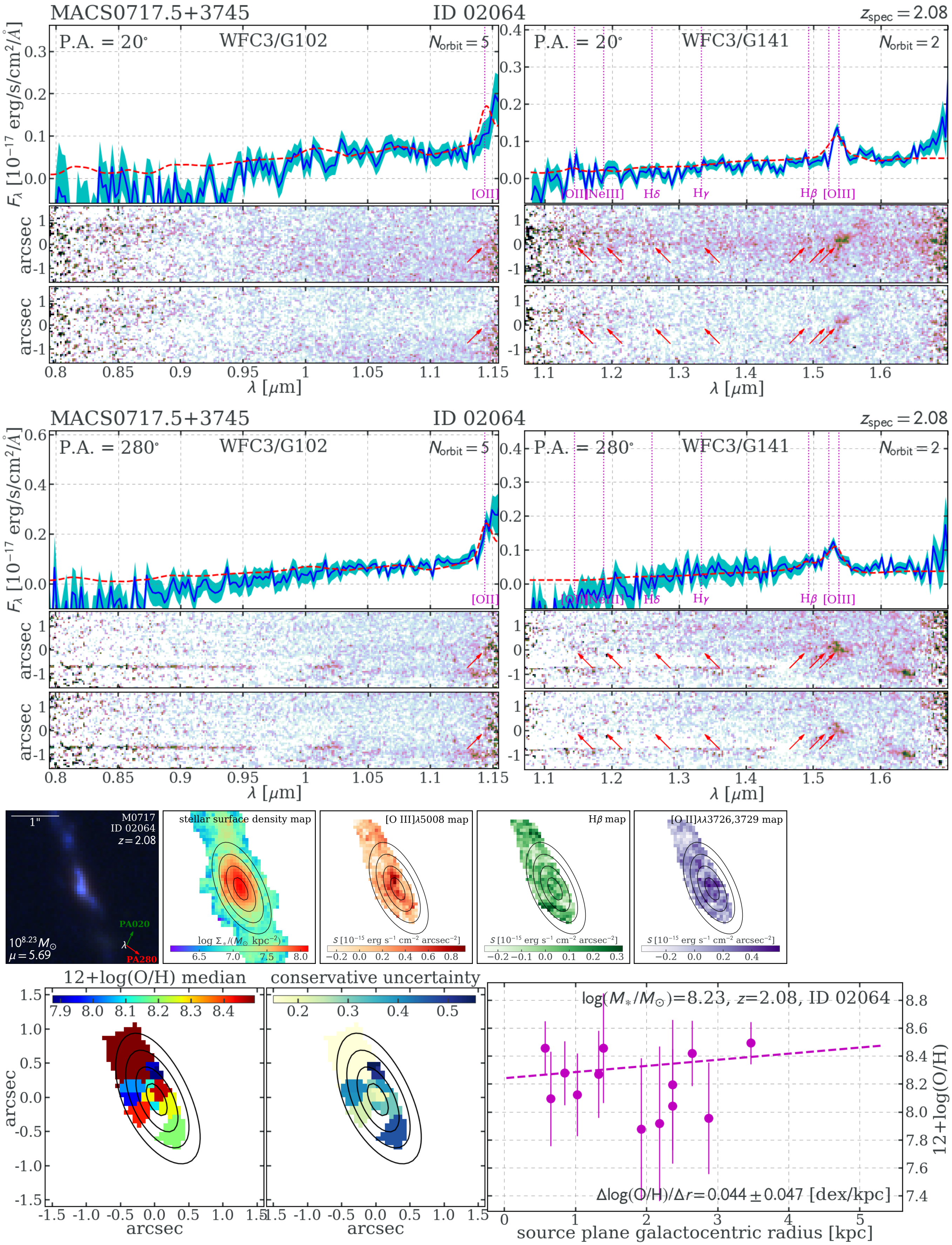

Figure 43. The source ID02064 in the field of MACS0717.5+3745 is shown.

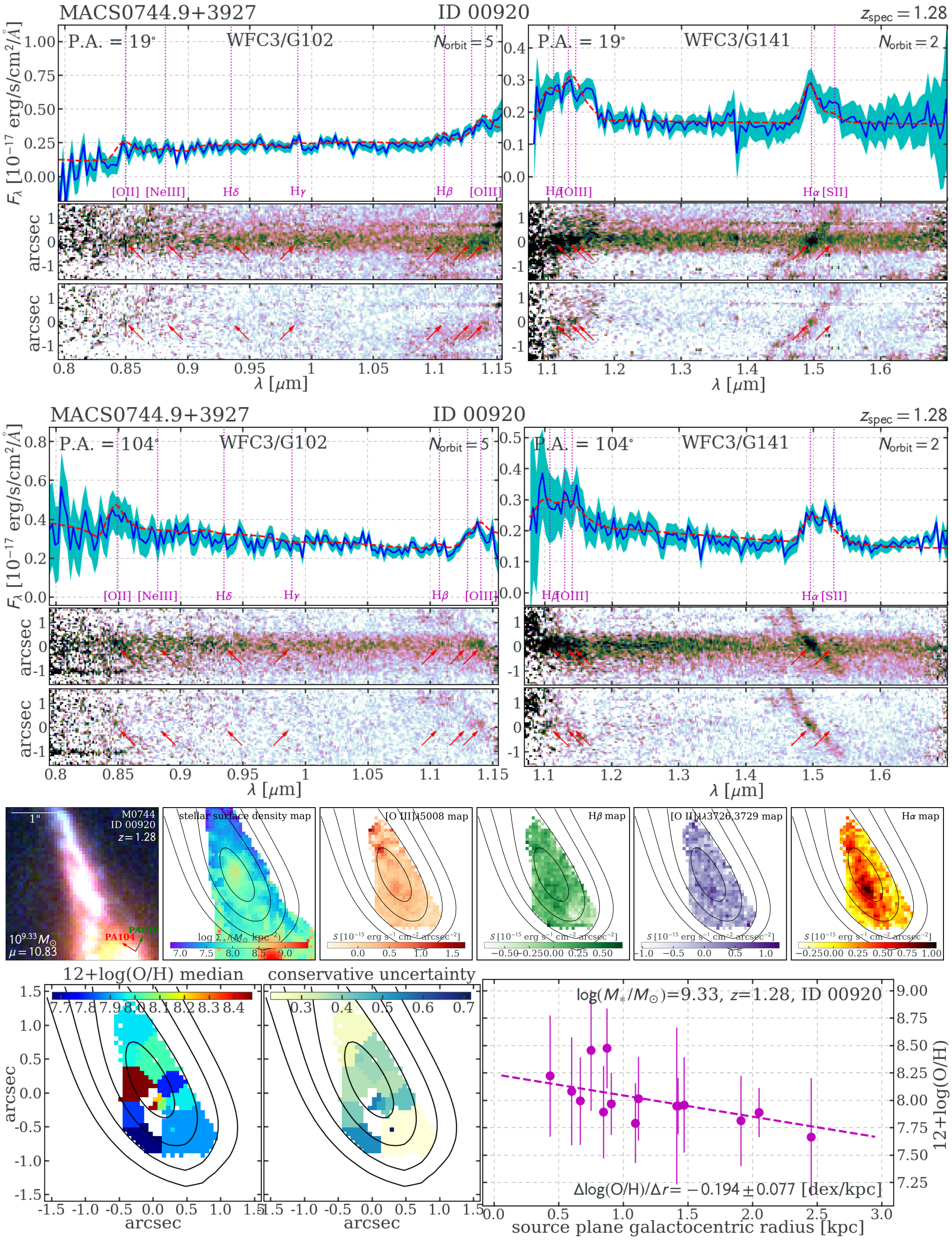

Figure 44. The source ID00920 in the field of MACS0744.9+3927 is shown.

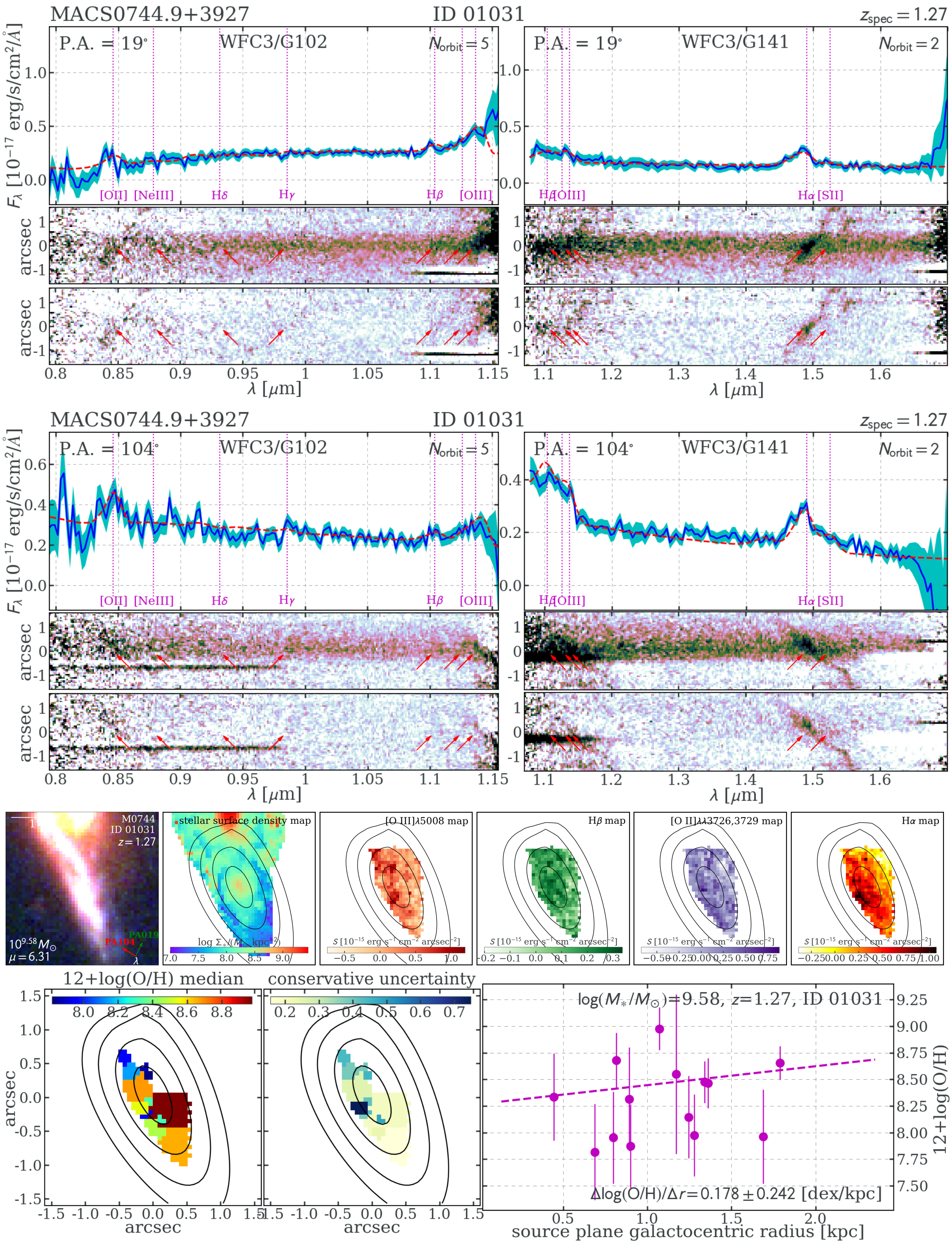

Figure 45. The source ID01031 in the field of MACS0744.9+3927 is shown.

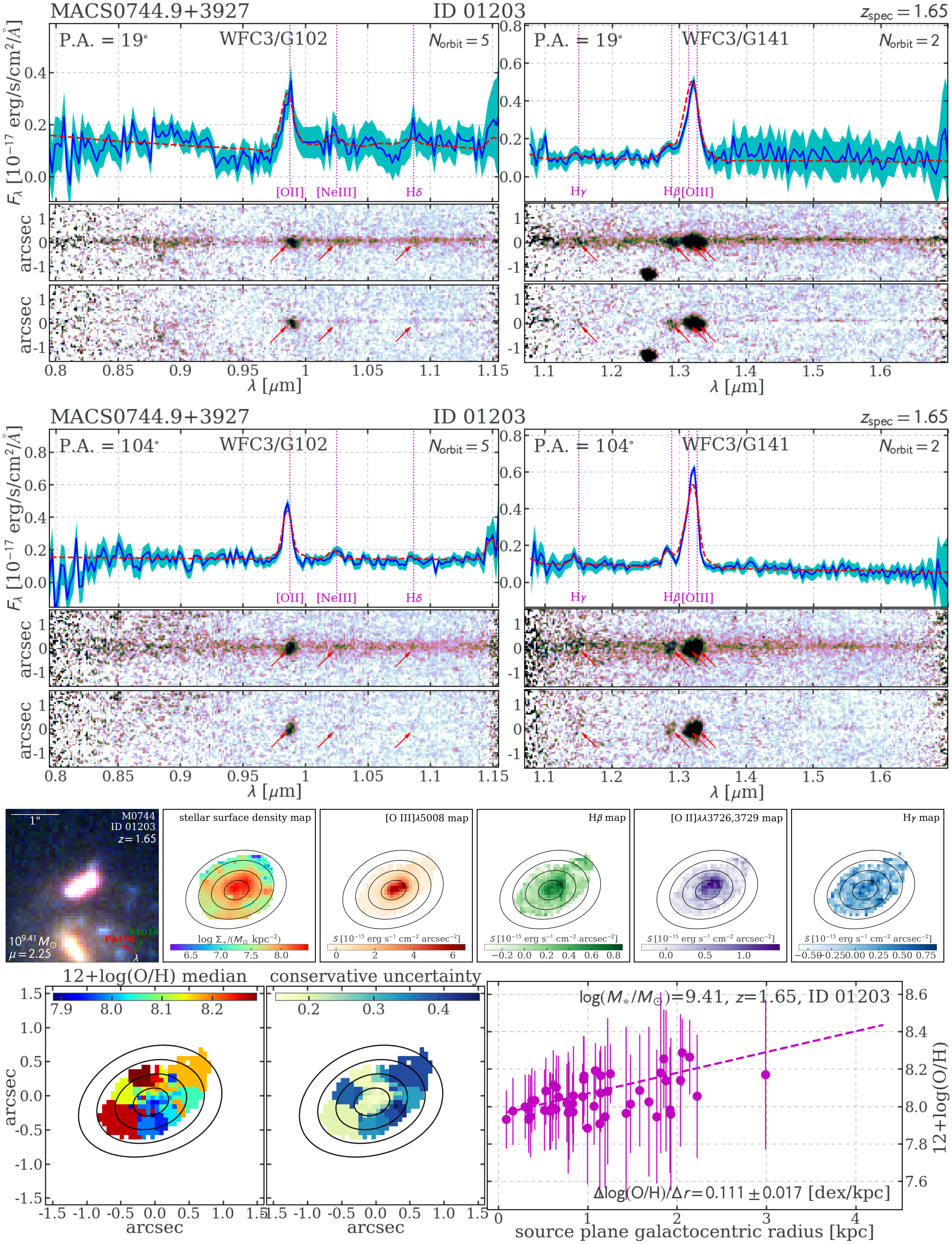

Figure 46. The source ID01203 in the field of MACS0744.9+3927 is shown.

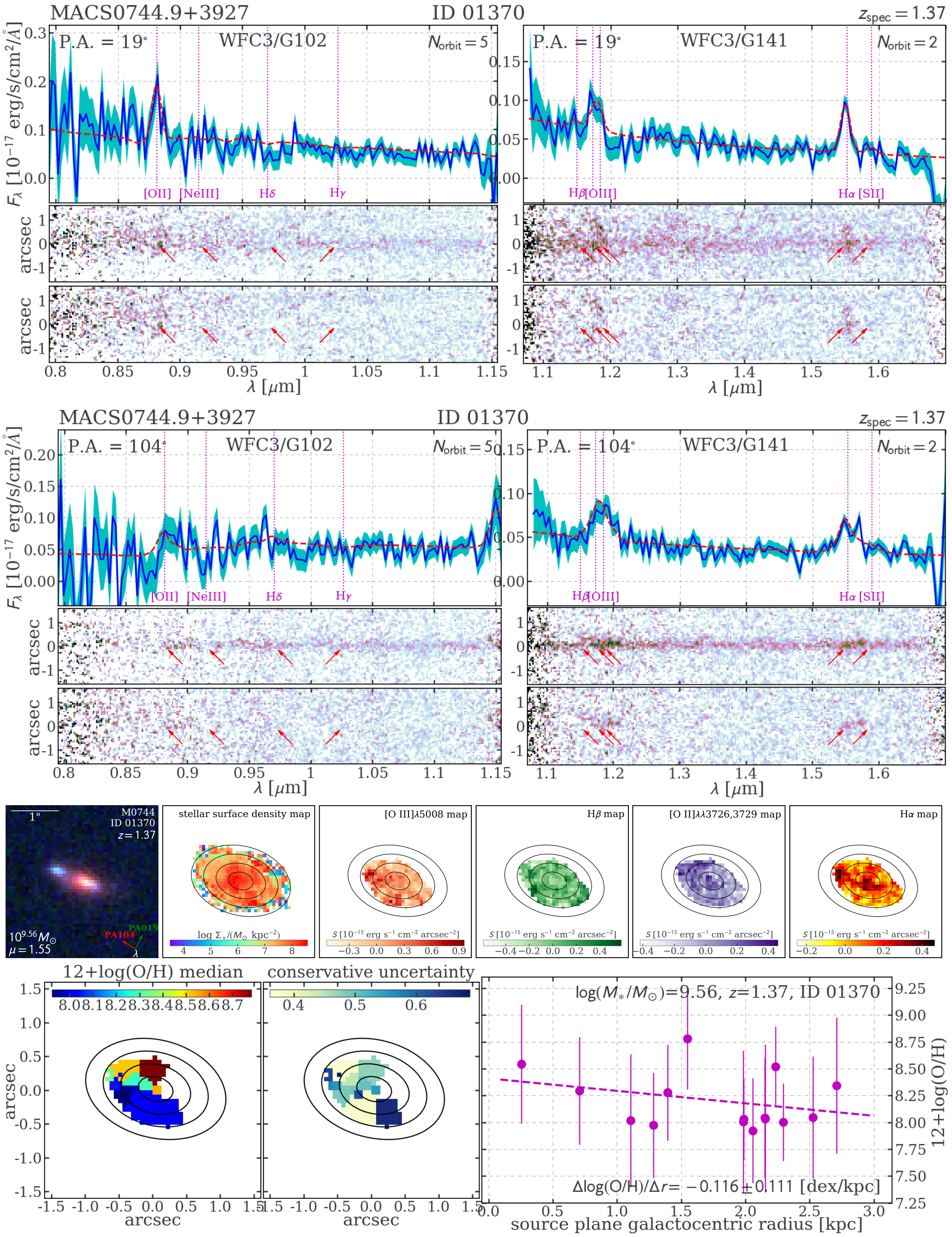

Figure 47. The source ID01370 in the field of MACS0744.9+3927 is shown.

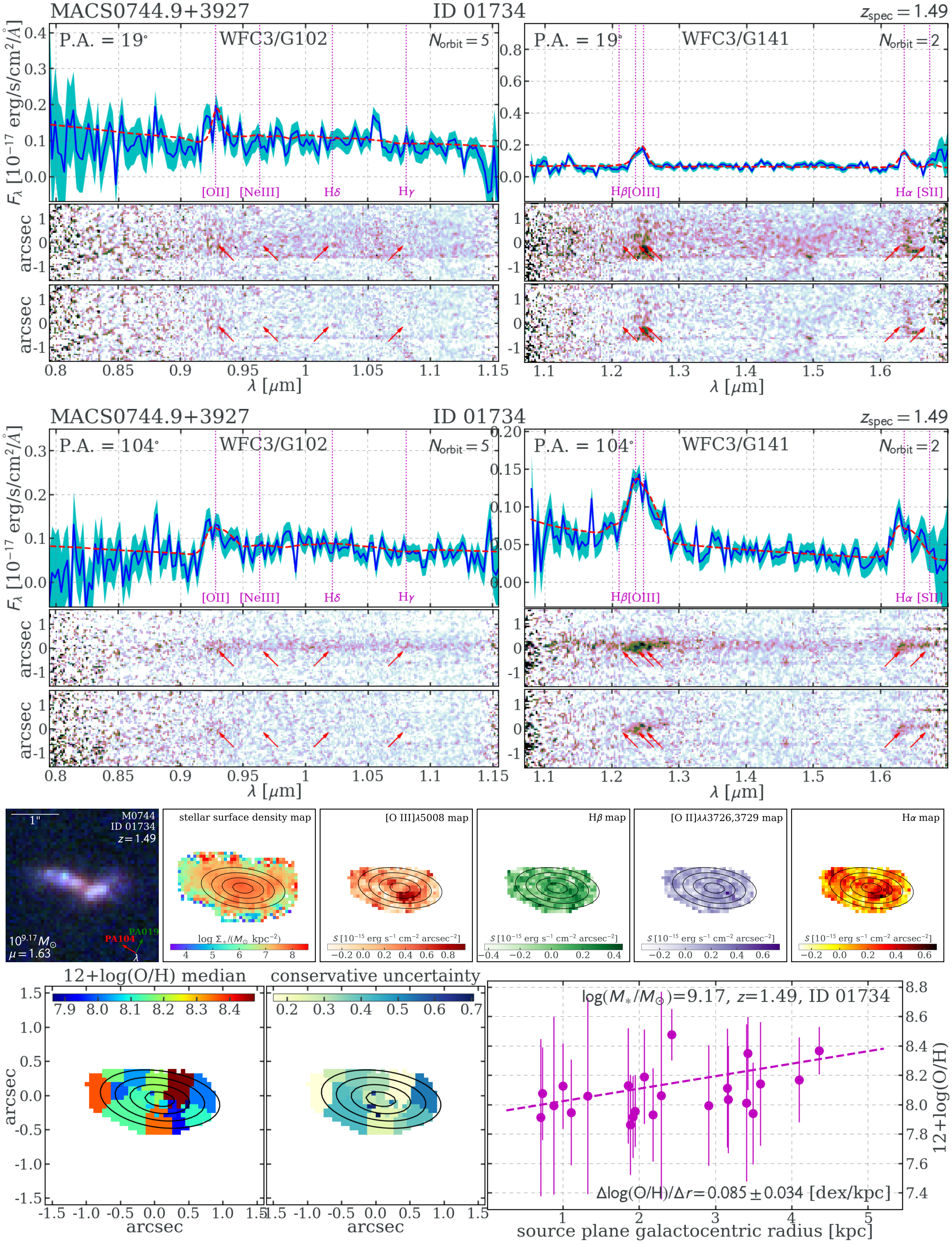

Figure 48. The source ID01734 in the field of MACS0744.9+3927 is shown.

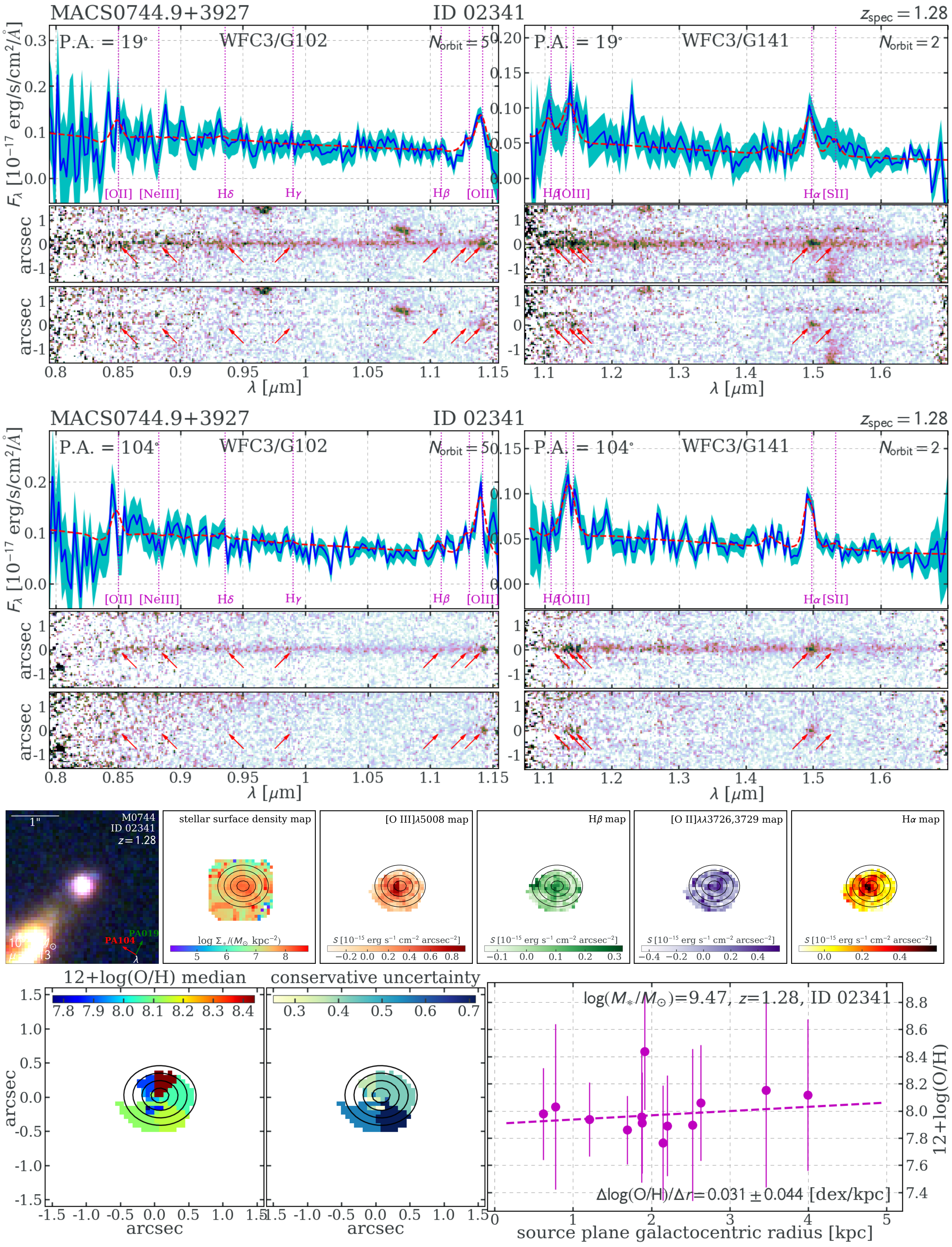

Figure 49. The source ID02341 in the field of MACS0744.9+3927 is shown.

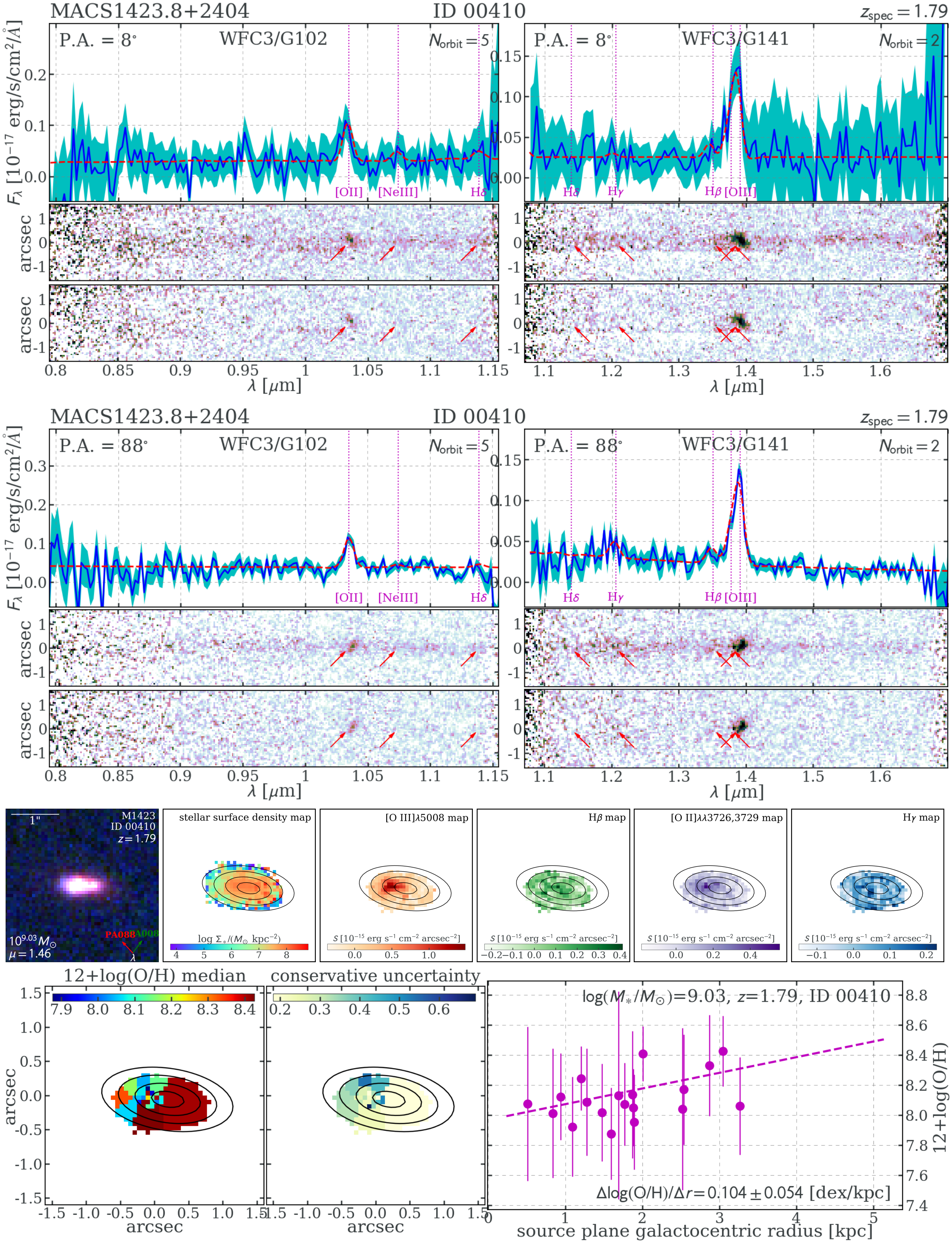

Figure 50. The source ID00410 in the field of MACS1423.8+2404 is shown.

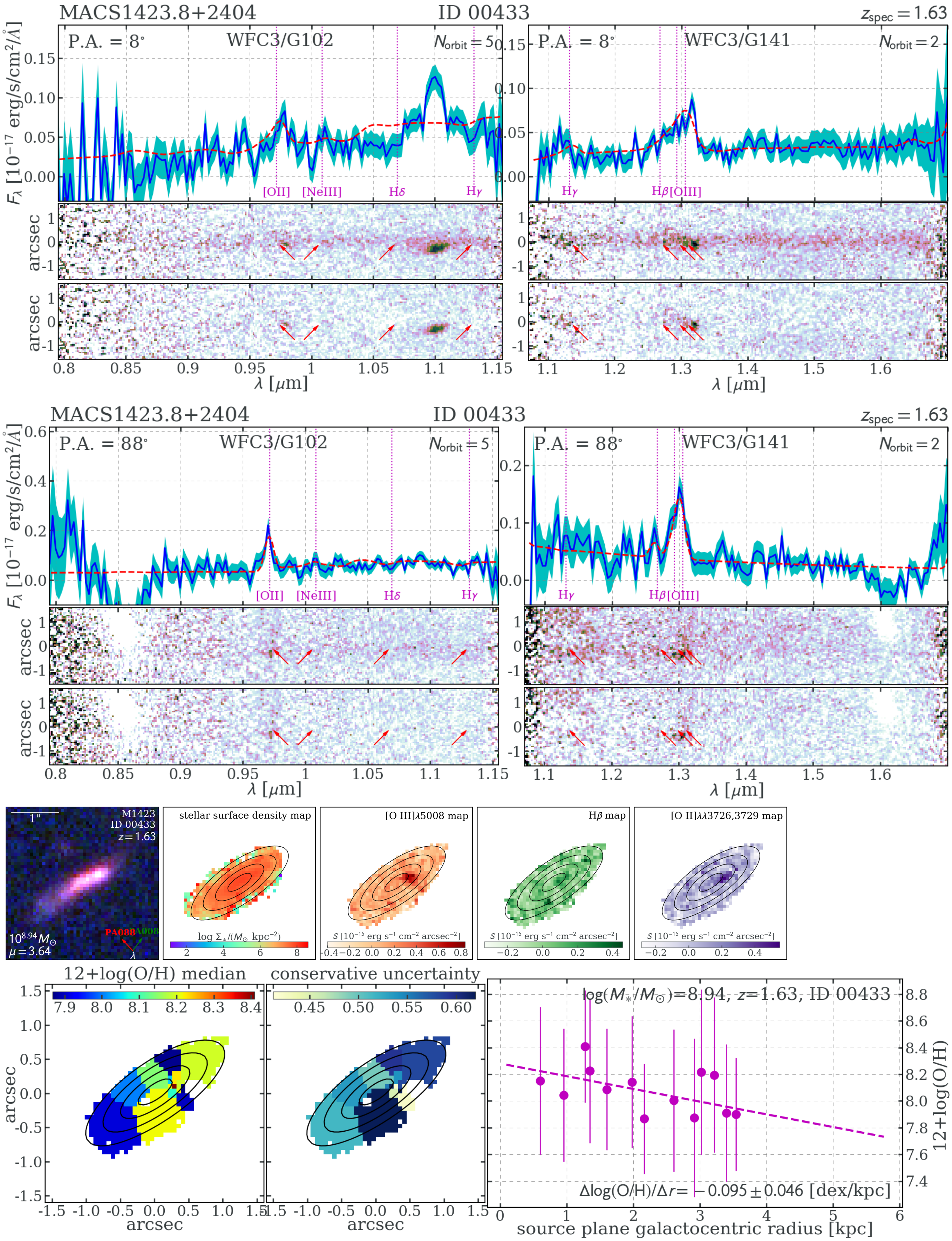

Figure 51. The source ID00433 in the field of MACS1423.8+2404 is shown.

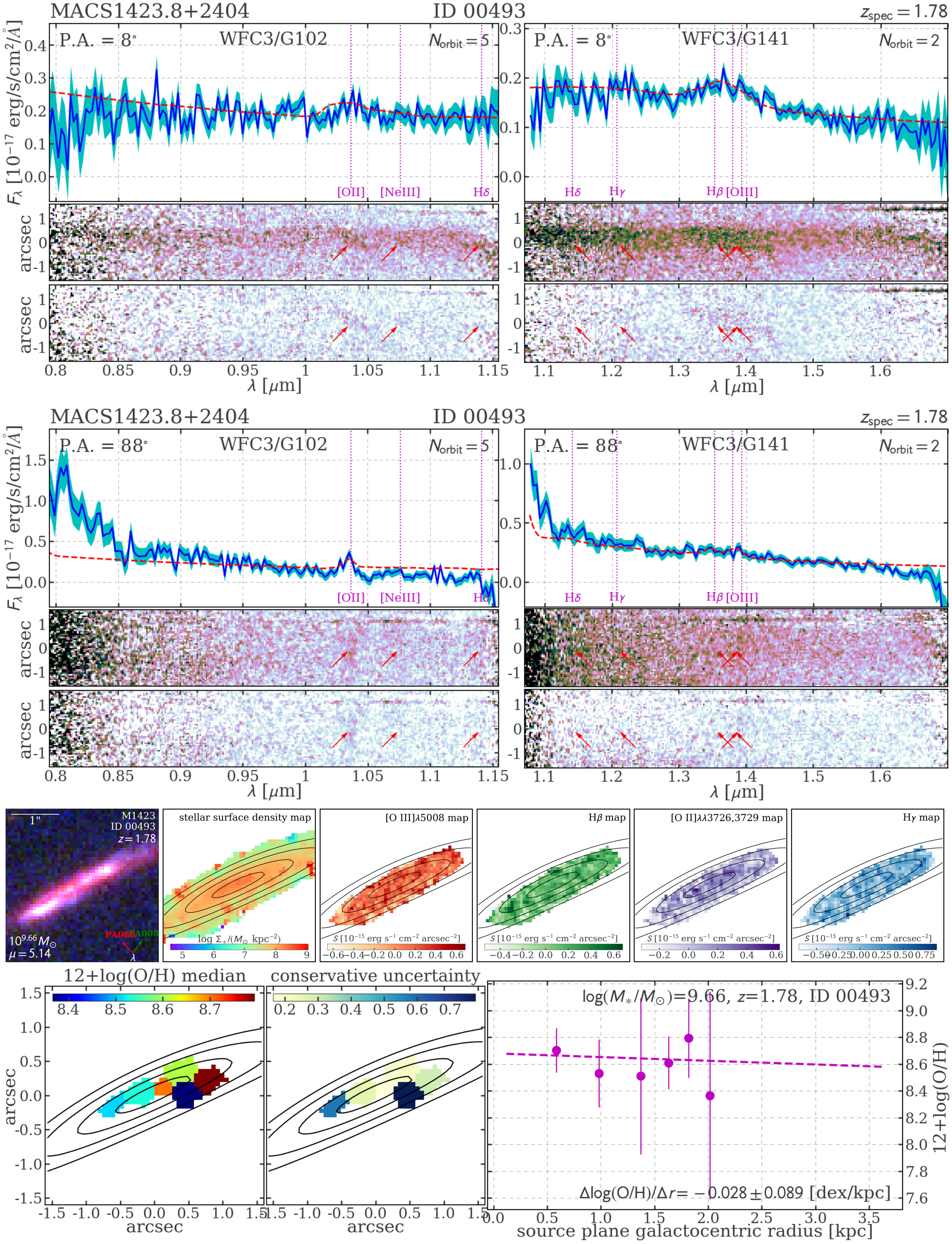

Figure 52. The source ID00493 in the field of MACS1423.8+2404 is shown.

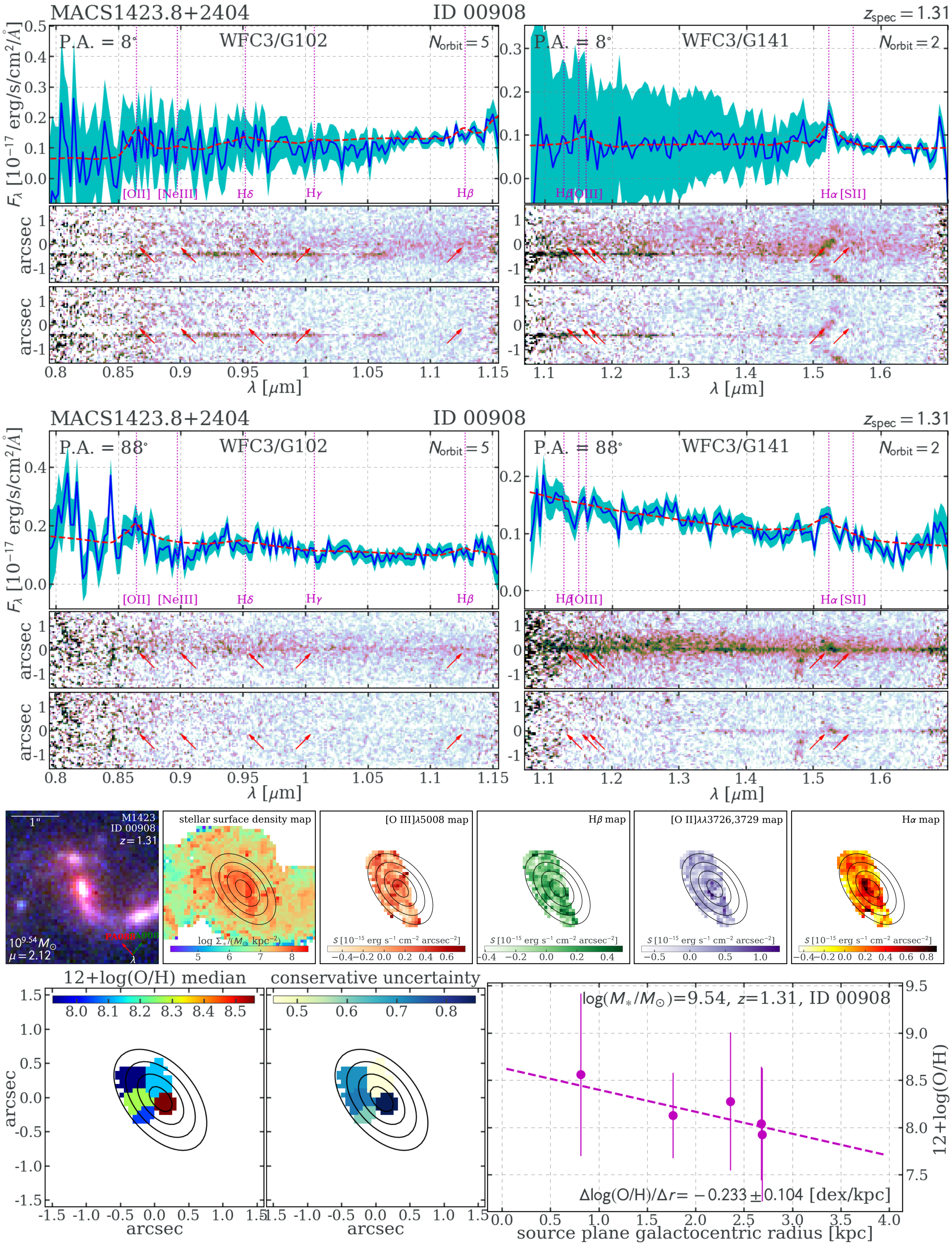

Figure 53. The source ID00908 in the field of MACS1423.8+2404 is shown.

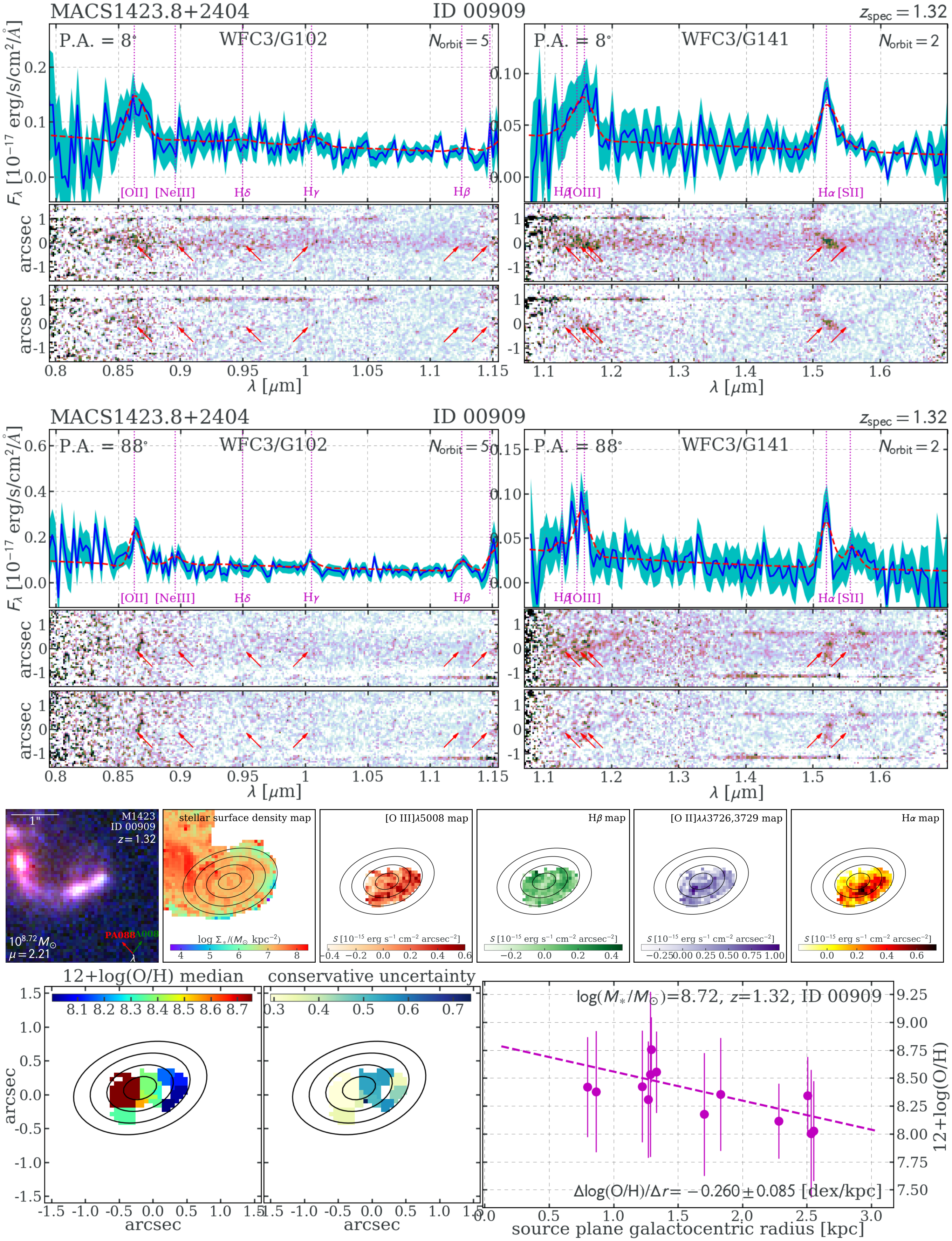

Figure 54. The source ID00909 in the field of MACS1423.8+2404 is shown.

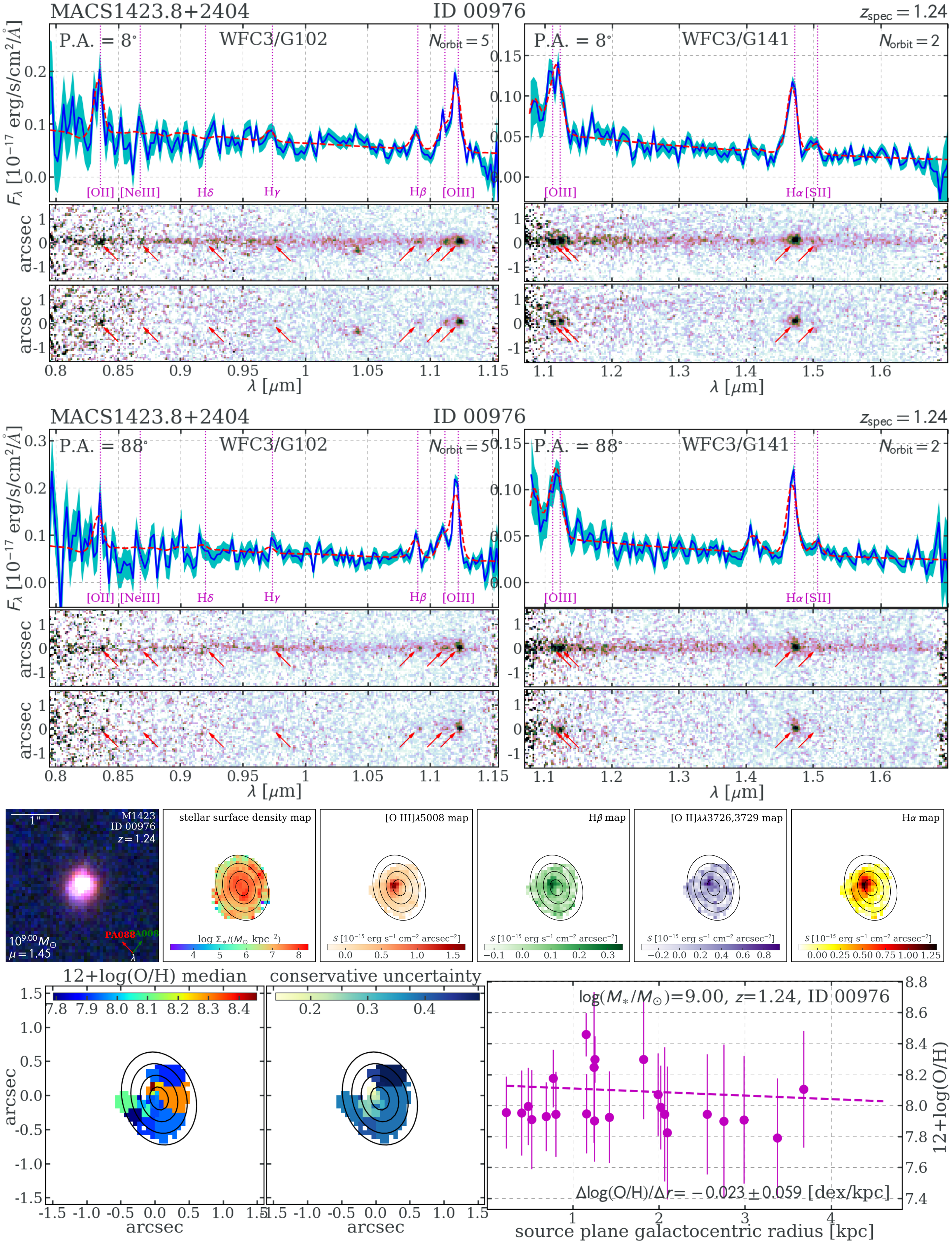

Figure 55. The source ID00976 in the field of MACS1423.8+2404 is shown.

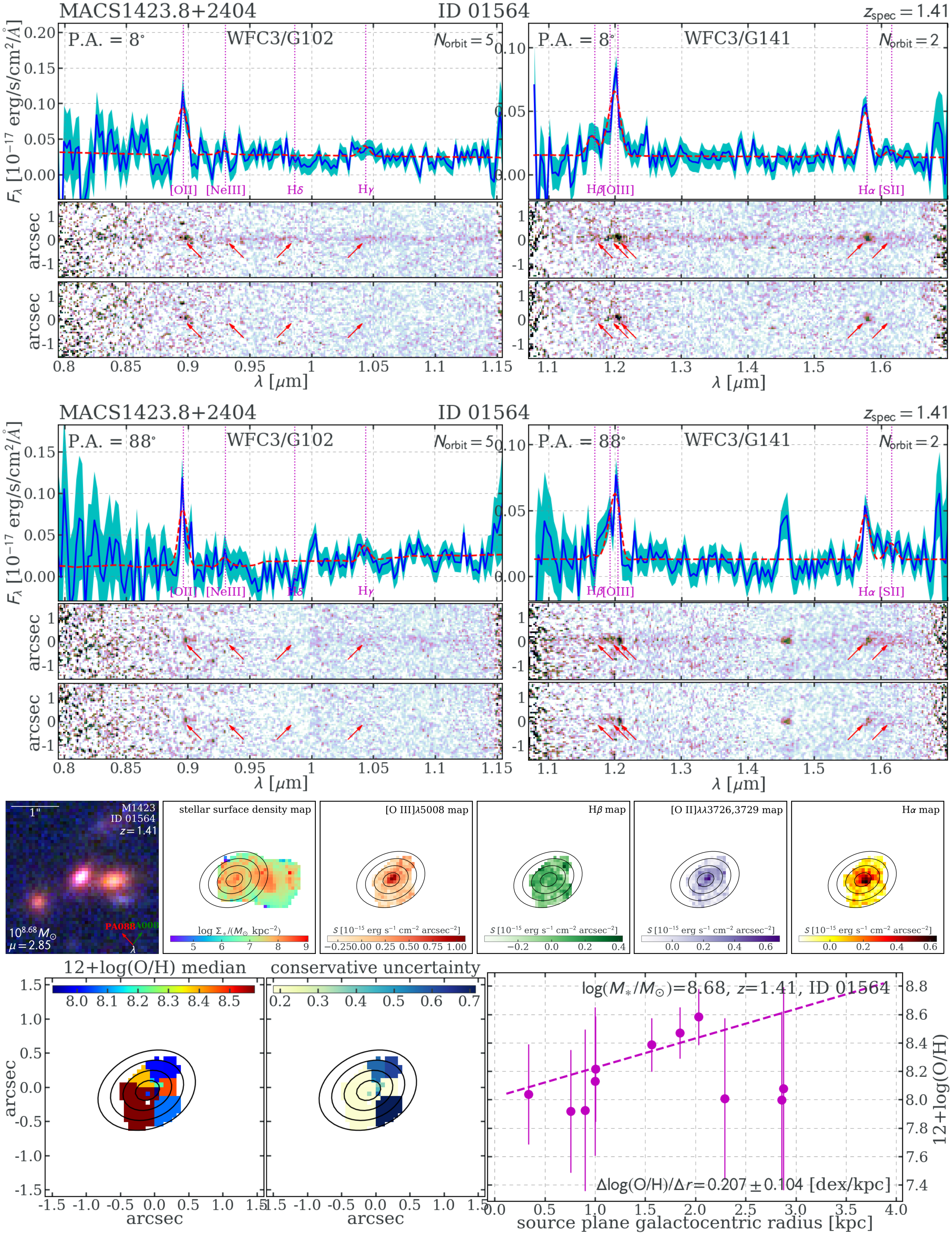

Figure 56. The source ID01564 in the field of MACS1423.8+2404 is shown.

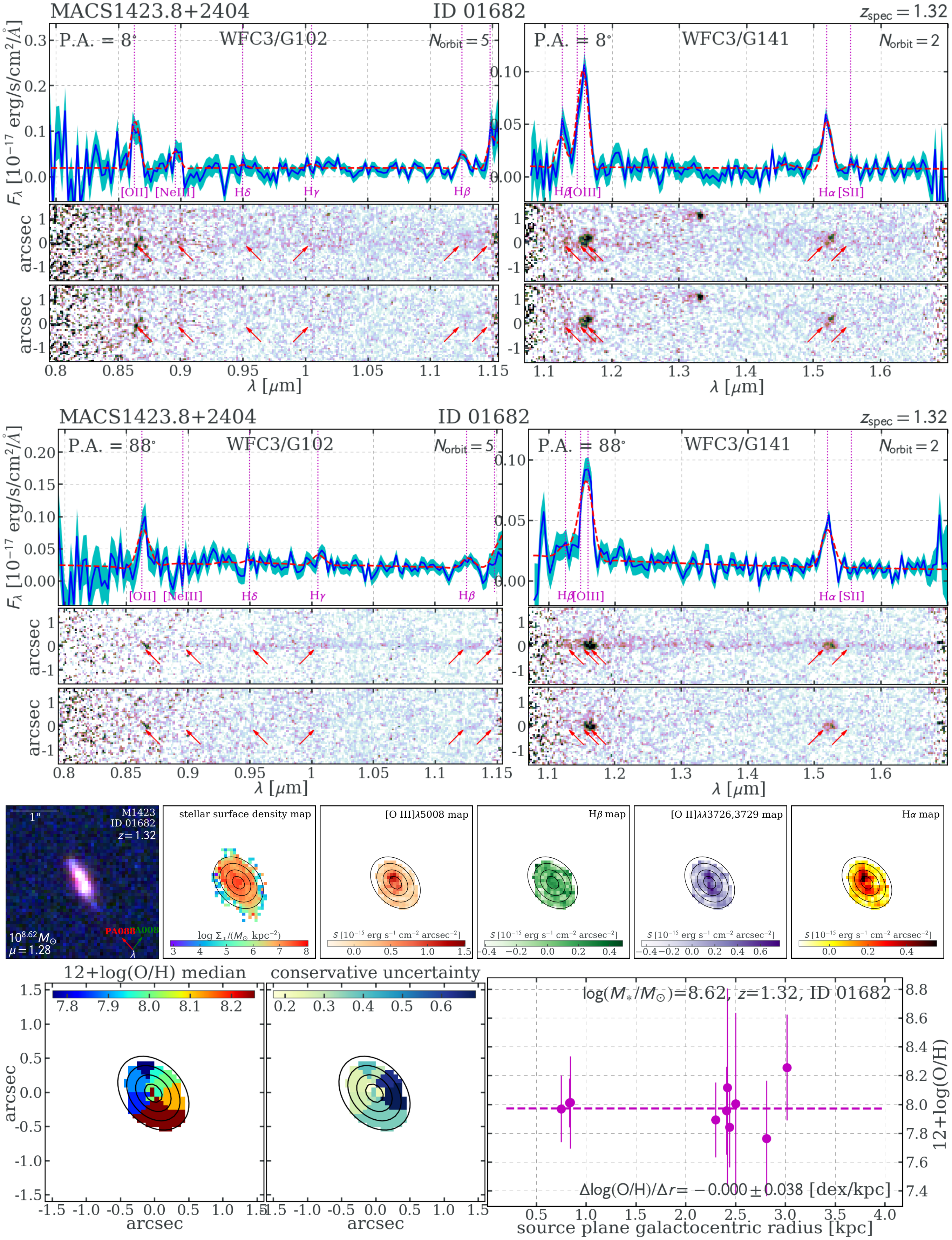

Figure 57. The source ID01682 in the field of MACS1423.8+2404 is shown.

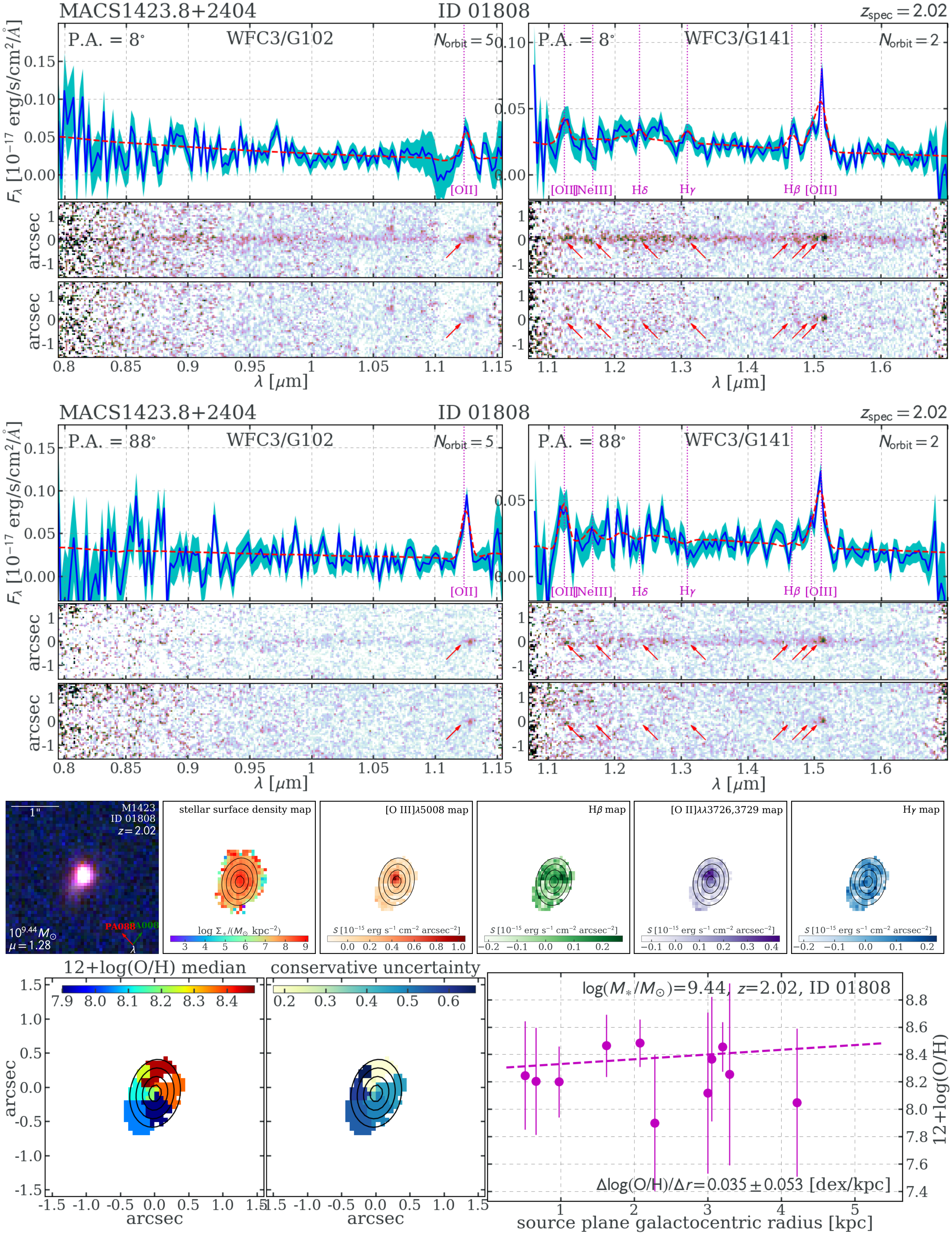

Figure 58. The source ID01808 in the field of MACS1423.8+2404 is shown.

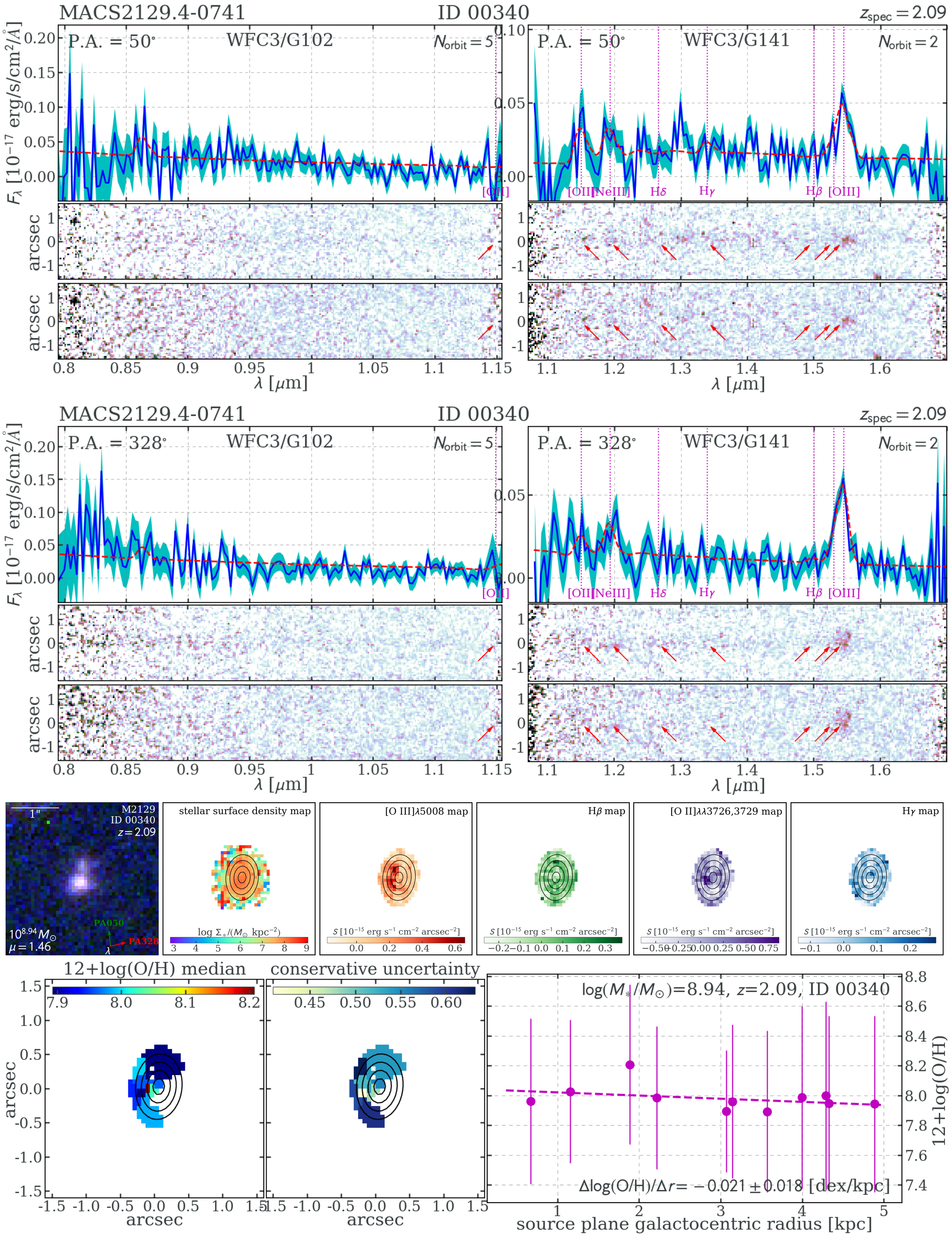

Figure 59. The source ID00340 in the field of MACS2129.4-0741 is shown.

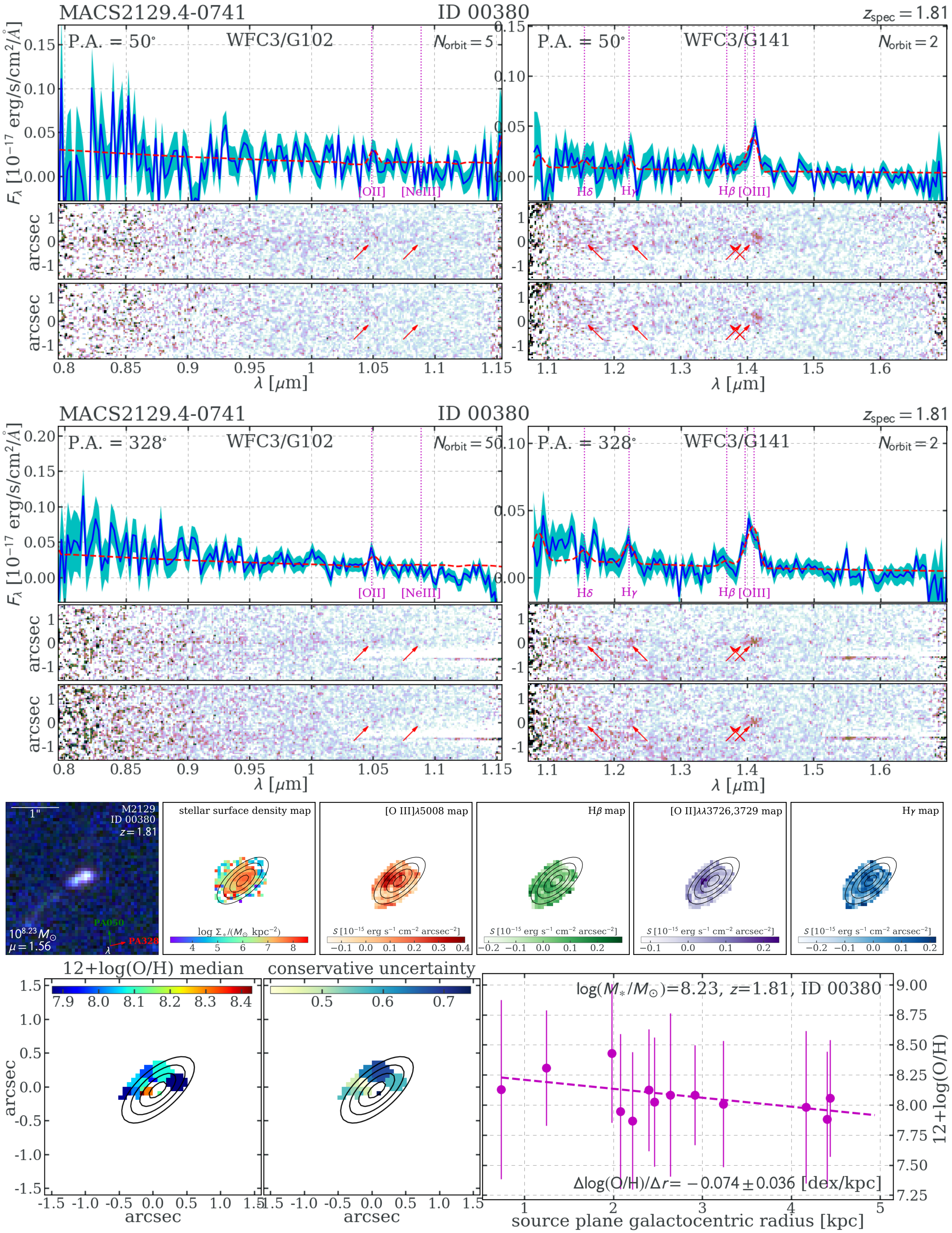

Figure 60. The source ID00380 in the field of MACS2129.4-0741 is shown.

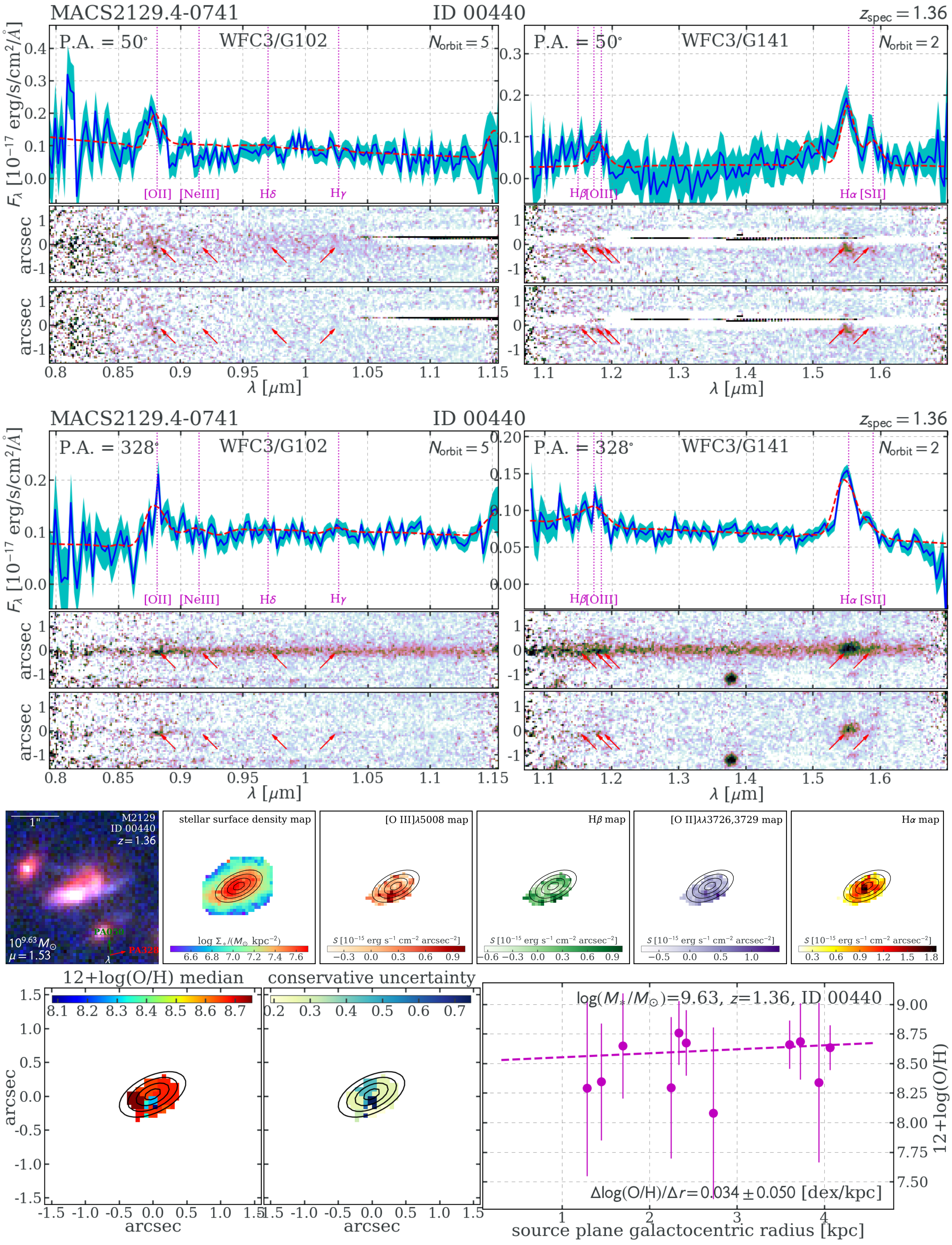

Figure 61. The source ID00440 in the field of MACS2129.4-0741 is shown.

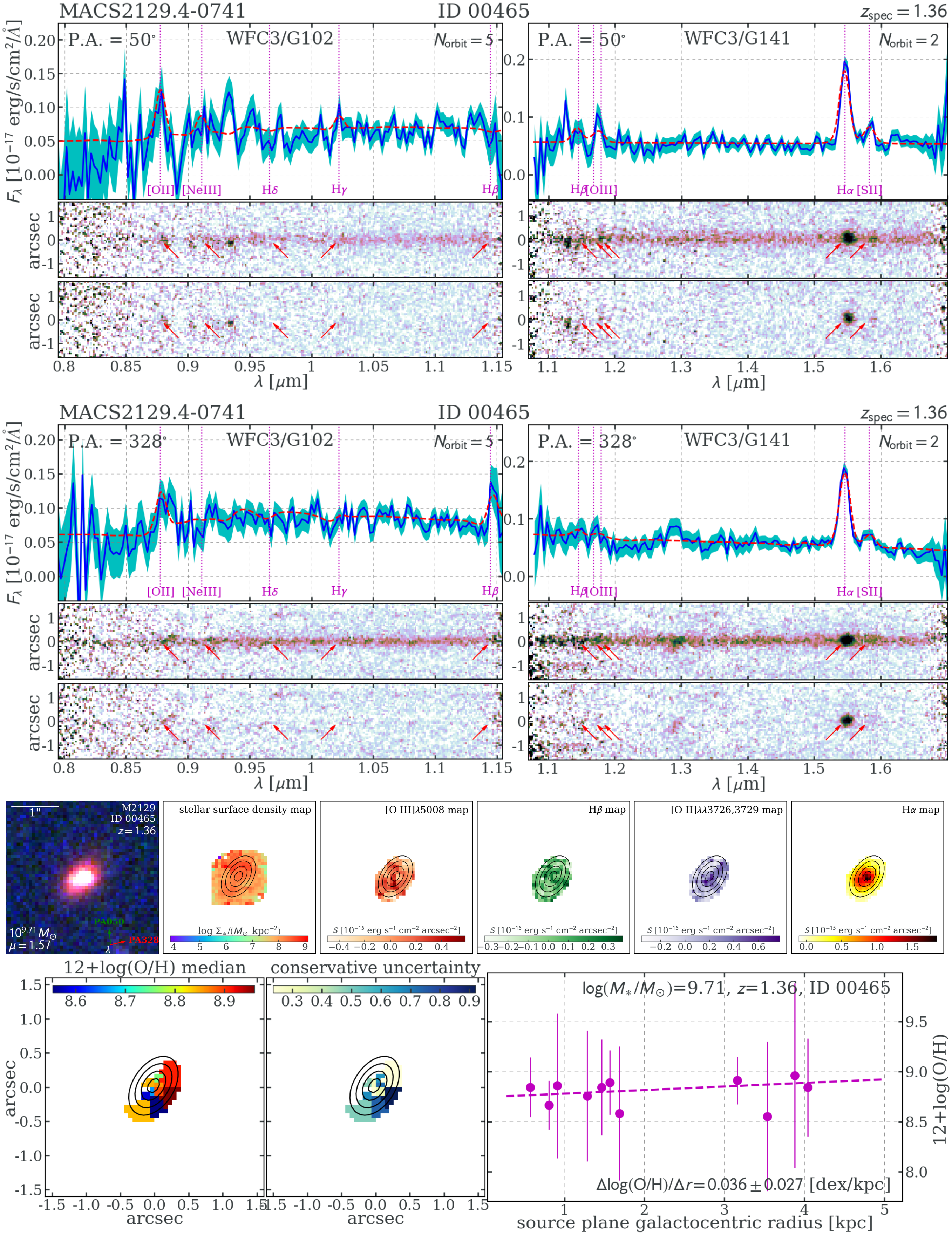

Figure 62. The source ID00465 in the field of MACS2129.4-0741 is shown.

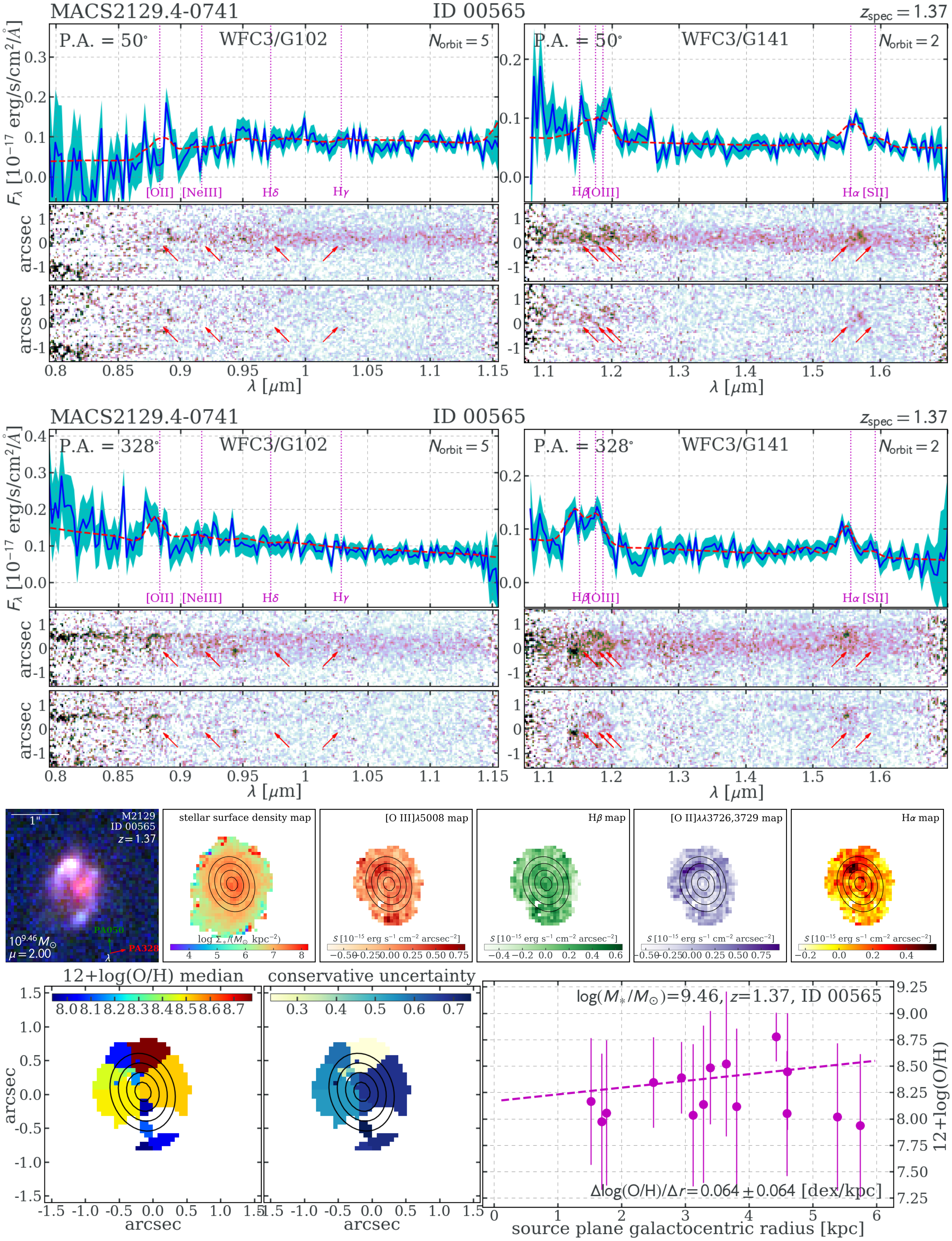

Figure 63. The source ID00565 in the field of MACS2129.4-0741 is shown.

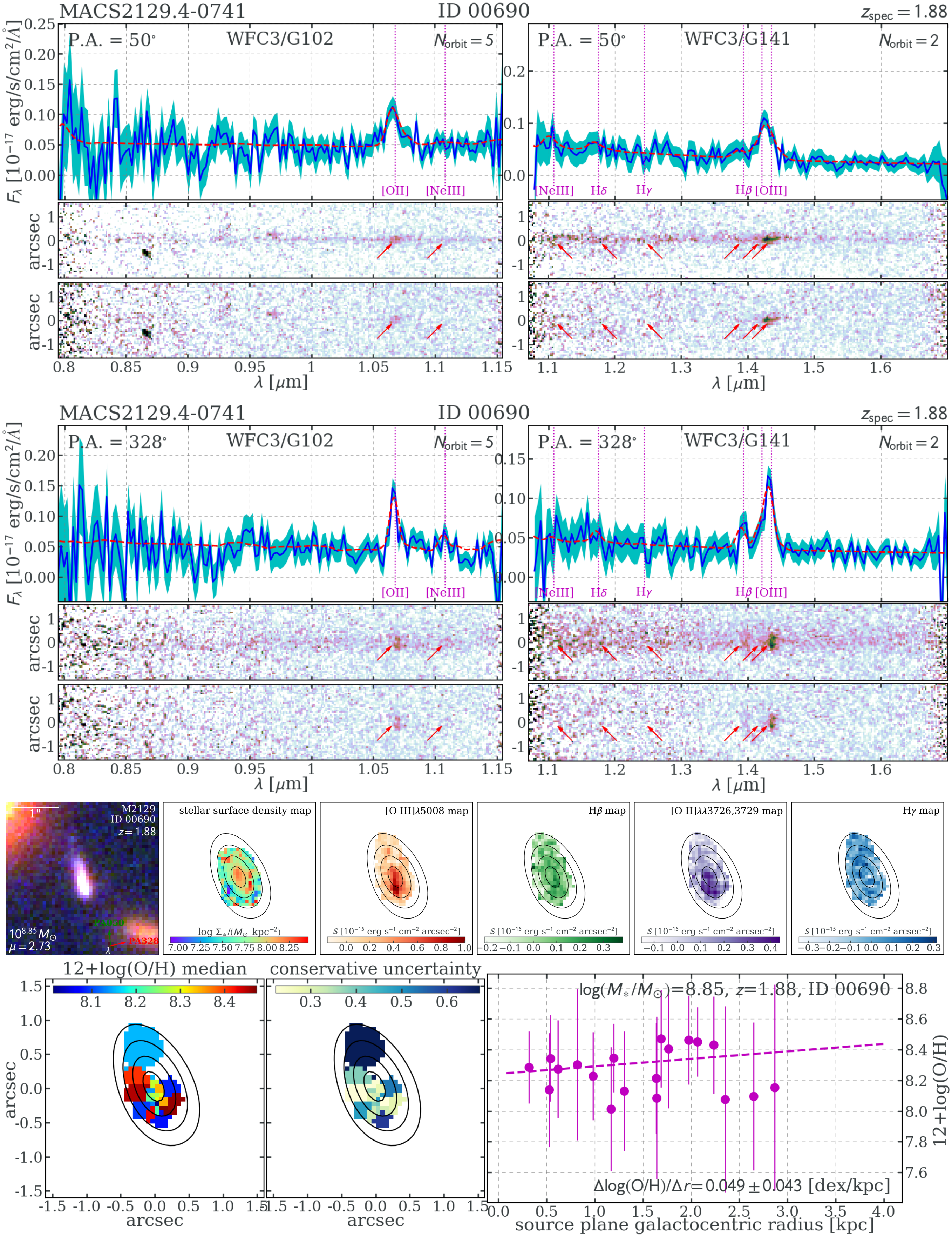

Figure 64. The source ID00690 in the field of MACS2129.4-0741 is shown.

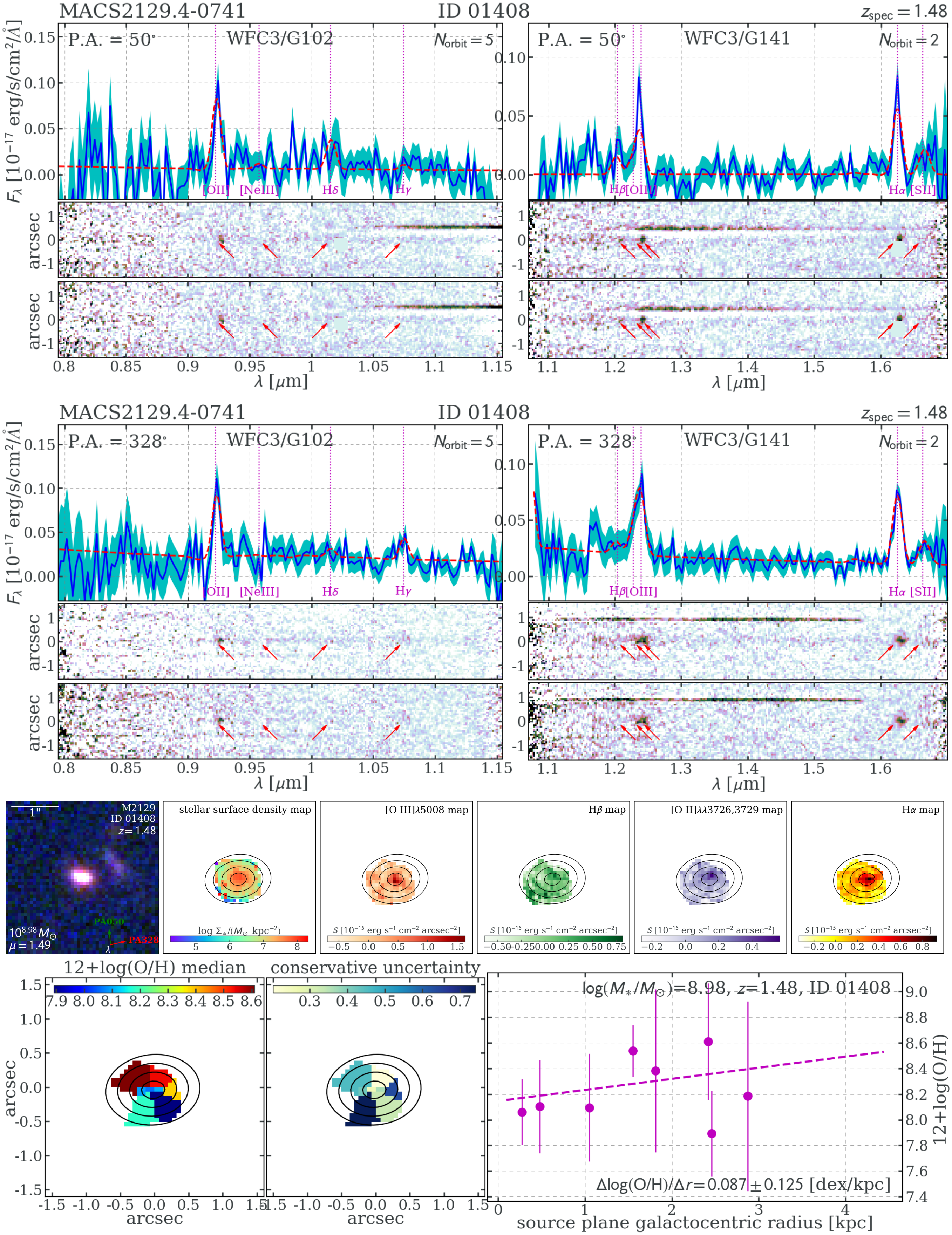

Figure 65. The source ID01408 in the field of MACS2129.4-0741 is shown.

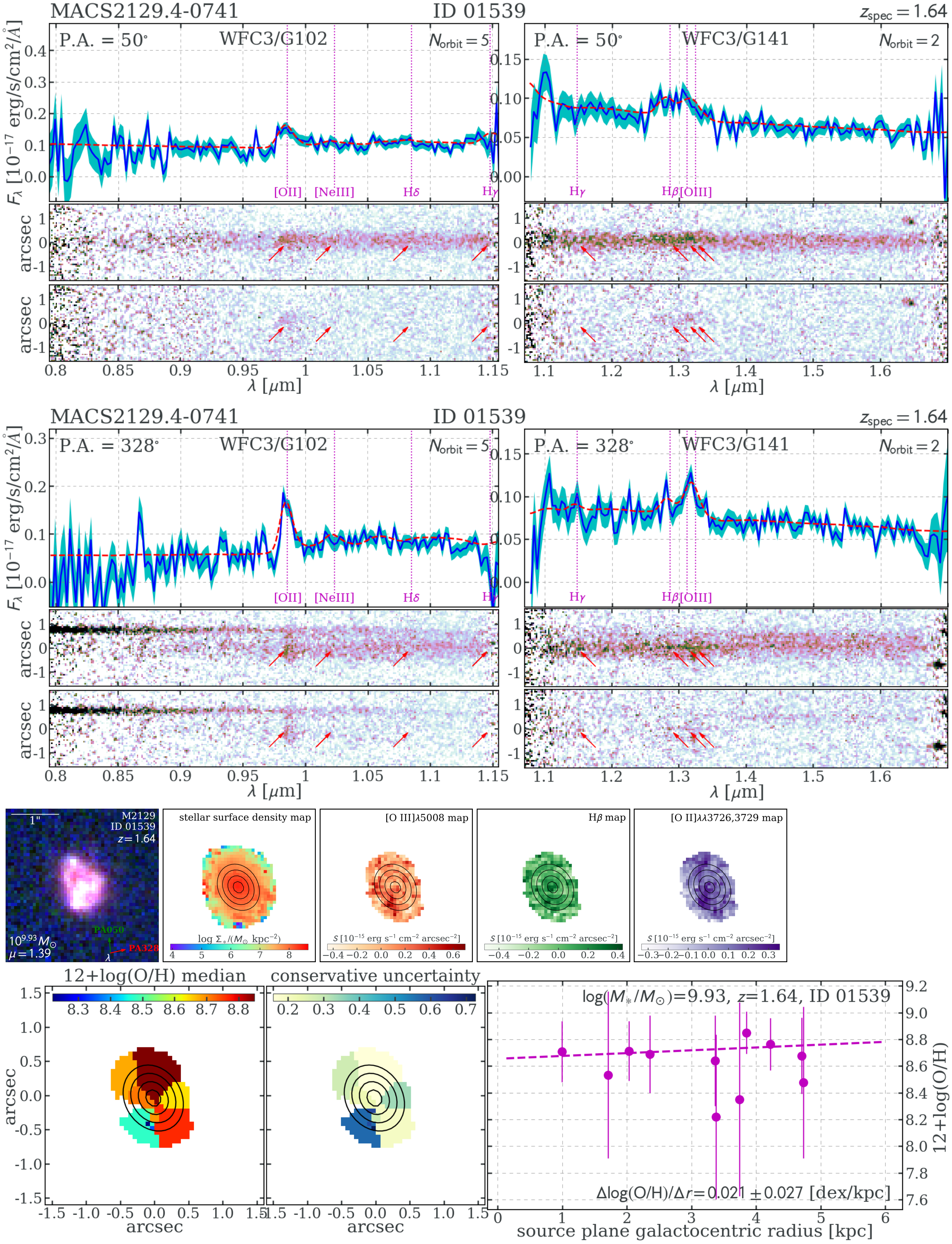

Figure 66. The source ID01539 in the field of MACS2129.4-0741 is shown.

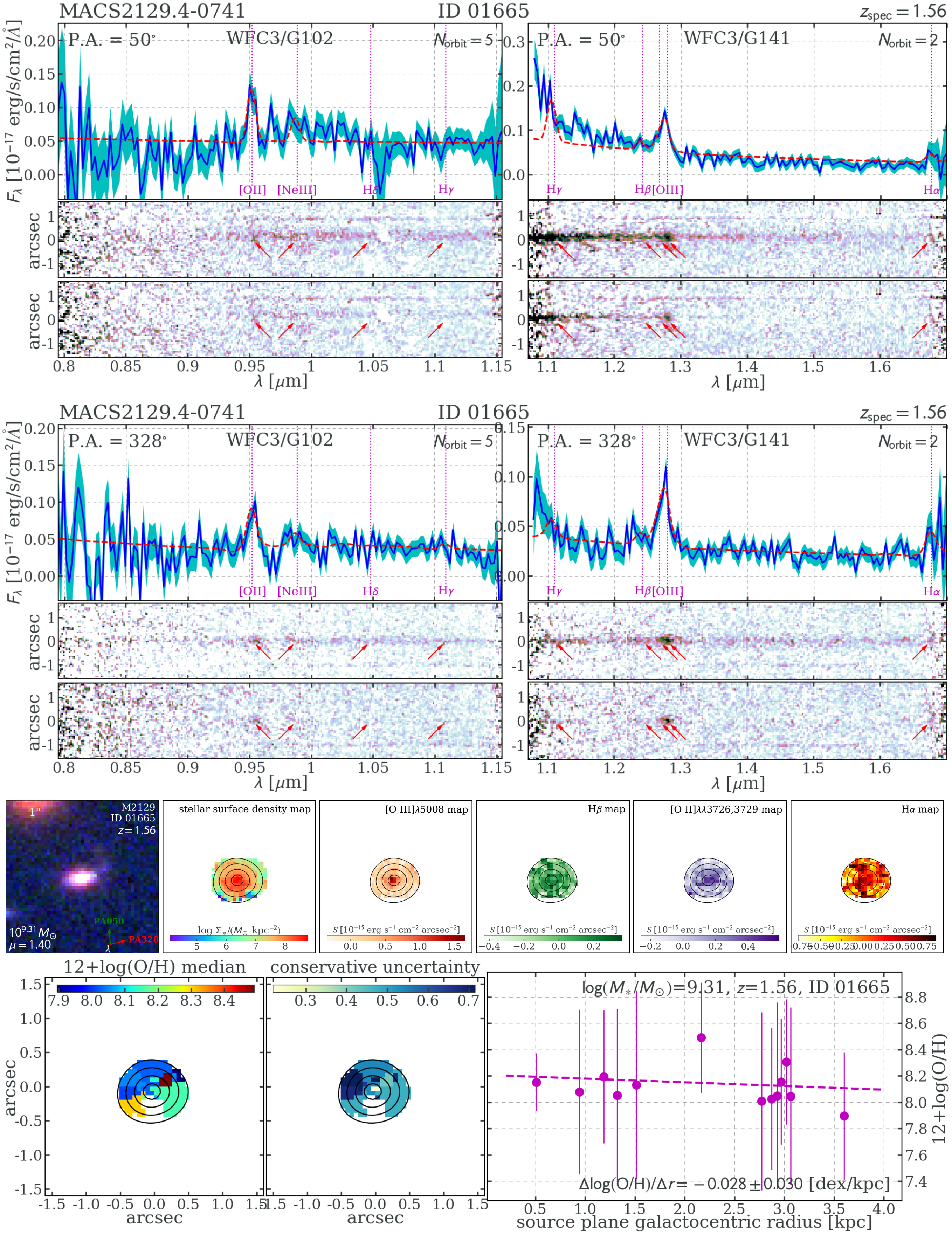

Figure 67. The source ID01665 in the field of MACS2129.4-0741 is shown.

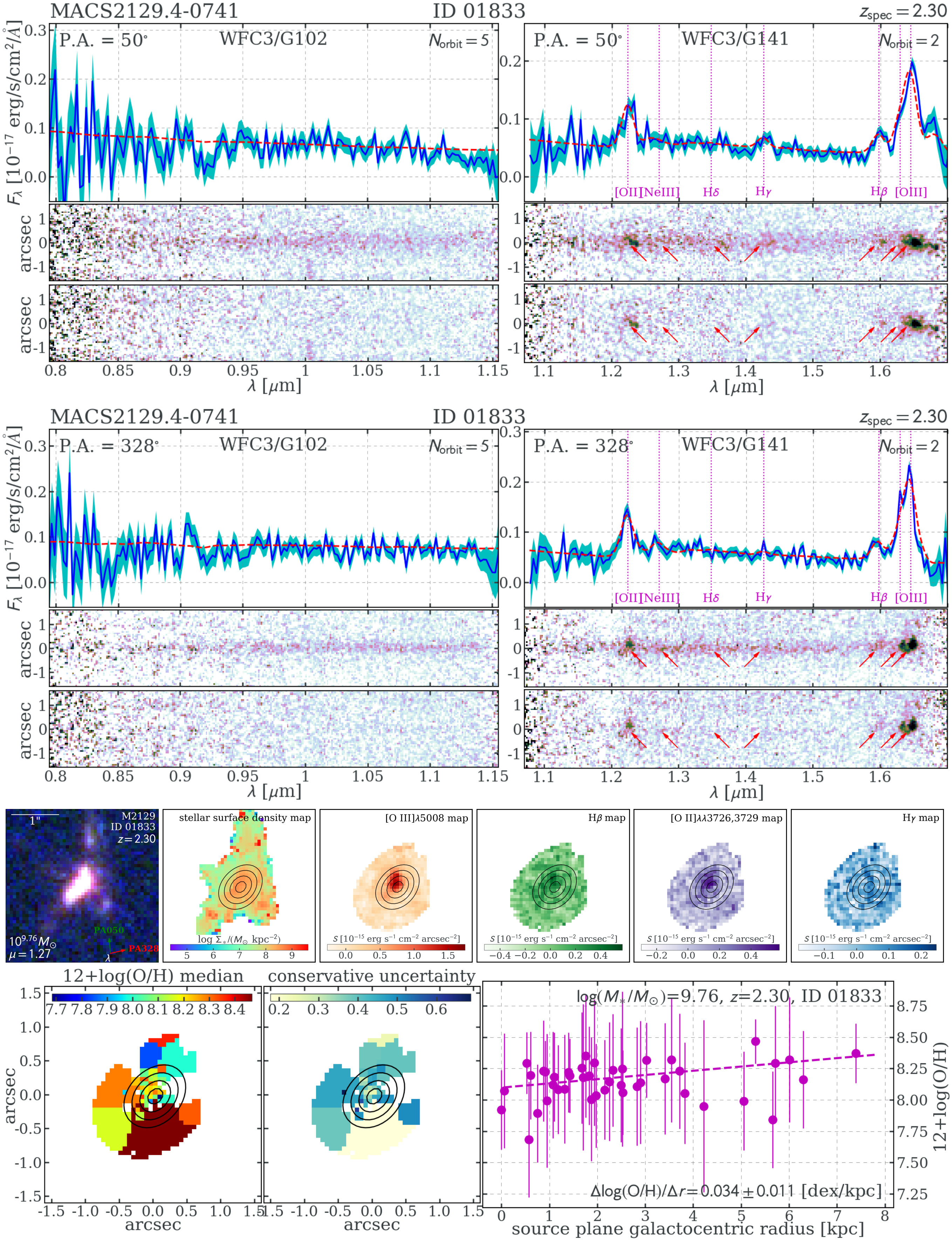

Figure 68. The source ID01833 in the field of MACS2129.4-0741 is shown.

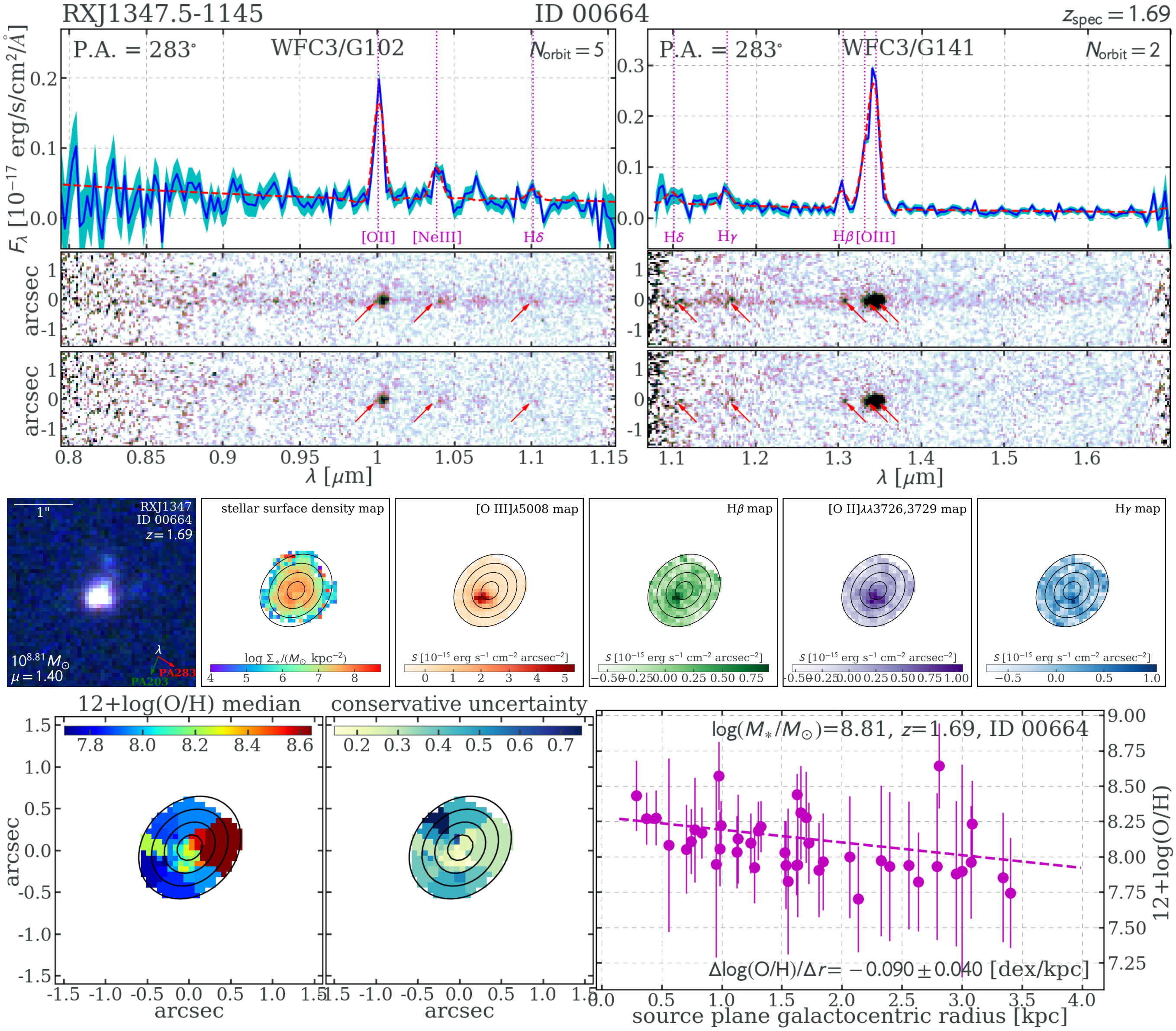

Figure 69. The source ID00664 in the field of RXJ1347.5-1145 is shown.

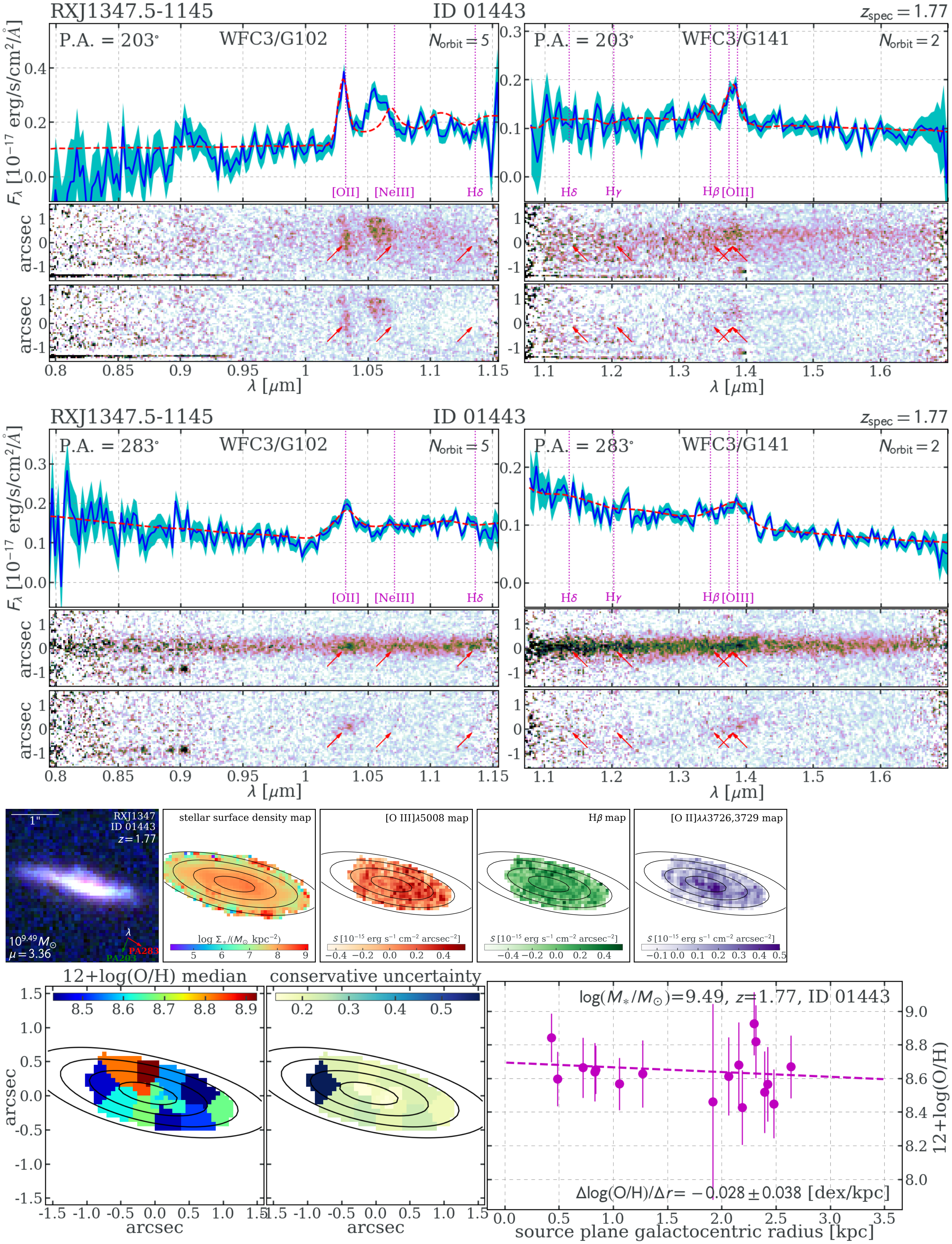

Figure 70. The source ID01443 in the field of RXJ1347.5-1145 is shown.

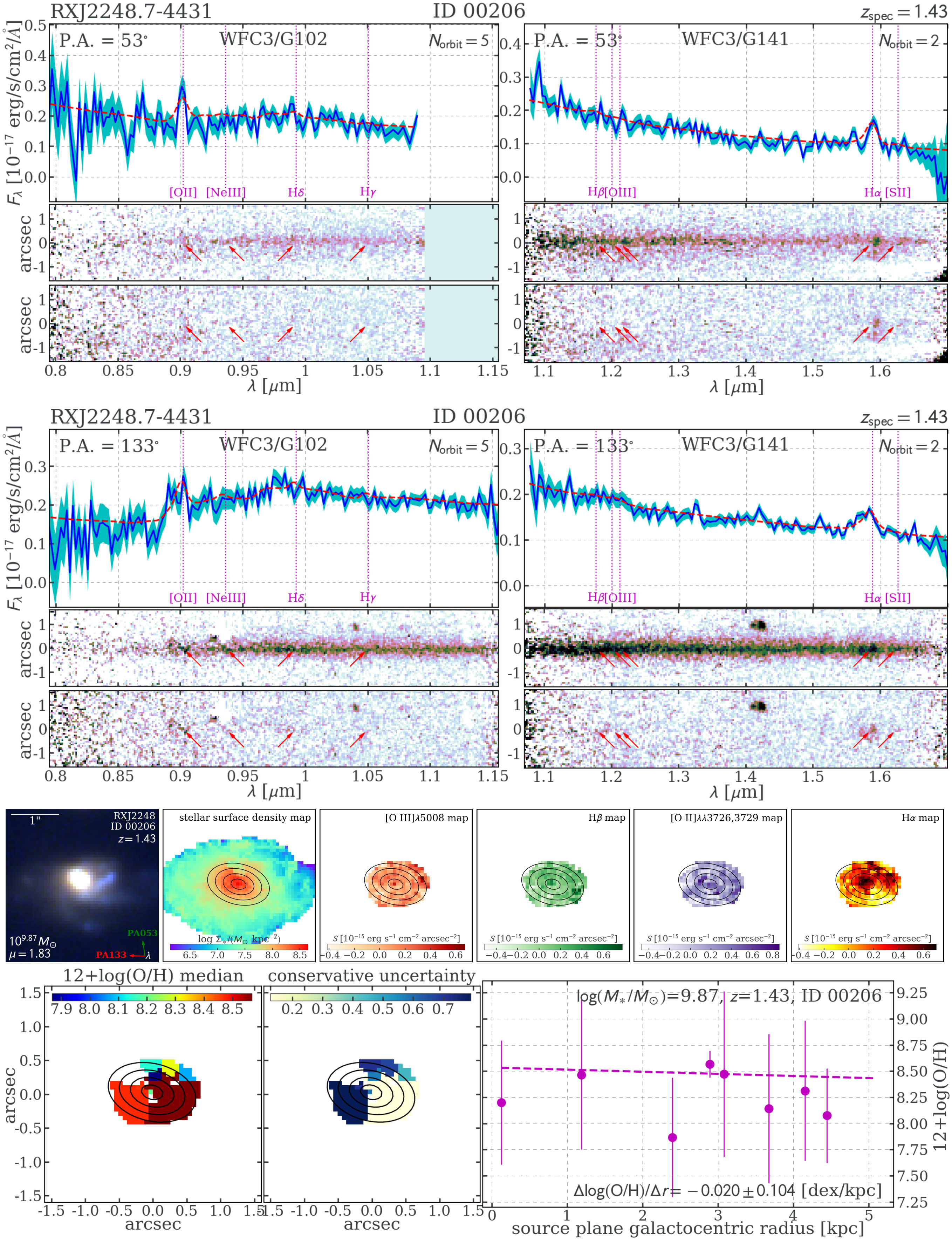

Figure 71. The source ID00206 in the field of RXJ2248.7-4431 is shown.

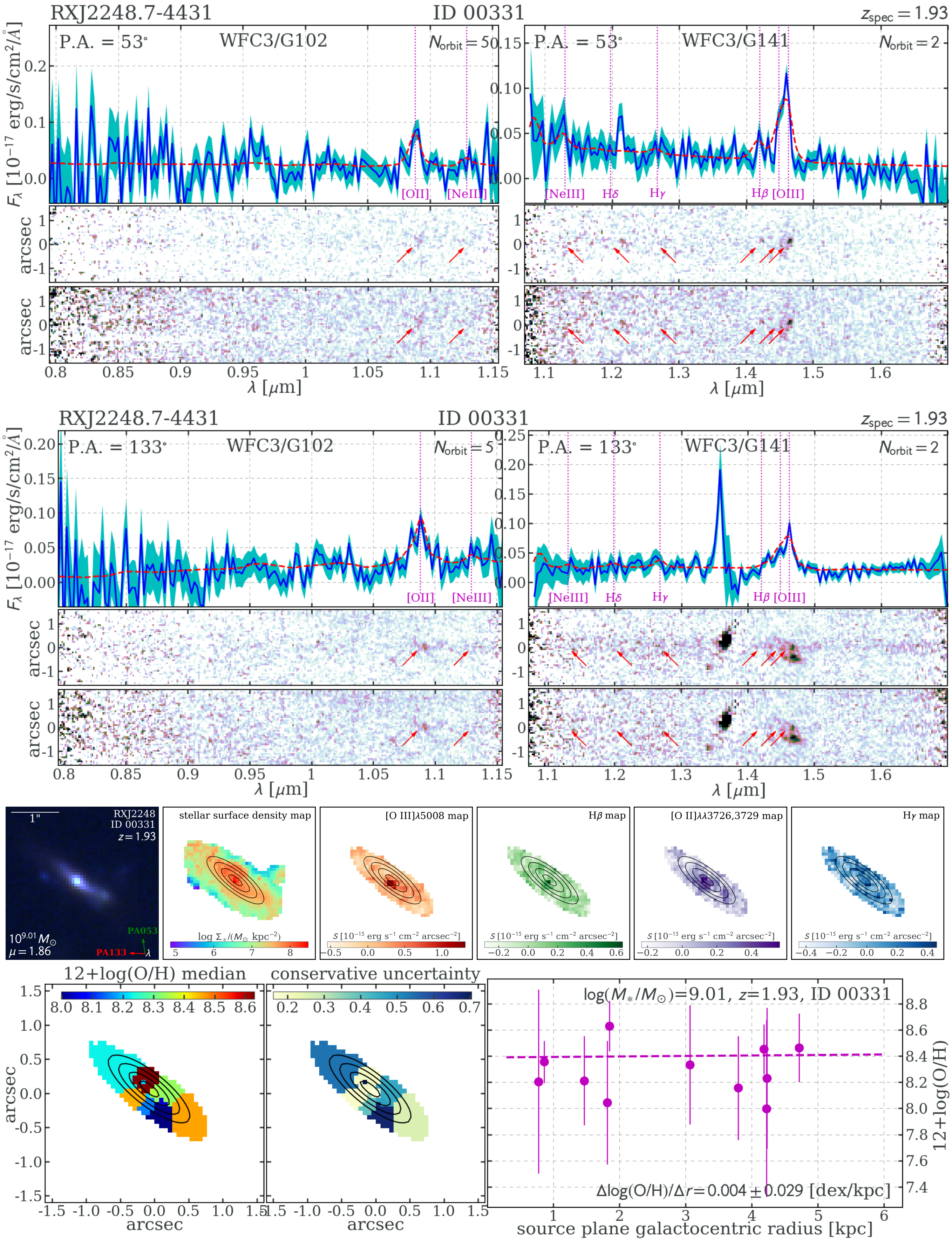

Figure 72. The source ID00331 in the field of RXJ2248.7-4431 is shown.

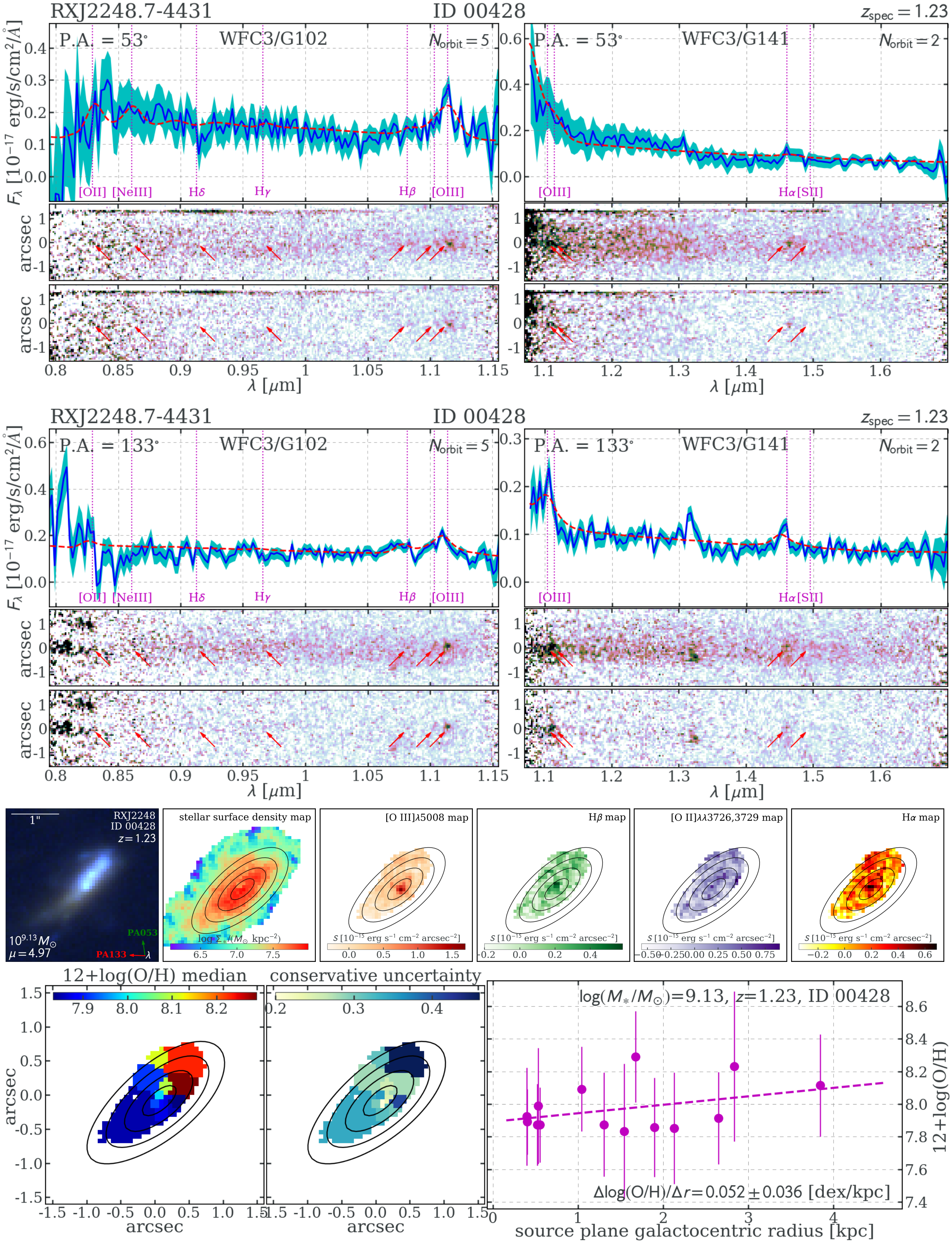

Figure 73. The source ID00428 in the field of RXJ2248.7-4431 is shown.

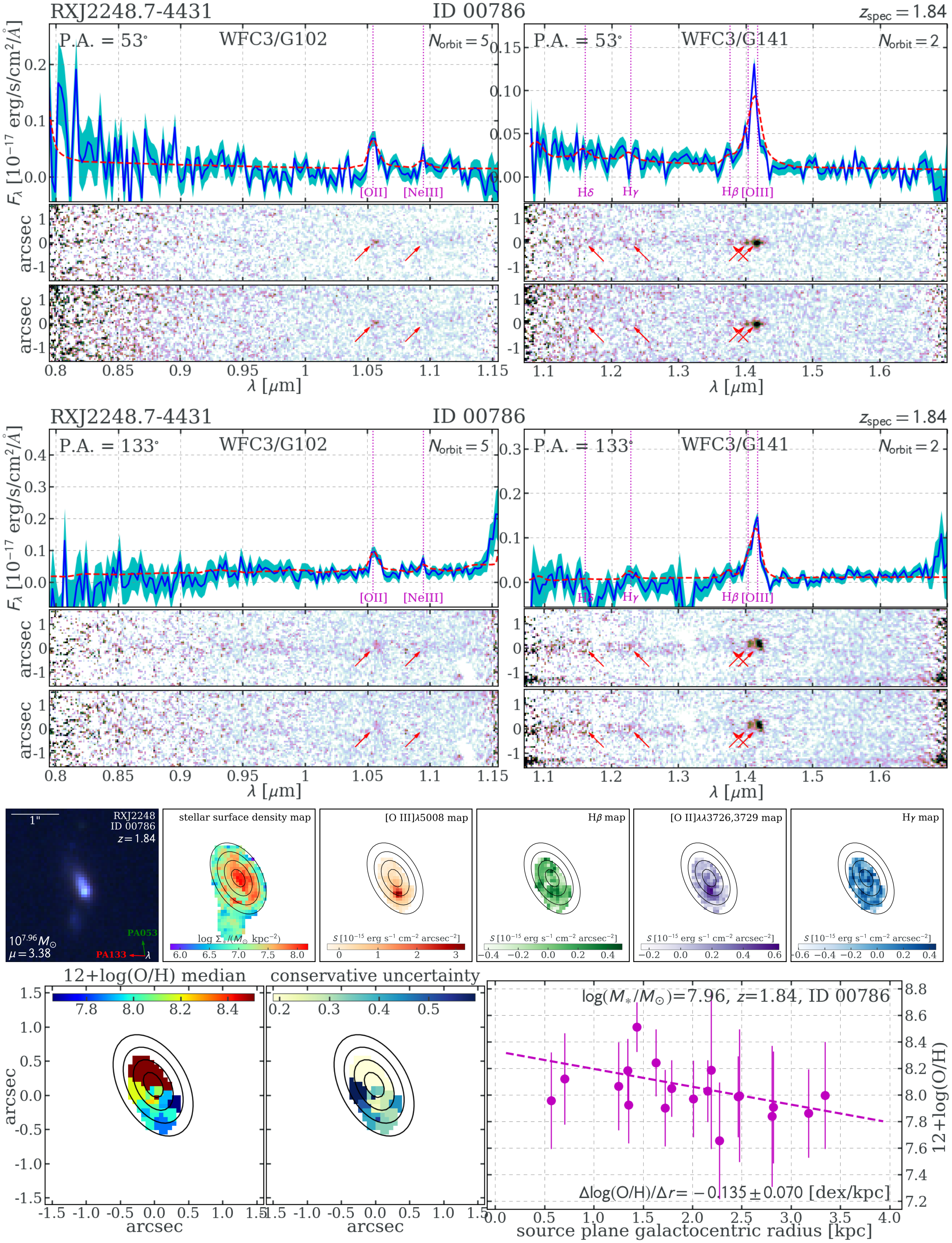

Figure 74. The source ID00786 in the field of RXJ2248.7-4431 is shown.

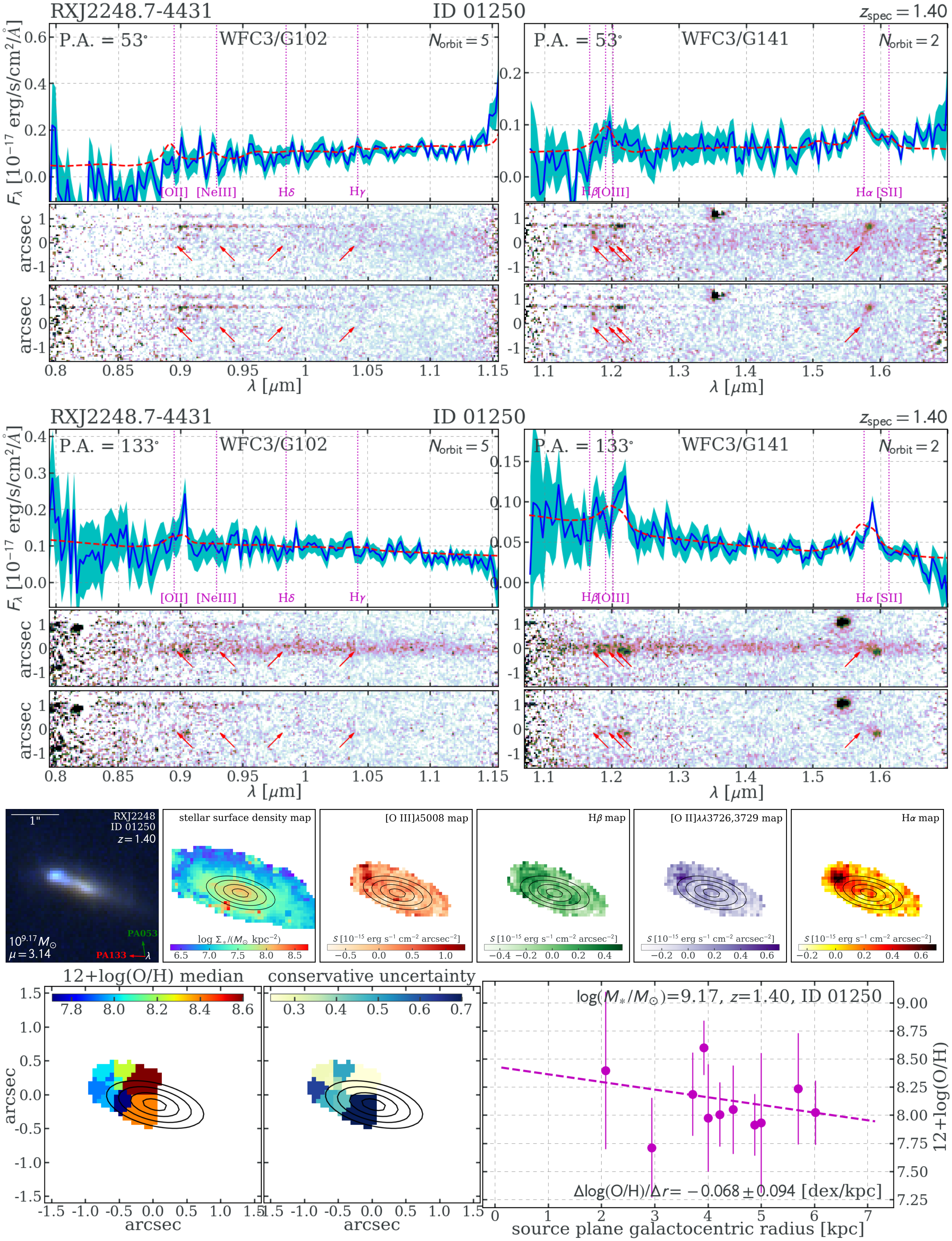

Figure 75. The source ID01250 in the field of RXJ2248.7-4431 is shown.

Table 3. Measured quantities of our sample galaxies.

Cluster	ID	R.A.	Dec.	$z_{\rm spec}$	$\Delta\log({\rm O/H})/\Delta r$	F140W[a]	$r_{\rm F140W}$[b]	Observed integrated EL fluxes [10^{-17}erg s^{-1} cm^{-2}]						μ[c]	Stellar continuum SED fitting			[N II]/Hα[d]	Nebular emission diagnostics		
		[deg.]	[deg.]		[dex/kpc]	[ABmag]		$f_{\rm [OII]}$	$f_{\rm H\gamma}$	$f_{\rm H\beta}$	$f_{\rm [OIII]}$	$f_{\rm H\alpha}$	$f_{\rm [SII]}$		$\log(M_*$[e]$/M_\odot)$	SFR$^{\rm S}$[e] [$M_\odot$/yr]	$A_V^{\rm S}$		12 + log(O/H)	$A_V^{\rm N}$	SFR$^{\rm N}$[e] [$M_\odot$/yr]
A370	01513	39.958904	-1.565269	1.27	−0.230 ± 0.026	21.17	0.95	20.05 ± 2.47	1.36 ± 1.06	8.53 ± 0.80	28.99 ± 0.88	37.55 ± 1.07	5.20 ± 1.10	$2.80^{+0.02}_{-0.03}$	$9.72^{+0.23}_{-0.03}$	$1.30^{+58.61}_{-1.26}$	$0.90^{+0.50}_{-0.38}$	$0.19^{+0.08}_{-0.01}$	$8.36^{+0.10}_{-0.13}$	$1.02^{+0.45}_{-0.42}$	$10.70^{+5.11}_{-3.43}$
A370	01590	39.965663	-1.566864	1.96	0.115 ± 0.056	23.85	0.57	4.61 ± 0.79	4.60 ± 2.74	2.89 ± 2.48	19.48 ± 1.05	···	···	$17.76^{+10.14}_{-7.58}$	$7.48^{+0.32}_{-0.35}$	$0.28^{+0.55}_{-0.18}$	$0.00^{+0.21}_{-0.00}$	$0.04^{+0.00}_{-0.00}$	$8.07^{+0.21}_{-0.35}$	< 1.06	$2.73^{+13.54}_{-2.00}$
A370	02056	39.959425	-1.573309	1.27	0.023 ± 0.009	23.30	0.91	13.75 ± 2.00	4.74 ± 0.92	3.25 ± 0.70	32.83 ± 0.83	10.15 ± 1.14	···	$3.55^{+0.08}_{-0.10}$	$8.50^{+0.10}_{-0.09}$	$5.01^{+2.97}_{-4.27}$	$1.00^{+0.19}_{-0.33}$	$0.05^{+0.01}_{-0.00}$	$7.98^{+0.18}_{-0.20}$	< 0.73	$4.03^{+5.14}_{-1.74}$
A370	02546	39.961942	-1.577895	1.27	0.029 ± 0.108	24.24	0.90	6.56 ± 1.60	0.58 ± 0.72	1.23 ± 0.66	6.98 ± 0.66	3.81 ± 0.68	0.98 ± 0.68	$3.41^{+0.05}_{-0.08}$	$8.25^{+0.13}_{-0.22}$	$0.61^{+0.58}_{-0.52}$	$0.20^{+0.32}_{-0.20}$	$0.05^{+0.00}_{-0.00}$	$8.10^{+0.25}_{-0.35}$	< 0.64	$0.92^{+1.12}_{-0.35}$
A370	03097	39.959500	-1.584013	1.55	−0.016 ± 0.054	22.56	0.94	11.81 ± 0.97	5.65 ± 0.63	4.03 ± 1.31	6.41 ± 1.14	34.27 ± 1.60	···	$2.55^{+0.06}_{-0.08}$	$9.28^{+0.21}_{-0.06}$	$0.73^{+8.55}_{-0.73}$	$0.30^{+0.52}_{-0.30}$	$0.11^{+0.01}_{-0.01}$	$8.78^{+0.09}_{-0.12}$	$1.55^{+0.29}_{-0.30}$	$26.80^{+8.71}_{-6.63}$
A370	03751	39.977361	-1.591636	1.97	0.122 ± 0.008	21.55	0.70	29.57 ± 0.51	7.21 ± 0.67	17.68 ± 0.68	111.41 ± 0.84	···	···	$6.35^{+0.40}_{-0.58}$	$9.05^{+0.05}_{-0.06}$	$32.91^{+3.28}_{-10.50}$	$0.80^{+0.01}_{-0.11}$	$0.07^{+0.00}_{-0.00}$	$8.08^{+0.11}_{-0.12}$	$0.85^{+0.21}_{-0.14}$	$26.23^{+3.19}_{-2.34}$
A370	03834	39.979759	-1.591402	1.25	0.017 ± 0.011	23.56	0.91	2.51 ± 2.71	3.71 ± 0.74	2.56 ± 0.60	15.80 ± 0.79	7.02 ± 0.70	0.78 ± 0.69	$3.18^{+0.11}_{-0.12}$	$8.58^{+0.27}_{-0.08}$	$0.33^{+8.25}_{-0.24}$	$0.90^{+0.60}_{-0.26}$	$0.06^{+0.01}_{-0.01}$	$7.88^{+0.22}_{-0.22}$	< 0.32	$1.43^{+0.77}_{-0.35}$
A2744	00144	3.606322	-30.380061	1.34	0.020 ± 0.085	22.76	0.92	7.45 ± 2.39	2.28 ± 1.12	3.71 ± 3.10	6.38 ± 1.45	14.13 ± 1.17	1.08 ± 1.19	$1.43^{+0.01}_{-0.01}$	$9.56^{+0.17}_{-0.21}$	$15.30^{+22.41}_{-14.67}$	$1.10^{+0.42}_{-0.50}$	$0.15^{+0.04}_{-0.04}$	$8.55^{+0.13}_{-0.22}$	$0.77^{+0.57}_{-0.45}$	$7.66^{+4.52}_{-2.45}$
A2744	00161	3.588863	-30.380291	1.36	0.027 ± 0.063	23.55	0.93	4.50 ± 1.30	1.95 ± 0.65	2.71 ± 1.86	12.51 ± 1.21	6.31 ± 0.70	0.25 ± 0.71	$2.12^{+0.02}_{-0.01}$	$8.53^{+0.18}_{-0.09}$	$2.72^{+5.94}_{-2.41}$	$0.40^{+0.32}_{-0.38}$	$0.05^{+0.01}_{-0.00}$	$8.00^{+0.21}_{-0.25}$	< 0.27	$1.88^{+0.65}_{-0.31}$
A2744	00169	3.571780	-30.380437	1.68	−0.147 ± 0.079	23.83	0.58	4.45 ± 0.59	3.94 ± 1.00	3.07 ± 0.70	18.64 ± 0.74	···	···	$2.76^{+0.02}_{-0.02}$	$8.17^{+0.02}_{-0.05}$	$4.36^{+0.03}_{-1.30}$	$0.40^{+0.01}_{-0.14}$	$0.05^{+0.00}_{-0.00}$	$8.06^{+0.19}_{-0.25}$	< 1.06	< 14.87
A2744	00188	3.573408	-30.380770	1.76	0.033 ± 0.030	21.77	0.95	16.97 ± 0.82	3.00 ± 1.43	5.48 ± 1.02	13.56 ± 1.09	···	···	$2.79^{+0.03}_{-0.02}$	$9.93^{+0.12}_{-0.07}$	$1.39^{+20.38}_{-1.39}$	$0.90^{+0.30}_{-0.34}$	$0.20^{+0.04}_{-0.02}$	$8.55^{+0.09}_{-0.10}$	< 0.68	$12.86^{+16.11}_{-5.74}$
A2744	00263	3.591110	-30.381705	1.89	0.018 ± 0.014	23.02	0.65	6.68 ± 0.55	3.19 ± 0.84	4.14 ± 0.68	34.01 ± 0.75	···	···	$2.21^{+0.02}_{-0.02}$	$8.58^{+0.12}_{-0.01}$	$10.39^{+2.19}_{-4.87}$	$0.20^{+0.10}_{-0.14}$	$0.05^{+0.00}_{-0.00}$	$8.02^{+0.14}_{-0.17}$	$0.90^{+0.88}_{-0.62}$	$21.64^{+34.81}_{-10.71}$
A2744	00892	3.599948	-30.393554	1.34	0.044 ± 0.041	23.21	0.74	14.74 ± 0.98	3.14 ± 0.48	6.97 ± 0.45	37.56 ± 1.01	26.46 ± 0.54	5.58 ± 0.53	$1.90^{+0.02}_{-0.02}$	$8.63^{+0.03}_{-0.04}$	$9.16^{+3.59}_{-3.56}$	$0.90^{+0.10}_{-0.13}$	$0.06^{+0.00}_{-0.00}$	$8.25^{+0.09}_{-0.10}$	$0.39^{+0.31}_{-0.24}$	$8.67^{+2.53}_{-1.60}$
A2744	00893	3.600091	-30.393759	1.34	−0.066 ± 0.085	22.58	0.90	15.59 ± 1.46	1.02 ± 0.75	3.97 ± 0.67	17.64 ± 1.43	17.00 ± 0.79	4.91 ± 0.79	$1.90^{+0.02}_{-0.02}$	$9.24^{+0.15}_{-0.12}$	$25.81^{+17.37}_{-24.47}$	$1.20^{+0.21}_{-0.52}$	$0.10^{+0.02}_{-0.01}$	$8.39^{+0.10}_{-0.12}$	< 0.38	$5.33^{+1.83}_{-1.03}$
A2744	00895	3.576755	-30.393627	1.37	0.139 ± 0.079	22.91	0.87	14.76 ± 1.07	0.05 ± 0.64	6.59 ± 0.91	22.15 ± 1.11	18.12 ± 0.64	2.56 ± 0.64	$3.29^{+0.05}_{-0.04}$	$8.66^{+0.15}_{-0.06}$	$3.11^{+9.15}_{-2.07}$	$0.70^{+0.30}_{-0.26}$	$0.06^{+0.01}_{-0.00}$	$8.29^{+0.09}_{-0.09}$	$1.41^{+0.31}_{-0.29}$	$7.81^{+2.54}_{-1.86}$
A2744	01057	3.575089	-30.399687	1.74	−0.033 ± 0.049	21.88	0.90	10.73 ± 0.79	···	4.28 ± 0.93	26.52 ± 1.05	···	···	$2.64^{+0.03}_{-0.03}$	$9.52^{+0.10}_{-0.15}$	$24.44^{+17.59}_{-22.43}$	$0.50^{+0.29}_{-0.37}$	$0.13^{+0.01}_{-0.02}$	$8.21^{+0.12}_{-0.13}$	< 0.61	$10.51^{+13.74}_{-4.19}$
A2744	01279	3.576955	-30.400863	1.34	−0.051 ± 0.014	23.67	0.83	8.63 ± 1.34	1.23 ± 0.68	5.94 ± 0.60	29.19 ± 1.27	12.51 ± 0.70	1.54 ± 0.69	$2.71^{+0.03}_{-0.04}$	$8.12^{+0.04}_{-0.03}$	$2.80^{+1.12}_{-1.10}$	$0.40^{+0.11}_{-0.17}$	$0.05^{+0.00}_{-0.00}$	$8.00^{+0.13}_{-0.15}$	< 0.22	$2.83^{+0.79}_{-0.44}$
A2744	01649	3.578893	-30.409998	1.26	0.026 ± 0.011	22.67	0.95	8.27 ± 4.96	1.07 ± 1.39	1.67 ± 1.58	23.97 ± 1.50	10.04 ± 1.54	···	$2.46^{+0.02}_{-0.03}$	$9.10^{+0.21}_{-0.17}$	$4.35^{+13.14}_{-4.30}$	$0.60^{+0.52}_{-0.42}$	$0.10^{+0.02}_{-0.02}$	$7.95^{+0.21}_{-0.24}$	$1.33^{+1.02}_{-0.86}$	$8.35^{+15.09}_{-5.01}$
A2744	01773	3.576699	-30.410185	1.66	0.129 ± 0.079	22.95	0.88	8.68 ± 0.72	2.46 ± 1.06	2.74 ± 0.81	10.98 ± 0.85	···	···	$2.00^{+0.02}_{-0.02}$	$9.32^{+0.10}_{-0.19}$	$8.31^{+8.41}_{-8.24}$	$0.50^{+0.33}_{-0.50}$	$0.11^{+0.01}_{-0.02}$	$8.46^{+0.12}_{-0.12}$	< 1.01	$14.68^{+32.79}_{-8.68}$
A2744	01897	3.574584	-30.412278	1.37	−0.159 ± 0.076	22.87	0.90	15.77 ± 1.74	2.18 ± 0.89	2.23 ± 1.10	7.95 ± 1.19	13.62 ± 1.02	3.68 ± 0.98	$1.68^{+0.01}_{-0.01}$	$9.39^{+0.12}_{-0.20}$	$10.56^{+10.17}_{-10.47}$	$0.90^{+0.38}_{-0.44}$	$0.12^{+0.02}_{-0.03}$	$8.56^{+0.09}_{-0.11}$	< 0.51	$5.17^{+2.87}_{-1.39}$
M0416	00094	64.033092	-24.056326	1.36	−0.010 ± 0.126	22.25	0.93	8.52 ± 1.42	1.83 ± 1.04	0.16 ± 0.98	7.33 ± 1.37	17.85 ± 0.85	3.32 ± 0.85	$1.47^{+0.02}_{-0.01}$	$9.72^{+0.08}_{-0.15}$	$10.27^{+15.13}_{-10.06}$	$0.90^{+0.27}_{-0.36}$	$0.18^{+0.02}_{-0.03}$	$8.57^{+0.15}_{-0.14}$	$1.50^{+0.59}_{-0.51}$	$14.78^{+9.31}_{-5.48}$
M0416	00519	64.032451	-24.068482	2.09	−0.037 ± 0.025	21.52	0.89	10.61 ± 1.08	···	4.81 ± 0.94	45.24 ± 1.11	···	···	$4.74^{+11.66}_{-2.63}$	$9.85^{+0.35}_{-0.54}$	$210.95^{+263.50}_{-149.96}$	$1.80^{+0.00}_{-0.00}$	$0.16^{+0.08}_{-0.07}$	$8.03^{+0.10}_{-0.12}$	< 0.65	$11.13^{+44.59}_{-9.16}$
M0416	00572	64.047481	-24.068851	1.90	0.045 ± 0.047	22.94	0.72	9.32 ± 0.78	5.94 ± 4.44	7.47 ± 1.05	26.96 ± 1.13	···	···	$3.31^{+0.09}_{-0.08}$	$8.72^{+0.06}_{-0.03}$	$14.45^{+3.35}_{-2.19}$	$0.80^{+0.10}_{-0.03}$	$0.05^{+0.00}_{-0.00}$	$8.25^{+0.15}_{-0.22}$	< 1.22	$21.50^{+36.41}_{-12.22}$
M0416	00889	64.026197	-24.074377	1.63	0.054 ± 0.038	22.91	0.83	8.79 ± 0.42	2.39 ± 0.37	2.71 ± 0.48	18.55 ± 0.55	···	···	$3.22^{+0.03}_{-0.04}$	$8.72^{+0.09}_{-0.10}$	$7.45^{+2.96}_{-4.23}$	$0.40^{+0.12}_{-0.20}$	$0.06^{+0.00}_{-0.01}$	$8.27^{+0.11}_{-0.12}$	< 0.55	$5.50^{+6.52}_{-2.06}$
M0416	00932	64.018102	-24.075620	2.18	−0.082 ± 0.073	22.16	0.92	13.67 ± 1.33	···	4.87 ± 0.95	17.30 ± 1.08	···	···	$1.86^{+0.02}_{-0.02}$	$10.03^{+0.06}_{-0.15}$	$74.38^{+31.79}_{-72.49}$	$1.10^{+0.16}_{-0.52}$	$0.19^{+0.02}_{-0.03}$	$8.45^{+0.11}_{-0.13}$	< 0.94	$43.12^{+88.65}_{-24.74}$
M0416	00955	64.041852	-24.075813	1.99	−0.079 ± 0.014	23.12	0.36	7.32 ± 0.44	3.52 ± 1.09	6.88 ± 0.60	57.38 ± 0.71	···	···	$2.81^{+0.05}_{-0.05}$	$8.15^{+0.01}_{-0.08}$	$4.18^{+0.08}_{-0.84}$	$0.10^{+0.01}_{-0.10}$	$0.04^{+0.00}_{-0.00}$	$7.95^{+0.12}_{-0.13}$	$1.02^{+0.68}_{-0.66}$	$32.07^{+36.99}_{-16.46}$
M0416	01047	64.021434	-24.078456	2.22	−0.044 ± 0.040	22.88	0.96	4.64 ± 0.89	0.05 ± 0.65	1.80 ± 0.60	14.75 ± 0.72	···	···	$2.85^{+0.05}_{-0.03}$	$9.38^{+0.08}_{-0.11}$	$8.04^{+2.43}_{-1.90}$	$0.20^{+0.14}_{-0.19}$	$0.09^{+0.01}_{-0.01}$	$7.97^{+0.28}_{-0.31}$	$2.29^{+1.59}_{-1.47}$	$55.56^{+242.09}_{-44.42}$
M0416	01197	64.023302	-24.081517	2.23	−0.083 ± 0.027	22.45	0.94	9.61 ± 1.45	3.83 ± 1.08	5.02 ± 1.02	40.99 ± 1.17	···	···	$5.11^{+0.10}_{-0.12}$	$9.17^{+0.04}_{-0.09}$	$0.07^{+38.09}_{-0.00}$	$0.00^{+1.00}_{-0.00}$	$0.08^{+0.00}_{-0.00}$	$7.97^{+0.18}_{-0.20}$	< 1.00	< 27.87
M0416	01213	64.035828	-24.081321	1.63	−0.052 ± 0.048	22.65	0.77	11.39 ± 0.83	2.91 ± 0.91	4.24 ± 0.70	30.81 ± 0.77	···	···	$3.33^{+0.07}_{-0.06}$	$8.74^{+0.08}_{-0.01}$	$1.28^{+0.02}_{-0.75}$	$0.10^{+0.07}_{-0.10}$	$0.06^{+0.00}_{-0.00}$	$8.17^{+0.12}_{-0.13}$	< 0.55	$7.08^{+8.81}_{-2.67}$
M0717	01007	109.388805	37.752159	1.85	−0.065 ± 0.034	22.23	0.84	8.01 ± 1.20	16.05 ± 2.03	3.81 ± 1.68	32.95 ± 1.70	···	···	$6.96^{+0.62}_{-0.55}$	$9.00^{+0.11}_{-0.11}$	$29.32^{+2.49}_{-12.33}$	$1.30^{+0.02}_{-0.18}$	$0.07^{+0.01}_{-0.01}$	$7.96^{+0.21}_{-0.24}$	< 1.21	$7.27^{+13.98}_{-4.10}$
M0717	01131	109.381097	37.750440	1.85	−0.055 ± 0.028	22.07	0.75	27.83 ± 0.95	···	12.00 ± 1.43	53.78 ± 1.30	···	···	$7.86^{+1.04}_{-0.96}$	$8.95^{+0.19}_{-0.15}$	$6.23^{+17.82}_{-5.45}$	$0.90^{+0.24}_{-0.30}$	$0.07^{+0.02}_{-0.01}$	$8.30^{+0.10}_{-0.11}$	< 0.53	$9.07^{+11.67}_{-3.87}$
M0717	01636	109.376338	37.744601	1.85	−0.059 ± 0.040	22.97	0.78	12.42 ± 0.57	1.12 ± 0.90	3.41 ± 0.71	22.03 ± 0.78	···	···	$3.52^{+0.13}_{-0.09}$	$9.04^{+0.11}_{-0.18}$	$13.91^{+10.92}_{-13.08}$	$1.00^{+0.21}_{-0.42}$	$0.08^{+0.01}_{-0.02}$	$8.30^{+0.10}_{-0.11}$	< 0.47	$7.29^{+8.48}_{-2.58}$
M0717	02043	109.394456	37.739171	1.86	−0.200 ± 0.076	24.49	0.21	0.07 ± 0.59	1.16 ± 1.26	3.57 ± 0.93	19.27 ± 0.81	···	···	$14.96^{+1.25}_{-1.33}$	$6.93^{+0.04}_{-0.03}$	$0.25^{+0.02}_{-0.02}$	$0.00^{+0.00}_{-0.00}$	$0.05^{+0.00}_{-0.00}$	$7.70^{+0.29}_{-0.24}$	$2.94^{+1.63}_{-1.79}$	$17.16^{+88.69}_{-14.80}$
M0717	02064	109.413018	37.738458	2.08	0.044 ± 0.047	23.42	0.64	15.24 ± 1.29	···	3.92 ± 1.18	24.27 ± 1.20	···	···	$5.69^{+0.42}_{-0.39}$	$8.23^{+0.15}_{-0.05}$	$4.73^{+0.46}_{-3.37}$	$0.60^{+0.07}_{-0.20}$	$0.04^{+0.00}_{-0.00}$	$8.31^{+0.10}_{-0.11}$	< 0.49	$6.92^{+8.50}_{-2.65}$
M0744	00920	116.212401	39.460342	1.28	−0.194 ± 0.077	20.81	0.95	13.04 ± 6.32	0.01 ± 1.30	6.74 ± 1.76	41.30 ± 1.25	42.86 ± 1.22	9.02 ± 1.21	$10.83^{+1.01}_{-0.76}$	$9.33^{+0.15}_{-0.06}$	$3.20^{+6.28}_{-1.83}$	$0.80^{+0.27}_{-0.21}$	$0.11^{+0.03}_{-0.01}$	$7.99^{+0.22}_{-0.28}$	$1.75^{+0.79}_{-0.86}$	$5.76^{+7.20}_{-3.50}$
M0744	01031	116.212064	39.459430	1.27	0.178 ± 0.242	20.94	0.93	24.57 ± 2.77	6.57 ± 1.25	20.09 ± 0.93	36.40 ± 1.09	48.45 ± 1.15	17.99 ± 1.13	$6.31^{+0.36}_{-0.31}$	$9.58^{+0.15}_{-0.10}$	$4.79^{+9.09}_{-1.80}$	$0.70^{+0.32}_{-0.11}$	$0.16^{+0.03}_{-0.02}$	$8.52^{+0.11}_{-0.13}$	$1.63^{+0.78}_{-0.97}$	$22.33^{+32.02}_{-14.78}$
M0744	01203	116.197585	39.456699	1.65	0.111 ± 0.017	21.68	0.64	34.00 ± 0.96	7.06 ± 1.00	17.46 ± 1.06	117.66 ± 1.17	···	···	$2.25^{+0.03}_{-0.03}$	$9.41^{+0.01}_{-0.01}$	$75.31^{+1.04}_{-1.11}$	$1.00^{+0.00}_{-0.00}$	$0.12^{+0.00}_{-0.00}$	$8.10^{+0.10}_{-0.12}$	$0.89^{+0.28}_{-0.20}$	$47.74^{+5.28}_{-3.06}$
M0744	01370	116.236950	39.454058	1.37	−0.116 ± 0.111	22.71	0.94	5.59 ± 1.52	···	2.22 ± 1.18	12.37 ± 1.39	10.19 ± 0.81	2.38 ± 0.80	$1.55^{+0.01}_{-0.02}$	$9.56^{+0.16}_{-0.06}$	$3.71^{+17.90}_{-3.69}$	$1.10^{+0.34}_{-0.32}$	$0.15^{+0.03}_{-0.01}$	$8.29^{+0.13}_{-0.17}$	$0.54^{+0.54}_{-0.37}$	$4.57^{+2.63}_{-1.24}$
M0744	01734	116.219106	39.449158	1.49	0.085 ± 0.034	22.62	0.77	16.67 ± 1.45	3.16 ± 0.92	7.48 ± 1.86	30.72 ± 1.53	19.46 ± 1.08	10.71 ± 2.31	$1.63^{+0.02}_{-0.01}$	$9.17^{+0.14}_{-0.01}$	$43.51^{+0.30}_{-43.43}$	$1.10^{+0.05}_{-1.00}$	$0.09^{+0.02}_{-0.00}$	$8.25^{+0.09}_{-0.11}$	< 0.17	$8.97^{+2.11}_{-1.31}$
M0744	02341	116.212719	39.441062	1.28	0.031 ± 0.044	22.60	0.93	4.92 ± 1.55	0.69 ± 0.68	3.38 ± 0.78	11.49 ± 0.71	10.74 ± 0.65	3.20 ± 0.63	$1.13^{+0.00}_{-0.00}$	$9.47^{+0.11}_{-0.07}$	$3.01^{+19.34}_{-2.88}$	$0.50^{+0.42}_{-0.30}$	$0.14^{+0.02}_{-0.01}$	$8.27^{+0.14}_{-0.25}$	$0.63^{+0.55}_{-0.41}$	$6.17^{+3.65}_{-1.86}$
M1423	00410	215.941735	24.088841	1.79	0.104 ± 0.054	23.19	0.77	7.50 ± 0.47	3.10 ± 0.71	3.08 ± 0.54	18.78 ± 0.64	···	···	$1.46^{+0.02}_{-0.01}$	$9.03^{+0.11}_{-0.07}$	$20.72^{+6.12}_{-18.14}$	$0.60^{+0.11}_{-0.33}$	$0.08^{+0.01}_{-0.01}$	$8.24^{+0.12}_{-0.14}$	< 0.59	$15.47^{+25.95}_{-6.11}$
M1423	00433	215.954478	24.088107	1.63	−0.095 ± 0.046	23.00	0.80	7.83 ± 0.85	0.47 ± 0.61	4.28 ± 1.70	18.45 ± 1.03	···	···	$3.64^{+0.06}_{-0.13}$	$8.94^{+0.15}_{-0.16}$	$10.22^{+8.63}_{-10.03}$	$1.00^{+0.28}_{-0.63}$	$0.08^{+0.01}_{-0.01}$	$8.27^{+0.15}_{-0.21}$	< 1.03	$8.97^{+20.72}_{-5.32}$

Table 3 *continued*

Table 3 *(continued)*

Cluster	ID	R.A. [deg.]	Dec. [deg.]	$z_{\rm spec}$	$\Delta\log({\rm O/H})/\Delta r$ [dex/kpc]	F140W[a] [ABmag]	$r_{\rm F140W}$[b]	Observed integrated EL fluxes [10^{-17}erg s^{-1} cm^{-2}]						μ[c]	Stellar continuum SED fitting			[N II]/Hα[d]	Nebular emission diagnostics		
								$f_{\rm [OII]}$	$f_{\rm H\gamma}$	$f_{\rm H\beta}$	$f_{\rm [OIII]}$	$f_{\rm H\alpha}$	$f_{\rm [SII]}$		$\log(M_*$[e]$/M_\odot)$	SFR$^{\rm S}$[e] [$M_\odot$/yr]	$A_{\rm V}^{\rm S}$		12 + log(O/H)	$A_{\rm V}^{\rm N}$	SFR$^{\rm N}$[e] [$M_\odot$/yr]
M1423	00493	215.952044	24.083337	1.78	−0.028 ± 0.089	21.75	0.93	13.40 ± 2.17	3.05 ± 3.47	19.79 ± 2.00	18.92 ± 2.61	···	···	$5.14^{+0.42}_{-0.20}$	$9.66^{+0.24}_{-0.24}$	$6.60^{+9.50}_{-6.60}$	$0.60^{+0.40}_{-0.44}$	$0.14^{+0.05}_{-0.03}$	$8.52^{+0.13}_{-0.15}$	$1.67^{+0.39}_{-0.80}$	> 26.26
M1423	00908	215.957460	24.079767	1.31	−0.233 ± 0.104	21.91	0.96	12.88 ± 4.10	···	4.07 ± 2.50	8.01 ± 3.07	17.25 ± 1.47	···	$2.12^{+0.03}_{-0.01}$	$9.54^{+0.34}_{-0.12}$	$12.11^{+78.23}_{-11.30}$	$1.20^{+0.51}_{-0.70}$	$0.15^{+0.09}_{-0.02}$	$8.60^{+0.17}_{-0.20}$	$0.75^{+0.75}_{-0.49}$	$5.81^{+4.91}_{-2.14}$
M1423	00909	215.957063	24.079622	1.32	−0.260 ± 0.085	23.08	0.86	16.21 ± 1.76	3.73 ± 0.82	3.47 ± 1.24	12.18 ± 1.48	14.55 ± 0.78	4.38 ± 0.78	$2.21^{+0.04}_{-0.02}$	$8.72^{+0.15}_{-0.12}$	$6.09^{+6.44}_{-5.65}$	$0.60^{+0.26}_{-0.43}$	$0.06^{+0.01}_{-0.01}$	$8.51^{+0.08}_{-0.09}$	< 0.28	$3.66^{+1.09}_{-0.64}$
M1423	00976	215.938230	24.078815	1.24	−0.023 ± 0.059	22.85	0.89	9.56 ± 1.47	1.96 ± 0.60	4.02 ± 0.46	17.47 ± 0.53	15.17 ± 0.57	2.78 ± 0.55	$1.45^{+0.01}_{-0.01}$	$9.00^{+0.17}_{-0.11}$	$3.54^{+22.83}_{-2.72}$	$0.50^{+0.50}_{-0.25}$	$0.09^{+0.01}_{-0.01}$	$8.30^{+0.09}_{-0.11}$	$0.44^{+0.29}_{-0.26}$	$5.49^{+1.61}_{-1.14}$
M1423	01564	215.943001	24.069814	1.41	0.207 ± 0.104	23.84	0.79	5.95 ± 0.77	1.94 ± 0.43	2.27 ± 1.21	9.01 ± 0.76	5.97 ± 0.48	1.67 ± 0.48	$2.85^{+0.04}_{-0.07}$	$8.68^{+0.01}_{-0.07}$	$0.02^{+0.24}_{-0.02}$	$0.60^{+0.12}_{-0.25}$	$0.06^{+0.00}_{-0.00}$	$8.33^{+0.10}_{-0.12}$	< 0.22	$1.53^{+0.48}_{-0.28}$
M1423	01682	215.959334	24.067604	1.32	−0.000 ± 0.038	23.80	0.90	8.07 ± 1.04	1.59 ± 0.47	4.30 ± 1.63	17.49 ± 0.89	6.85 ± 0.47	0.48 ± 0.47	$1.28^{+0.01}_{-0.00}$	$8.62^{+0.10}_{-0.08}$	$2.91^{+8.45}_{-1.95}$	$0.50^{+0.31}_{-0.22}$	$0.06^{+0.01}_{-0.00}$	$8.09^{+0.13}_{-0.17}$	< 0.16	$3.35^{+0.72}_{-0.47}$
M1423	01808	215.960238	24.065007	2.02	0.035 ± 0.053	23.33	0.87	4.28 ± 0.36	0.90 ± 0.52	1.92 ± 0.79	8.75 ± 0.54	···	···	$1.28^{+0.01}_{-0.00}$	$9.44^{+0.11}_{-0.13}$	$14.51^{+12.61}_{-14.01}$	$0.60^{+0.20}_{-0.48}$	$0.11^{+0.01}_{-0.01}$	$8.33^{+0.13}_{-0.15}$	$1.04^{+1.08}_{-0.73}$	$21.46^{+56.60}_{-12.51}$
M2129	00340	322.352173	-7.679022	2.09	−0.021 ± 0.018	23.73	0.81	1.95 ± 0.89	1.08 ± 0.64	0.64 ± 0.57	10.54 ± 0.65	···	···	$1.46^{+0.02}_{-0.01}$	$8.94^{+0.17}_{-0.04}$	$20.70^{+6.83}_{-13.92}$	$0.80^{+0.10}_{-0.28}$	$0.07^{+0.01}_{-0.00}$	$7.84^{+0.40}_{-0.38}$	$1.75^{+1.18}_{-1.16}$	$43.84^{+112.18}_{-31.85}$
M2129	00380	322.364762	-7.679957	1.81	−0.074 ± 0.036	24.55	0.67	1.50 ± 0.39	2.06 ± 0.58	2.22 ± 0.77	6.94 ± 0.54	···	···	$1.56^{+0.02}_{-0.01}$	$8.23^{+0.17}_{-0.07}$	$3.94^{+1.05}_{-3.46}$	$0.40^{+0.11}_{-0.31}$	$0.05^{+0.00}_{-0.00}$	$7.89^{+0.41}_{-0.52}$	$1.47^{+1.36}_{-0.94}$	$16.98^{+56.16}_{-10.93}$
M2129	00440	322.366118	-7.681231	1.36	0.034 ± 0.050	22.16	0.88	8.43 ± 1.81	···	6.34 ± 2.65	8.86 ± 1.97	33.17 ± 1.40	6.90 ± 1.34	$1.53^{+0.02}_{-0.01}$	$9.63^{+0.13}_{-0.11}$	$59.57^{+42.05}_{-56.40}$	$1.50^{+0.22}_{-0.53}$	$0.16^{+0.03}_{-0.02}$	$8.63^{+0.14}_{-0.12}$	$2.05^{+0.41}_{-0.42}$	$44.89^{+17.40}_{-13.01}$
M2129	00465	322.367391	-7.681865	1.36	0.036 ± 0.027	22.34	0.88	7.06 ± 1.23	1.81 ± 0.62	3.08 ± 0.85	1.27 ± 1.15	27.21 ± 0.70	5.59 ± 0.68	$1.57^{+0.02}_{-0.01}$	$9.71^{+0.08}_{-0.08}$	$2.92^{+99.02}_{-2.70}$	$1.20^{+0.80}_{-0.25}$	$0.18^{+0.02}_{-0.02}$	$8.90^{+0.13}_{-0.15}$	$2.26^{+0.58}_{-0.55}$	$42.01^{+24.05}_{-14.75}$
M2129	00565	322.364752	-7.683770	1.37	0.064 ± 0.064	22.34	0.92	10.16 ± 2.04	1.77 ± 1.00	12.87 ± 2.50	15.41 ± 1.84	17.05 ± 1.14	5.64 ± 1.14	$2.00^{+0.02}_{-0.02}$	$9.46^{+0.26}_{-0.16}$	$1.65^{+41.19}_{-1.64}$	$0.70^{+0.77}_{-0.36}$	$0.13^{+0.05}_{-0.02}$	$8.33^{+0.15}_{-0.39}$	< 0.42	$5.60^{+2.83}_{-1.34}$
M2129	00690	322.346464	-7.685883	1.88	0.049 ± 0.043	23.08	0.78	9.45 ± 0.59	0.70 ± 0.95	4.85 ± 0.76	18.93 ± 0.82	···	···	$2.73^{+0.02}_{-0.07}$	$8.85^{+0.10}_{-0.05}$	$15.65^{+6.52}_{-10.14}$	$0.80^{+0.10}_{-0.20}$	$0.06^{+0.01}_{-0.00}$	$8.33^{+0.11}_{-0.14}$	< 1.01	$15.12^{+27.89}_{-7.66}$
M2129	01408	322.369038	-7.700541	1.48	0.087 ± 0.125	23.65	0.83	4.86 ± 0.70	1.39 ± 0.45	2.27 ± 0.73	8.91 ± 0.79	8.43 ± 0.57	4.23 ± 0.76	$1.49^{+0.02}_{-0.02}$	$8.98^{+0.16}_{-0.09}$	$16.52^{+9.96}_{-16.29}$	$1.20^{+0.21}_{-0.73}$	$0.08^{+0.01}_{-0.00}$	$8.32^{+0.15}_{-0.17}$	< 0.48	$4.81^{+2.41}_{-1.27}$
M2129	01539	322.363350	-7.703212	1.64	0.021 ± 0.027	22.08	0.94	13.52 ± 0.95	0.45 ± 1.21	6.47 ± 1.12	9.61 ± 1.12	···	···	$1.39^{+0.01}_{-0.01}$	$9.93^{+0.08}_{-0.12}$	$45.29^{+59.20}_{-44.93}$	$1.00^{+0.30}_{-0.50}$	$0.21^{+0.03}_{-0.03}$	$8.63^{+0.13}_{-0.12}$	$1.09^{+0.75}_{-0.72}$	$31.57^{+55.80}_{-19.34}$
M2129	01665	322.358149	-7.706707	1.56	−0.028 ± 0.030	23.26	0.79	6.84 ± 0.68	1.91 ± 0.47	3.74 ± 0.78	15.71 ± 0.85	4.35 ± 1.29	···	$1.40^{+0.01}_{-0.01}$	$9.31^{+0.11}_{-0.21}$	$6.99^{+7.03}_{-6.93}$	$0.50^{+0.36}_{-0.43}$	$0.11^{+0.01}_{-0.03}$	$8.18^{+0.13}_{-0.16}$	< 0.28	$6.23^{+2.77}_{-1.41}$
M2129	01833	322.362724	-7.709921	2.30	0.034 ± 0.011	22.45	0.91	20.08 ± 1.32	3.42 ± 0.92	8.64 ± 0.96	47.71 ± 1.15	···	···	$1.27^{+0.01}_{-0.01}$	$9.76^{+0.05}_{-0.03}$	$150.11^{+39.63}_{-16.90}$	$1.00^{+0.10}_{-0.01}$	$0.14^{+0.01}_{-0.00}$	$8.24^{+0.11}_{-0.13}$	< 0.65	$87.00^{+109.28}_{-36.79}$
RXJ1347	00664	206.904786	-11.750602	1.69	−0.090 ± 0.040	23.01	0.48	12.64 ± 0.65	4.88 ± 1.09	5.93 ± 0.79	51.74 ± 0.95	···	···	$1.40^{+0.11}_{-0.07}$	$8.81^{+0.02}_{-0.03}$	$1.52^{+0.09}_{-0.11}$	$0.00^{+0.00}_{-0.00}$	$0.06^{+0.00}_{-0.00}$	$8.08^{+0.14}_{-0.15}$	< 0.85	$34.43^{+54.74}_{-16.28}$
RXJ1347	01443	206.882540	-11.764358	1.77	−0.028 ± 0.038	21.75	0.93	21.20 ± 0.96	···	6.34 ± 1.21	18.50 ± 1.30	···	···	$3.36^{+0.70}_{-0.39}$	$9.49^{+0.19}_{-0.09}$	$0.77^{+46.86}_{-0.64}$	$0.30^{+0.62}_{-0.24}$	$0.12^{+0.03}_{-0.01}$	$8.53^{+0.10}_{-0.11}$	< 0.63	$12.80^{+20.97}_{-6.71}$
RXJ2248	00206	342.175906	-44.516503	1.43	−0.020 ± 0.104	21.53	0.97	14.31 ± 1.82	0.36 ± 1.05	7.84 ± 1.80	7.13 ± 1.72	12.87 ± 1.05	···	$1.83^{+0.01}_{-0.02}$	$9.87^{+0.04}_{-0.03}$	$0.05^{+3.05}_{-0.05}$	$0.50^{+0.25}_{-0.20}$	$0.22^{+0.01}_{-0.01}$	$8.60^{+0.10}_{-0.11}$	< 0.23	$4.09^{+1.27}_{-0.73}$
RXJ2248	00331	342.169955	-44.518922	1.93	0.004 ± 0.029	23.29	0.79	9.03 ± 0.65	2.54 ± 0.99	2.96 ± 1.29	15.17 ± 0.90	···	···	$1.86^{+0.02}_{-0.02}$	$9.01^{+0.20}_{-0.04}$	$0.58^{+9.53}_{-0.35}$	$0.00^{+0.58}_{-0.00}$	$0.07^{+0.02}_{-0.00}$	$8.36^{+0.11}_{-0.13}$	< 0.72	$16.56^{+27.33}_{-7.66}$
RXJ2248	00428	342.186462	-44.521187	1.23	0.052 ± 0.036	22.19	0.96	8.61 ± 5.13	0.95 ± 1.51	10.12 ± 1.11	24.10 ± 1.15	11.30 ± 1.33	···	$4.97^{+0.08}_{-0.09}$	$9.13^{+0.05}_{-0.10}$	$1.92^{+0.54}_{-0.42}$	$0.20^{+0.11}_{-0.15}$	$0.10^{+0.00}_{-0.01}$	$8.05^{+0.17}_{-0.24}$	< 0.19	$1.31^{+0.36}_{-0.22}$
RXJ2248	00786	342.169402	-44.527222	1.84	−0.135 ± 0.070	23.81	0.46	7.24 ± 0.67	2.04 ± 0.97	2.77 ± 0.76	25.73 ± 0.86	···	···	$3.38^{+0.07}_{-0.06}$	$7.96^{+0.03}_{-0.01}$	$2.70^{+0.05}_{-0.17}$	$0.30^{+0.00}_{-0.01}$	$0.05^{+0.00}_{-0.00}$	$8.12^{+0.13}_{-0.15}$	< 0.73	$9.32^{+15.70}_{-4.22}$
RXJ2248	01250	342.192946	-44.536578	1.40	−0.068 ± 0.094	22.52	0.88	8.96 ± 2.06	···	0.25 ± 2.06	15.49 ± 1.92	17.06 ± 1.11	4.18 ± 1.13	$3.14^{+0.04}_{-0.05}$	$9.17^{+0.08}_{-0.06}$	$0.16^{+1.02}_{-0.16}$	$0.20^{+0.33}_{-0.20}$	$0.09^{+0.01}_{-0.01}$	$8.41^{+0.12}_{-0.12}$	$1.14^{+0.62}_{-0.54}$	$6.71^{+4.51}_{-2.47}$
M1149	00270	177.385990	22.414074	1.27	−0.160 ± 0.030	22.55	0.71	10.28 ± 5.23	4.84 ± 8.65	24.87 ± 0.94	29.58 ± 0.72	13.33 ± 0.36	0.36 ± 0.35	$1.96^{+0.03}_{-0.03}$	$9.00^{+0.12}_{-0.04}$	$0.24^{+13.40}_{-0.20}$	$0.20^{+0.60}_{-0.20}$	$0.09^{+0.01}_{-0.00}$	$7.91^{+0.14}_{-0.15}$	< 0.03	$3.04^{+0.15}_{-0.13}$
M1149	00593	177.406922	22.407499	1.48	−0.010 ± 0.020	22.40	0.81	23.44 ± 1.40	6.00 ± 0.85	5.72 ± 0.44	31.48 ± 0.45	29.90 ± 0.34	5.31 ± 0.41	$2.02^{+0.04}_{-0.03}$	$9.13^{+0.09}_{-0.01}$	$39.40^{+0.65}_{-39.32}$	$1.00^{+0.03}_{-1.00}$	$0.09^{+0.01}_{-0.00}$	$8.38^{+0.06}_{-0.06}$	$0.93^{+0.14}_{-0.14}$	$17.50^{+2.32}_{-2.10}$
M1149	00600	177.389220	22.407583	2.31	−0.180 ± 0.080	24.12	0.76	1.01 ± 0.38	1.33 ± 0.29	1.40 ± 0.27	8.31 ± 0.31	···	···	$6.87^{+0.33}_{-0.29}$	$8.32^{+0.09}_{-0.03}$	$0.90^{+0.04}_{-0.06}$	$0.00^{+0.01}_{-0.00}$	$0.04^{+0.00}_{-0.00}$	$7.83^{+0.28}_{-0.23}$	< 0.85	$3.10^{+6.36}_{-1.55}$
M1149	00676	177.415126	22.406195	1.68	0.060 ± 0.050	23.31	0.78	7.48 ± 0.77	2.58 ± 0.29	2.57 ± 0.19	16.16 ± 0.22	···	···	$1.77^{+0.04}_{-0.04}$	$8.93^{+0.16}_{-0.07}$	$18.72^{+5.91}_{-17.88}$	$0.90^{+0.10}_{-0.50}$	$0.07^{+0.01}_{-0.01}$	$8.19^{+0.09}_{-0.10}$	< 0.18	$4.91^{+1.66}_{-0.69}$
M1149	00683	177.397234	22.406181	1.68	−0.220 ± 0.050	24.41	0.10	3.80 ± 1.02	6.97 ± 0.48	6.05 ± 0.33	28.23 ± 0.33	···	···	$5.83^{+0.23}_{-0.26}$	$6.90^{+0.02}_{-0.02}$	$0.24^{+0.01}_{-0.01}$	$0.00^{+0.00}_{-0.00}$	$0.05^{+0.00}_{-0.00}$	$7.58^{+0.34}_{-0.14}$	< 0.10	$3.20^{+0.67}_{-0.37}$
M1149	00862	177.403416	22.402433	1.49	−0.040 ± 0.020	21.41	0.97	19.22 ± 3.17	···	11.35 ± 1.08	5.96 ± 1.03	45.12 ± 0.70	···	$3.63^{+0.08}_{-0.06}$	$9.79^{+0.10}_{-0.15}$	$24.57^{+8.35}_{-20.09}$	$1.00^{+0.16}_{-0.31}$	$0.19^{+0.03}_{-0.04}$	$8.96^{+0.06}_{-0.08}$	$0.72^{+0.29}_{-0.29}$	$11.96^{+3.23}_{-2.56}$
M1149	01058	177.391848	22.400105	1.25	−0.030 ± 0.030	22.61	0.33	21.25 ± 2.59	16.58 ± 1.09	13.49 ± 0.69	94.78 ± 0.56	40.66 ± 0.29	2.06 ± 0.28	$3.83^{+0.07}_{-0.06}$	$8.10^{+0.01}_{-0.08}$	$3.69^{+0.06}_{-0.60}$	$0.10^{+0.02}_{-0.10}$	$0.05^{+0.00}_{-0.00}$	$7.96^{+0.10}_{-0.10}$	< 0.02	$4.31^{+0.19}_{-0.13}$
M1149	01322	177.392541	22.394921	1.49	−0.010 ± 0.020	23.33	0.78	0.20 ± 1.68	5.35 ± 0.96	0.82 ± 0.61	16.73 ± 0.62	7.14 ± 0.41	8.37 ± 0.80	$2.88^{+0.06}_{-0.04}$	$8.84^{+0.02}_{-0.01}$	$20.93^{+0.30}_{-0.87}$	$1.60^{+0.00}_{-0.01}$	$0.07^{+0.00}_{-0.00}$	$8.21^{+0.07}_{-0.08}$	< 0.18	$1.78^{+0.40}_{-0.21}$
M1149	01468	177.406546	22.392860	1.89	−0.070 ± 0.040	23.54	0.37	2.71 ± 0.80	3.29 ± 0.39	2.58 ± 0.30	39.69 ± 0.31	···	···	$56.29^{+8.89}_{-6.27}$	$6.22^{+0.05}_{-0.06}$	$0.05^{+0.01}_{-0.01}$	$0.00^{+0.00}_{-0.00}$	$0.05^{+0.00}_{-0.00}$	$7.92^{+0.08}_{-0.08}$	< 0.69	$0.49^{+0.72}_{-0.24}$
M1149	01704	177.398643	22.387499	2.28	0.020 ± 0.080	24.97	0.52	3.30 ± 0.30	0.83 ± 0.22	0.87 ± 0.21	7.86 ± 0.26	···	···	$2.66^{+0.07}_{-0.10}$	$7.71^{+0.11}_{-0.08}$	$1.11^{+0.24}_{-0.14}$	$0.00^{+0.05}_{-0.00}$	$0.04^{+0.00}_{-0.00}$	$8.18^{+0.10}_{-0.10}$	< 0.36	$3.86^{+3.49}_{-1.04}$

[a] The observed JH_{140}-band magnitude, before accounting for lensing magnification.

[b] The reduction factor of JH_{140}-band flux, after subtracting the nebular emission that falls within the corresponding wavelength window.

[c] The lensing magnification estimated from various mass models of galaxy clusters. For all the *HFF* clusters, we use the SHARON & JOHNSON version 4corr models (Johnson et al. 2014). For all the *CLASH*-only clusters except RXJ1347, we use the Zitrin PIEMD+eNFW version 2 models (Zitrin et al. 2015). For RXJ1347, we use our own model built following closely the approach in Johnson et al. (2014).

[d] The flux ratio of [N II] and Hα, estimated from the prescription of Faisst et al. (2017). This value is used to correct for the blended Hα-[N II] fluxes in grism spectra, if necessary.

[e] Values presented here are corrected for lensing magnification.

REFERENCES

Belfiore, F., Vincenzo, F., Maiolino, R., & Matteucci, F. 2019, 1903.05105

Belfiore, F., Maiolino, R., Tremonti, C. A., et al. 2017, Monthly Notices of the Royal Astronomical Society, 469, 151

Berg, D. A., Skillman, E. D., Croxall, K. V., et al. 2015, The Astrophysical Journal, 806, 16

Bertin, E., & Arnouts, S. 1996, Astronomy and Astrophysics Supplement Series, 117, 393

Bresolin, F. 2019, eprint arXiv:1907.05071, 1907.05071

Brinchmann, J., Charlot, S., White, S. D. M., et al. 2004, Monthly Notices of the Royal Astronomical Society, 351, 1151

Bruzual, G., & Charlot, S. 2003, Monthly Notices of the Royal Astronomical Society, 344, 1000

Calzetti, D., Armus, L., Bohlin, R. C., et al. 2000, The Astrophysical Journal, 533, 682

Cappellari, M., & Copin, Y. 2003, Monthly Notices of the Royal Astronomical Society, 342, 345

Cardelli, J. A., Clayton, G. C., & Mathis, J. S. 1989, The Astronomical Journal, 345, 245

Carton, D., Brinchmann, J., Contini, T., et al. 2018, Monthly Notices of the Royal Astronomical Society, 1805.08131

Chabrier, G. 2003, Publications of the Astronomical Society of the Pacific, 115, 763

Coil, A. L., Aird, J., Reddy, N. A., et al. 2015, The Astrophysical Journal, 801, 35

Cresci, G., Mannucci, F., Maiolino, R., et al. 2010, Nature, 467, 811

Curti, M., Maiolino, R., Cirasuolo, M., et al. 2020, Monthly Notices of the Royal Astronomical Society, 492, 821

Davé, R., Finlator, K., & Oppenheimer, B. D. 2012, Monthly Notices of the Royal Astronomical Society, 421, 98

Dekel, A., & Mandelker, N. 2014, Monthly Notices of the Royal Astronomical Society, 444, 2071

Dekel, A., Birnboim, Y., Engel, G., et al. 2009, Nature, 457, 451

Diehl, S., & Statler, T. S. 2006, Monthly Notices of the Royal Astronomical Society, 368, 497

Erb, D. K. 2015, Nature, 523, 169

Faisst, A. L., Masters, D. C., Wang, Y., et al. 2017, eprint arXiv:1710.00834, 1710.00834

Finlator, K., & Davé, R. 2008, Monthly Notices of the Royal Astronomical Society, 385, 2181

Foreman-Mackey, D., Hogg, D. W., Lang, D., & Goodman, J. 2013, Publications of the Astronomical Society of the Pacific, 125, 306

Förster Schreiber, N. M., Renzini, A., Mancini, C., et al. 2018, eprint arXiv:1802.07276, 1802.07276

Gibson, B. K., Pilkington, K., Brook, C. B., Stinson, G. S., & Bailin, J. 2013, Astronomy and Astrophysics, 554, A47

Gonzaga, S. 2012, The DrizzlePac Handbook, HST Data Handbook

Henry, A. L., Scarlata, C., Domínguez, A., et al. 2013, The Astrophysical Journal, 776, L27

Hirtenstein, J., Jones, T. A., Wang, X., et al. 2018, eprint arXiv:1811.11768, 1811.11768

Ho, I. T., Kudritzki, R.-P., Kewley, L. J., et al. 2015, Monthly Notices of the Royal Astronomical Society, 448, 2030

Ho, I. T., Seibert, M., Meidt, S. E., et al. 2017, The Astrophysical Journal, 846, 39

Hopkins, P. F., Kereš, D., Onorbe, J., et al. 2014, Monthly Notices of the Royal Astronomical Society, 445, 581

Johnson, T. L., Sharon, K., Bayliss, M. B., et al. 2014, The Astrophysical Journal, 797, 48

Jones, T. A., Ellis, R. S., Jullo, E., & Richard, J. 2010, The Astrophysical Journal Letters, 725, L176

Jones, T. A., Ellis, R. S., Richard, J., & Jullo, E. 2013, The Astrophysical Journal, 765, 48

Jones, T. A., Wang, X., Schmidt, K. B., et al. 2015, The Astronomical Journal, 149, 107

Juneau, S., Bournaud, F., Charlot, S., et al. 2014, The Astrophysical Journal, 788, 88

Kelly, B. C. 2007, The Astrophysical Journal, 665, 1489

Kennicutt, R. C. J. 1998, Annual Review of Astronomy and Astrophysics, 36, 189

Kriek, M. T., van Dokkum, P. G., Franx, M., Illingworth, G. D., & Magee, D. K. 2009, The Astrophysical Journal, 705, L71

Leethochawalit, N., Jones, T. A., Ellis, R. S., et al. 2016, The Astrophysical Journal, 820, 84

Lilly, S. J., Carollo, C. M., Pipino, A., Renzini, A., & Peng, Y.-j. 2013, The Astrophysical Journal, 772, 119

Lotz, J. M., Koekemoer, A. M., Coe, D., et al. 2016, 1605.06567

Ma, X., Hopkins, P. F., Feldmann, R., et al. 2017, Monthly Notices of the Royal Astronomical Society, 466, 4780

Madau, P., & Dickinson, M. E. 2014, Annual Review of Astronomy and Astrophysics, 52, 415

Maiolino, R., & Mannucci, F. 2018, 1811.09642

Maiolino, R., Nagao, T., Grazian, A., et al. 2008, Astronomy and Astrophysics, 488, 463

Peng, Y.-j., & Maiolino, R. 2014, Monthly Notices of the Royal Astronomical Society, 443, 3643

Pettini, M., & Pagel, B. E. J. 2004, Monthly Notices of the Royal Astronomical Society, 348, L59

Pilkington, K., Few, C. G., Gibson, B. K., et al. 2012, Astronomy and Astrophysics, 540, A56

Poetrodjojo, H. M., Groves, B. A., Kewley, L. J., et al. 2018, Monthly Notices of the Royal Astronomical Society

Postman, M., Coe, D., Benítez, N., et al. 2012, The Astrophysical Journal Supplement Series, 199, 25

Price-Whelan, A. M., Sipocz, B. M., Günther, H. M., et al. 2018, eprint arXiv:1801.02634, 1801.02634

Robitaille, T., & Bressert, E. 2012, Astrophysics Source Code Library

Sanchez, S. F., Rosales-Ortega, F., Iglesias-Páramo, J., et al. 2014, Astronomy and Astrophysics, 563, A49

Sanchez-Menguiano, L., Sanchez, S. F., Pérez, I., et al. 2016, Astronomy and Astrophysics, 587, A70

Schmidt, K. B., Treu, T. L., Brammer, G. B., et al. 2014, The Astrophysical Journal Letters, 782, L36

Smartt, S. J., & Rolleston, W. R. J. 1997, The Astrophysical Journal, 481, L47

Speagle, J. S., Steinhardt, C. L., Capak, P. L., & Silverman, J. D. 2014, The Astrophysical Journal Supplement Series, 214, 15

Storey, P. J., & Zeippen, C. J. 2000, Monthly Notices of the Royal Astronomical Society, 312, 813

Stott, J. P., Sobral, D., Smail, I. R., et al. 2013, Monthly Notices of the Royal Astronomical Society, 430, 1158

Stott, J. P., Sobral, D., Swinbank, A. M., et al. 2014, Monthly Notices of the Royal Astronomical Society, 443, 2695

Swinbank, A. M., Sobral, D., Smail, I. R., et al. 2012, Monthly Notices of the Royal Astronomical Society, 426, 935

Tissera, P. B., Rosas-Guevara, Y., Bower, R. G., et al. 2018, eprint arXiv:1806.04575, 1806.04575

Treu, T. L., Schmidt, K. B., Brammer, G. B., et al. 2015, The Astrophysical Journal, 812, 114

van Dokkum, P. G., Brammer, G. B., Fumagalli, M., et al. 2011, The Astrophysical Journal, 743, L15

Vogelsberger, M., Genel, S., Springel, V., et al. 2014, Nature, 509, 177

Wang, X., Jones, T. A., Treu, T. L., et al. 2017, The Astrophysical Journal, 837, 89

—. 2019, The Astrophysical Journal, 882, 94

Whitaker, K. E., Franx, M., Leja, J., et al. 2014, The Astrophysical Journal, 795, 104

Wuyts, E., Wisnioski, E., Fossati, M., et al. 2016, The Astrophysical Journal, 827, 74

Yuan, T., Kewley, L. J., & Rich, J. A. 2013, The Astrophysical Journal, 767, 106

Zitrin, A., Fabris, A., Merten, J. C., et al. 2015, The Astrophysical Journal, 801, 44